

A hybrid weakly conforming finite
element method for applications in solid
mechanics

Zur Erlangung des akademischen Grades eines
DOKTORS DER NATURWISSENSCHAFTEN

von der KIT-Fakultät für Mathematik des
Karlsruher Instituts für Technologie (KIT)

genehmigte Dissertation

von
Dipl.-Math.oec. Julian Gabriel Krämer
aus
Hambrücken

Referent: Prof. Dr. Christian Wieners

Korreferent: Prof. Dr. Willy Dörfler

Tag der mündlichen Prüfung: 23. September 2020

Danksagung

Ich möchte mich bei Prof. Dr. Christian Wieners bedanken, der mir die Möglichkeit gegeben hat zu promovieren und mich die ganze Zeit über stets umfassend betreut hat. Seine Tür war immer offen und sein Fachwissen war immens hilfreich, sei es bei mathematischen Fragestellungen oder beim Programmieren der Algorithmen.

Ich bedanke mich des weiteren bei Prof. Dr. Willy Dörfler dafür, dass er sich bereit erklärt hat das Korreferat zu übernehmen und für die Vermittlung der Doktorandenstelle bei Herrn Wieners nach dem Studium.

Bei allen Mitarbeitern des Instituts für Angewandte und Numerische Mathematik 3, die mit mir zusammen gearbeitet haben, möchte ich mich für das tolle Arbeitsklima bedanken. Wenn eine Frage aufkam, war stets eine Bürotür offen und auch die Freizeit kam beim gemeinsamen Kickern, Waffeln backen, Wasserski fahren, Spieleabenden und anderen Aktionen selten zu kurz. Die regen Gespräche über Fußball, Weltpolitik und Mathematik haben meinen Arbeitsalltag sehr bereichert.

Bedanken möchte ich mich auch bei meiner Familie, insbesondere bei meinen Eltern, die mich jahrelang bedingungslos unterstützt haben und ohne die meine Ausbildung nicht möglich gewesen wäre. Meine Kinder haben mich stets motiviert und auch mit Spielsachen für die Arbeit beglückt, damit mir nicht langweilig wird, auch dafür möchte ich danke sagen.

Und zum Schluss möchte ich mich insbesondere bei meiner tollen Frau Julia bedanken, die mich nicht nur im Studium auf die Vorzüge der Numerik

gebracht hat, sondern die mir auch in den heißen Phasen meiner Promotion kompromisslos den Rücken frei gehalten hat; ohne sie wäre diese Promotion nicht möglich gewesen.

Contents

1	Introduction	1
2	Solid mechanics	5
2.1	Kinematics	5
2.2	Balance equations	8
2.3	Constitutive relations	10
2.4	Linear elasticity	12
3	Numerical methods for linear elasticity	13
3.1	Established methods and numerical setting	13
3.2	Weakly conforming method	17
3.3	Choice of local multiplier spaces	17
3.4	Static condensation	18
3.5	Choice of local cell spaces	21
3.6	Numerical costs compared to established methods	22
3.7	Implementation of the weakly conforming method	25
4	Numerical properties of the weakly conforming finite element method	29
4.1	Convergence rates in a smooth setting	30
4.2	Geometrical singularities	36
4.3	Locking phenomena	43
4.4	Geometrical anisotropy	48
4.5	Material-induced anisotropy	52
4.6	Incompressible materials - dependency on material parameters	55

5	A priori error analysis of the weakly conforming method and adaptive applications	61
5.1	A residual error estimator	61
5.2	Adaptive algorithm	70
5.3	Example with known solution	76
5.4	Adaptive strategies for the L-shaped domain	78
5.5	A corner singularity in 3D	82
6	Non-linear materials	87
6.1	Hyperelasticity	87
6.2	Elasto-plastic damage model	94
6.3	Contact Problems	105
7	Conclusion	113

Chapter 1

Introduction

The numerical simulation of mechanical parts and larger objects play an important role in modern times, for example the investigation of the structural integrity of planned buildings. Lower scale models can only provide limited information and are often more expensive than computerized simulations. There are however important requirements, which those computations need to hold. They need to be able to produce reliable solutions, they need to be able to solve a broad spectrum of different material models and they need to be as efficient as possible, since computational resources can become expensive quickly for large scale simulations.

In this work we present a new weakly conforming approach, situated in the well known and researched field of finite element methods, and demonstrate its suitability for applications in solid mechanics. However, the method is not limited to this area; in theory it can be applied to any numerical problem which can be solved by other finite element method.

State of the art

Finite element methods are developed and analyzed since the 1950s and gained importance in the 1980s and 90s, as modern technology allowed larger and more precise simulations, as the computational power increased rapidly. Sensible starting points for finite element methods are [21] and [52].

Classical finite element approaches use continuous ansatz functions over the whole domain, thus are called continuous methods. This way they achieve

continuity between cells, which is sensible since the cells are representing a continuous object, which is only subdivided into cells for the numerical method. Contrary to this, discontinuous Galerkin methods use ansatz functions which are only piecewise continuous and need other criteria to achieve inter cell continuity. One wide spread approach is to use penalty terms, which assure continuity by penalizing jumps between cells, which leads to their diminution as the numerical solver searches for a minimum. Important sources for discontinuous Galerkin methods are [13, 33, 8, 32] and in [39, 26, 46, 34] the adaption of them to solid mechanics is discussed. The approach for this work is a discontinuous method, but uses no penalty terms, but rather a different approach for the enforcement of continuity. It enforces the inter cell jumps to diminish only in a weak sense. This extends the higher order generalization of Crouzeix–Raviart finite elements, which are presented in [31] for the diffusion equation to elasticity. One advantage of the weakly conforming approach is that through hybridization some degrees can be eliminated, which decreases the size of the global system matrix. A family of hybrid non-conforming discretizations similar to the one presented in this work is described in [1, 2, 3, 50], where the application to plasticity and hyperelastic materials is considered. In [29] a hybrid method for contact problems is presented.

Parts of this work were published together with Christian Wieners, Barbara Wohlmuth and Linus Wunderlich in [43]; in [17] the aforementioned were joined by Hamid Reza Bayat, Stefanie Reese and Stephan Wulfinghoff. Another joined paper with Christian Wieners, Barbara Wohlmuth and Linus Wunderlich is available at [44]. Additionally, part of this work will be submitted with our SPP partners for a book chapter [15] within the final report of our SPP 1748.

Work group and contributions of this work

Our research group within the priority program consists of the project initiators Stefanie Reese of Aachen, Christian Wieners of Karlsruhe and Barbara Wohlmuth of München, as well as the doctoral researchers Hamid Reza Bayat, Linus Wunderlich and myself. Within our group we aimed at developing and analyzing highly sophisticated hybrid schemes for solid mechanics. The re-

search group of Prof. Reese contributed to the project their highly developed finite element technologies and developed a reduced integration scheme with hourglass stabilization for the incomplete interior penalty discontinuous Galerkin method, cf. [16] and [18]. The group of Prof. Wohlmuth focused on developing a complete analytical framework of the newly developed methods, for example the main part of the a-priori error estimation given in Section 5.1 were done by her group. Additionally they researched isogeometric approaches, cf. [40]. The dissertation of Linus Wunderlich, [61], covered various hybrid finite element approaches, including the weakly conforming method. Our group, led by Prof. Wieners implemented and investigated the weakly conforming methods, using our experience in scientific computing.

Within the scope of this priority program, we supervised the bachelor thesis of Kai Ulrich [57] in cooperation with Niklas Baumgarten, where he compared different discretization methods, including the weakly conforming method, for the Laplace equation.

The contribution of this work is a complete investigation of the newly proposed hybrid method, which includes an analytical framework in linear elasticity, a discussion of numerical properties, efficient adaptive strategies and we investigated the behavior of the weakly conforming method in the framework of several non-conforming model formulations, including damage, plasticity, contact and hyperelastic materials. These models we analyzed the deployment of the weakly conforming method and developed algorithms which we implemented in our finite element library. We compare the newly developed scheme to established ones, namely conforming and discontinuous Galerkin methods, to comprehend in which cases it could be beneficiary to deploy the weakly conforming method.

Structure of this work

In Chapter 2 the mathematical modeling of elasticity is introduced, following mainly [30], to clarify the mechanical terms which are used throughout this work. In Chapter 3 our weakly conforming approach is presented and analyzed. Additionally, two representative methods of classical approaches are

briefly discussed, a conforming one and the symmetric interior penalty discontinuous Galerkin method. These two are used as a comparison in subsequent chapters. In Chapter 4 the fundamental properties of our method are reviewed. It is important for the application to solid mechanics, that certain difficulties arising from physical circumstances are modeled efficiently and reliable. This is discussed with various examples in this chapter and the numerical properties are compared to our benchmark methods. In Chapter 5 an a priori error analysis is presented, as well as an adaptive strategy which uses the derived residual error estimator, paired with a Doerfler marking strategy, to make use of an optimal distribution of computational resources. The main part of this work is analyzing linear elastic materials, as this shortens the notation and is more suitable to explain the functionality of our method. However in Chapter 6 we will discuss several more sophisticated non-linear models and apply our weakly conforming method to these. This involves large strain elasticity, plasticity, damage and a contact formulation.

Acknowledgements

This work was financed by the German research foundation Deutsche Forschungsgemeinschaft (DFG) within the priority program 1748, which I gratefully acknowledge. The priority program aims at the development of modern non-conventional discretization methods in the field of solid mechanics and was financed for six years.

Furthermore I gratefully acknowledge the possibility to perform some of the large computations on the supercomputer ForHLR funded by the Ministry of Science, Research and the Arts Baden-Württemberg and by the Federal Ministry of Education and Research.

Chapter 2

Solid mechanics

Content of this chapter In this chapter the foundations of linear solid mechanics are presented to clarify the mechanical vocabulary used in the subsequent chapters. In our studies and numerical experiments we focus on the observation of deformation phenomena. Additionally, throughout this work we only look at quasi-static problems, where we are at a thermo-dynamic equilibrium and all time dependent derivatives can be neglected. To model mechanical phenomena physically correct, balance laws are coupled with material models to determine the values of displacement and stress values.

Origin of this chapter There are many notable publications on this well studied subject; we follow the structure of [30] closely; another important source is [48].

2.1 Kinematics

Kinematics refers to the description and modeling of the deformation and motion of a body of material and does not take into consideration the forces which cause the body to deform or to move.

Let Ω , an open subset of \mathbb{R}^3 , be a given initial or reference configuration of a body. Together with its boundary $\partial\Omega$ it yields the closed set $\bar{\Omega}$. The boundary is divided into different sections with different boundary conditions, depending on the forces which act on each subset.

For given internal and external forces, the mapping $\varphi : \Omega \rightarrow \Omega^\varphi \subset \mathbb{R}^3$

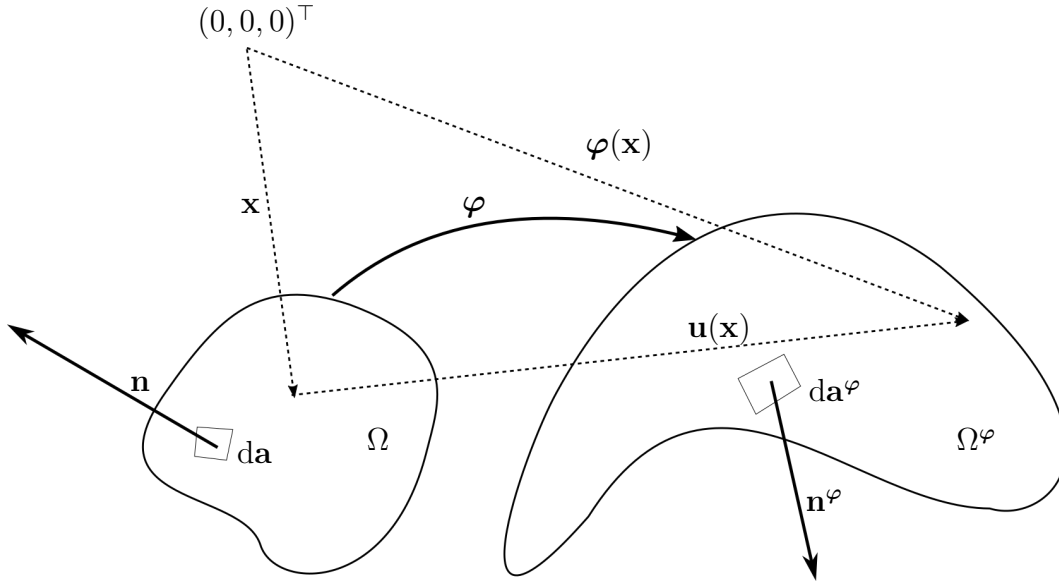


Figure 2.1: Basic variables used for the description of deformations.

describes the transition of Ω into a deformed state. The new domain in the deformed configuration is called Ω^φ . The tensor

$$\mathbf{F}(\mathbf{x}) := D\varphi(\mathbf{x}) = \begin{pmatrix} \frac{\partial}{\partial x_1}\varphi_1 & \frac{\partial}{\partial x_2}\varphi_1 & \frac{\partial}{\partial x_3}\varphi_1 \\ \frac{\partial}{\partial x_1}\varphi_2 & \frac{\partial}{\partial x_2}\varphi_2 & \frac{\partial}{\partial x_3}\varphi_2 \\ \frac{\partial}{\partial x_1}\varphi_3 & \frac{\partial}{\partial x_2}\varphi_3 & \frac{\partial}{\partial x_3}\varphi_3 \end{pmatrix}$$

is called deformation gradient. We require the property $J := \det \mathbf{F} > 0$, since a deformation by definition preserves orientation. In the following we will often omit the argument of \mathbf{F} if we study its properties at a fixed point.

Most of the times we do not treat the deformation itself, but rather the displacement field $\mathbf{u} : \Omega \rightarrow \mathbb{R}^3$, which is defined by

$$\varphi(\mathbf{x}) := \mathbf{x} + \mathbf{u}(\mathbf{x}).$$

The relations between those variables are shown in Fig. 2.1.

Strains

If a deformation is not a rigid body translation, i.e. if it does not simply dislocate and rotate the body, but rather actually changes its shape, different parts of the body are deformed in different ways; for this we introduce the

strains. A strain tensor is a measurement of the change in distance between points.

For all points $\mathbf{x} + \delta\mathbf{x} \in \bar{\Omega}$ we study the relation

$$\varphi(\mathbf{x} + \delta\mathbf{x}) - \varphi(\mathbf{x}) = \mathbf{F}(\mathbf{x})\delta\mathbf{x} + \mathcal{O}(|\delta\mathbf{x}|)$$

and

$$|\varphi(\mathbf{x} + \delta\mathbf{x}) - \varphi(\mathbf{x})|^2 = \delta\mathbf{x}^\top \mathbf{F}(\mathbf{x})^\top \mathbf{F}(\mathbf{x}) \delta\mathbf{x} + \mathcal{O}(|\delta\mathbf{x}|^2).$$

The symmetric tensor $\mathbf{C} = \mathbf{F}(\mathbf{x})^\top \mathbf{F}(\mathbf{x})$ is called the *right Cauchy-Green strain tensor*. It is used as a measurement of strain. One important property is, that it should be equal to \mathbf{I} if the deformation consists only of rigid body deformations, where we have no internal forces acting on the body, i.e.

$$\varphi(\mathbf{x}) = \mathbf{a} + \mathbf{Q}\mathbf{x},$$

where $\mathbf{a} \in \mathbb{R}$ and $\mathbf{Q} \in \{\mathbf{Q} \in \mathbb{R}^{3 \times 3} : \mathbf{Q}\mathbf{Q}^\top = \mathbf{I}, \det \mathbf{Q} = 1\}$. Such a \mathbf{Q} corresponds to a rotation in \mathbb{R}^3 . This means that in this case $\mathbf{C} = \mathbf{I}$, which coincides with the postulated lack of strain for the given deformation. The reverse holds true as well, if $\mathbf{C} = \mathbf{I}$ is given, the deformation is a rigid body motion with $\varphi(\mathbf{x}) = \mathbf{a} + \mathbf{Q}\mathbf{x}$.

Green-St.Venant strain tensor

One important strain tensor is the *Green-St.Venant strain tensor* \mathbf{E} . It is defined by the relation

$$2\mathbf{E} = \mathbf{C} - \mathbf{I}$$

and provides a measurement of the deviation of a given deformation to a rigid body deformation. This definition gives us an important quantity: If we express the right Cauchy-Green strain tensor with respect to the deformation $\mathbf{u}(\mathbf{x})$, we get

$$\begin{aligned} \mathbf{C} &= \mathbf{F}^\top \mathbf{F} = \mathbf{I} + \mathbf{D}\mathbf{u}^\top + \mathbf{D}\mathbf{u} + \mathbf{D}\mathbf{u}^\top \mathbf{D}\mathbf{u} = 2\mathbf{E} + \mathbf{I} \\ &\Leftrightarrow \mathbf{E} = \frac{1}{2}(\mathbf{D}\mathbf{u}^\top + \mathbf{D}\mathbf{u} + \mathbf{D}\mathbf{u}^\top \mathbf{D}\mathbf{u}), \end{aligned}$$

where we express the strains \mathbf{E} with respect to the displacements. In the case of small deformations, $\varphi(\mathbf{x}) \approx \mathbf{0} \Leftrightarrow \mathbf{D}\mathbf{u} \approx \mathbf{0}$, the quadratic term is negligible and the strain tensor becomes $\mathbf{E} = \frac{1}{2}(\mathbf{D}\mathbf{u}^\top + \mathbf{D}\mathbf{u}) = \frac{1}{2} \text{sym } \mathbf{D}\mathbf{u}$.

2.2 Balance equations

Since we want a computable model of solid mechanical interactions, we need a system of equations in which we can input our data. First we introduce the balance equations, which arise from the mechanical background.

Applied forces

We distinct between two possible forces, which act on the body of interest. The first kind are volume or body forces, for example gravity, which we define via the vector field

$$\mathbf{f}^\varphi : \Omega^\varphi \rightarrow \mathbb{R}^3.$$

The second kind of forces are surface or traction forces, which act only on the Neumann part of the boundary, $\partial\Omega_N^\varphi$, which we define as

$$\mathbf{g}^\varphi : \partial\Omega_N^\varphi \subset \partial\Omega^\varphi \rightarrow \mathbb{R}^3.$$

An example for such forces is applied pressure from another object, possibly in a positive or negative direction.

Cauchy axiom

With such force densities we can now assume the stress principle of Euler and Cauchy to obtain the Cauchy stress vector. We define $S_1 := \{\mathbf{v} \in \mathbb{R}^3 : |\mathbf{v}| = 1\}$. The stress principle states that for given volume force densities $\mathbf{f}^\varphi : \Omega^\varphi \rightarrow \mathbb{R}^3$ and traction force densities $\mathbf{g}^\varphi : \partial\Omega_N^\varphi \subset \partial\Omega^\varphi \rightarrow \mathbb{R}^3$ a vector field

$$\mathbf{t}^\varphi : \overline{\Omega}^\varphi \times S_1 \rightarrow \mathbb{R}^3$$

exists, with

1. $\mathbf{t}^\varphi(\mathbf{x}^\varphi, \mathbf{n}) = g^\varphi(\mathbf{x}^\varphi)$,
2. $\int_{V^\varphi} \mathbf{f}^\varphi(\mathbf{x}^\varphi) \, d\mathbf{x}^\varphi + \int_{\partial V^\varphi} \mathbf{t}^\varphi(\mathbf{x}^\varphi, \mathbf{n}^\varphi) \, d\mathbf{a}^\varphi = 0$ (force balance),
3. $\int_{V^\varphi} \mathbf{x}^\varphi \wedge \mathbf{f}^\varphi(\mathbf{x}^\varphi) \, d\mathbf{x}^\varphi + \int_{\partial V^\varphi} \mathbf{x}^\varphi \wedge \mathbf{t}^\varphi(\mathbf{x}^\varphi, \mathbf{n}^\varphi) \, d\mathbf{a}^\varphi = 0$ (moment balance).

We call this vector field the Cauchy stress vector. The Cauchy axiom provides the existence of elementary surface forces $\mathbf{t}^\varphi(\mathbf{x}^\varphi, \mathbf{n}^\varphi)$, which only depend on the outer normal vector of a surface point of Ω^φ . Furthermore it provides that a body under exterior forces is, when it reaches a static, deformed state, in a state of a equilibrium, both with respect to forces, as well as with respect to moments.

Cauchy stress

Next we look at a fundamental result of solid mechanics, Cauchy's theorem. It states, that the dependence of the Cauchy stress vector $\mathbf{t}^\varphi(\mathbf{x}^\varphi, \mathbf{n})$ is linear with respect to \mathbf{n} , which means that a tensor $\mathbf{T}^\varphi(\mathbf{x}^\varphi) \in \mathbb{M}_+^3 = \{\mathbf{F} \in \mathbb{R}^{3,3} : \det \mathbf{F} > 0\}$ exists, with $\mathbf{t}^\varphi(\mathbf{x}^\varphi, \mathbf{n}) = \mathbf{T}^\varphi(\mathbf{x}^\varphi)\mathbf{n}$.

Theorem 1 (Cauchy's theorem). *Assume that the applied body force density $\mathbf{f}^\varphi : \Omega^\varphi \rightarrow \mathbb{R}^3$ and the Cauchy stress vector field $\mathbf{t}^\varphi : \bar{\Omega}^\varphi \times S_1 \rightarrow \mathbb{R}^3$ is continuously differentiable with respect to $\mathbf{x}^\varphi \in \Omega^\varphi$ for each $\mathbf{n} \in S_1$ and continuous with respect to $\mathbf{n} \in S_1$ for each $\mathbf{x}^\varphi \in \Omega^\varphi$. Then there exists a continuously differentiable tensor field $\mathbf{T}^\varphi : \mathbf{x}^\varphi \in \Omega^\varphi \rightarrow \mathbf{T}^\varphi(\mathbf{x}^\varphi) \in \mathbb{R}^{3 \times 3}$, such that*

$$\mathbf{t}^\varphi(\mathbf{x}^\varphi, \mathbf{n}) = \mathbf{T}^\varphi(\mathbf{x}^\varphi)\mathbf{n}$$

and

- 1) $-\operatorname{div} \mathbf{T}^\varphi = \mathbf{f}^\varphi$ in Ω^φ ,
- 2) $\mathbf{T}^\varphi \mathbf{n} = \mathbf{g}^\varphi$ on $\partial\Omega_N^\varphi$,
- 3) $(\mathbf{T}^\varphi)^\top = \mathbf{T}^\varphi$ in Ω^φ .

For the proof we refer the reader to [30]. We call \mathbf{T}^φ the Cauchy stress tensor. Cauchy's theorem is the very basis of the mathematical description of solid mechanics. 1) and 2) form a boundary value problem we need to solve in order to get the desired deformation \mathbf{u} for given forces \mathbf{f} and \mathbf{g} , while 3) already eliminates nearly half of the unknown entries of the tensor \mathbf{T} .

Piola-Kirchhoff stress tensors

Since the system is for the moment expressed with respect to \mathbf{x}^φ , we cannot use this in a sensible manner, since \mathbf{x}^φ is unknown itself. For this we introduce the *Piola transform* $\mathbf{T} : \Omega \rightarrow \mathbb{R}^{3 \times 3}$ with

$$\mathbf{T}(\mathbf{x}) = (\det D\varphi(\mathbf{x}))\mathbf{T}^\varphi(\mathbf{x}^\varphi)D\varphi(\mathbf{x})^{-\top}.$$

If this transform is applied on the Cauchy stress tensor \mathbf{T}^φ we call \mathbf{T} the *first Piola-Kirchhoff stress tensor*. With this we can transform the equations of equilibrium to a system of equations which is expressed in dependence of $\mathbf{x} \in \Omega$: The first Piola-Kirchhoff stress tensor satisfies the following equations,

$$-\operatorname{div} \mathbf{T} = \mathbf{f} \text{ in } \Omega, \quad (2.1)$$

$$\mathbf{T} \cdot \mathbf{n} = \mathbf{g} \text{ on } \partial\Omega_N, \quad (2.2)$$

$$D\varphi(\mathbf{T})^\top = \mathbf{T}D\varphi^\top \text{ in } \Omega. \quad (2.3)$$

The system is now still undetermined, since we have three equations for nine unknowns, three components of the deformation and six components of the stress tensor. To close this gap, we introduce material dependent constitutive equations.

2.3 Constitutive relations

The constitutive relations provide additional equations, which we need, to acquire a solvable system of differential equations. Since the three equations of Theorem 1 are valid in any material, it stands to reason to use material dependent properties to close the system. Otherwise all materials would act the same in our model, which would be an apparent contradiction to reality. For this introductory chapter we restrain the theory to elastic materials, however later in this work we will introduce non-elastic materials, namely materials with memory for plasticity and damage models.

Definition 2 (Elastic materials). *Elastic materials have the property that if a load, which induced a deformed state is lifted, they return to their initial state, whereas, for example, plastic materials return to an altered state if deformed beyond a certain limit.*

A material is called *elastic* if at each point \mathbf{x}^φ of the deformed configuration the Cauchy stress tensor $\mathbf{T}^\varphi(\mathbf{x}^\varphi)$ is a function that only depends on \mathbf{x}^φ and the deformation gradient $\mathbf{F}(\mathbf{x}^\varphi)$. For such materials there exists a mapping

$$\hat{\mathbf{T}} : (\mathbf{x}, \mathbf{F}) \in \bar{\Omega} \times \mathbb{M}_+^3 \rightarrow \text{sym}(3) := \mathbf{T} \in \mathbb{R}^{3 \times 3} : \mathbf{T} = \mathbf{T}^{-1},$$

called *response function for the Cauchy stress*, such that

$$\mathbf{T}^\varphi(\mathbf{x}^\varphi) = \hat{\mathbf{T}}(\mathbf{x}, \mathbf{D}\varphi(\mathbf{x})).$$

This relation is called the *constitutive equation of the material*.

We require that the response function is *objective/frame-indifferent*, i.e.

$$\hat{\mathbf{T}}(\mathbf{x}, \mathbf{Q}\mathbf{F}) = \mathbf{Q}\hat{\mathbf{T}}(\mathbf{x}, \mathbf{F})\mathbf{Q}^\top,$$

where \mathbf{Q} is again a rotation, which means that the response stays the same, if the observation point is changed or if the object is turned, as well as the acting forces.

The following properties are not required, but further specify types of elastic materials.

If the constitutive equation of the used material is only dependent of \mathbf{x} , i.e. $\hat{\mathbf{T}}(\mathbf{x}, \mathbf{F}) = \hat{\mathbf{T}}(\mathbf{F})$, it is called *homogeneous*, otherwise it is called *inhomogeneous*.

If the constitutive equation of the used material is invariant with respect to a rotation \mathbf{Q} , i.e. $\hat{\mathbf{T}}(\mathbf{x}, \mathbf{Q}\mathbf{F}) = \hat{\mathbf{T}}(\mathbf{x}, \mathbf{F})$, it is called *isotropic*, otherwise *anisotropic*.

Definition 3. The *second Piola-Kirchhoff stress* is defined by $\Sigma = \mathbf{F}^{-1}\mathbf{T}$.

Theorem 4. Let there be a homogeneous and isotropic elastic material, whose reference configuration is in a natural state. With sufficient smoothness of the material, there exist two constants μ and λ , such that the response function $\hat{\Sigma} : \mathbb{M}_+^3 \rightarrow \text{sym}(3)$ is of the form

$$\hat{\Sigma}(\mathbf{E}) = \lambda(\text{trace } \mathbf{E})\mathbf{I} + 2\mu\mathbf{E} + o(\mathbf{E}).$$

The constants μ and λ are known as *Lamé constants*. With them homogeneous, isotropic elastic materials can be described. By various experiments we are able to derive that the inequalities $\lambda > 0$ and $\mu > 0$ are required. There is

another system to describe such materials, we can use equivalently the *Poisson ratio* ν and *Young's modulus* E , with the relations

$$\begin{aligned}\nu &= \frac{\lambda}{2(\lambda + \mu)}, \\ E &= \frac{\mu(3\lambda + 2\mu)}{\lambda + \mu}, \\ \lambda &= \frac{E\nu}{(1 + \nu)(1 - 2\nu)}, \\ \mu &= \frac{E}{2(1 + \nu)},\end{aligned}$$

with the inequalities $E > 0$ and $0 < \nu < \frac{1}{2}$.

2.4 Linear elasticity

If we now assume that the forces are chosen such that the resulting deformations are sufficiently small, we can use the setting of linear elasticity, since terms of higher order vanish, which leaves us with the following set of equations, which will be used throughout this work, except for Chapter 6.

$$\operatorname{div} \boldsymbol{\sigma} = \mathbf{f}, \quad \text{in } \Omega, \quad (2.4a)$$

$$\boldsymbol{\sigma} \mathbf{n} = \mathbf{t}_N, \quad \text{on } \partial\Omega_N, \quad (2.4b)$$

$$\mathbf{u} = \mathbf{u}_D, \quad \text{on } \partial\Omega_D, \quad (2.4c)$$

and the constitutive relation $\boldsymbol{\sigma} = \boldsymbol{\sigma}(\mathbf{u})$. Here Ω^φ is approximated by Ω . For isotropic linear elasticity we have $\boldsymbol{\sigma} = \mathbb{C}\boldsymbol{\varepsilon}(\mathbf{u})$ depending on the linearized strain $\boldsymbol{\varepsilon}(\mathbf{u}) = \operatorname{sym}(\mathbf{D}\mathbf{u})$ and the elasticity tensor $\mathbb{C}\boldsymbol{\varepsilon} = 2\mu\boldsymbol{\varepsilon} + \lambda \operatorname{tr}(\boldsymbol{\varepsilon})\mathbf{I}$ depending on the Lamé parameters $\mu > 0$ and $\lambda \geq 0$.

Chapter 3

Numerical methods for linear elasticity

Content of this chapter In this chapter we discuss and analyze the weakly conforming method and briefly introduce two established methods, which have a vastly different approach of coupling the cells in which the discretized mesh Ω_h is divided, compared to the weakly conforming method. Additionally we will investigate the theoretical computational costs of all three methods.

Origin of this chapter Parts of the theoretical structure will be submitted with our SPP partners for a book chapter [15] within the final report of our SPP 1748; other theoretical aspects were published in [17].

3.1 Established methods and numerical setting

Finite element discretizations are based on the decomposition of a given domain $\Omega \subset \mathbb{R}^{\dim}$ with $\dim \in \{2, 3\}$ into open convex cells $K \in \mathcal{K}_h$, defined by $\Omega_h = \bigcup_{K \in \mathcal{K}_h} K$. Furthermore the skeleton is defined by $\partial\Omega_h = \overline{\Omega} \setminus \Omega_h$.

Variational formulation

To apply a finite element method, we cannot use the differential equation system directly, but rather consider the following weak formulation: Find $\mathbf{u} \in V(\mathbf{u}_D)$, where V is a suitable Sobolev space and $V(\mathbf{u}_D) = \{\mathbf{v} \in V : \mathbf{v} = \mathbf{u}_D \text{ on } \partial\Omega_D\}$, which minimizes the functional

$$J(\mathbf{v}) = \frac{1}{2}a(\mathbf{v}, \mathbf{v}) - \langle \ell, \mathbf{v} \rangle, \mathbf{v} \in V,$$

where

$$\begin{aligned} a(\cdot, \cdot) &= (\mathbb{C}\boldsymbol{\varepsilon}(\cdot), \boldsymbol{\varepsilon}(\cdot))_{0,\Omega}, \\ \langle \ell, \cdot \rangle &= (\mathbf{f}, \cdot)_{0,\Omega} + (\mathbf{t}_N, \cdot)_{0,\partial\Omega_N}. \end{aligned}$$

This is equivalent to the formulation: Find $\mathbf{u} \in V(\mathbf{u}_D)$ solving

$$a(\mathbf{u}, \mathbf{v}) = \langle \ell, \mathbf{v} \rangle, \quad \mathbf{v} \in V(\mathbf{0}). \quad (3.1)$$

For ℓ sufficiently smooth, a solution \mathbf{u} of this weak formulation is also a solution of equation (2.4). This is the case in all computations we consider.

Now we select locally in every cell $K \in \mathcal{K}_h$ a polynomial space $V_K \subset \mathbb{P}(K; \mathbb{R}^{\dim})$, e.g., $V_K = \mathbb{P}_1(K; \mathbb{R}^2)$ for linear elements on triangles, or bilinear polynomials on quadrilaterals. This defines the discontinuous space $V_h^{\text{dG}} = \prod_K V_K \subset \mathbb{P}(\Omega_h; \mathbb{R}^{\dim})$, and $a(\cdot, \cdot)$ extends to

$$a_h(\mathbf{u}_h, \mathbf{v}_h) = \sum_K (\mathbb{C}\boldsymbol{\varepsilon}(\mathbf{u}_h), \boldsymbol{\varepsilon}(\mathbf{v}_h))_{0,K}, \quad \mathbf{u}, \mathbf{v} \in H^1(\Omega_h; \mathbb{R}^{\dim}), \quad (3.2)$$

where $H^1(\Omega_h; \mathbb{R}^{\dim}) = \{\mathbf{v} \in L_2(\Omega; \mathbb{R}^{\dim}) : \mathbf{v}_K = \mathbf{v}|_K \in H^1(K; \mathbb{R}^{\dim}) \text{ for all } K\}$.

Conforming Galerkin method

Conforming methods use globally continuous ansatz functions, which inherently guarantee a continuous solution. As it is broadly accepted and as we will show within this work, there are upsides and downsides to this procedure. One major downside is the need for high numbers of degrees of freedom, when a problem has a non-smooth solution.

For the *conforming Galerkin method* we define

$$V_h^{\text{cf}} = V \cap V_h^{\text{dG}} \subset C^0(\bar{\Omega}; \mathbb{R}^{\text{dim}}),$$

and select the (continuous) ansatz functions in the space $V_h^{\text{cf}}(\mathbf{u}_{\text{D},h})$, which we define by

$$V_h^{\text{cf}}(\mathbf{u}_{\text{D},h}) = \left\{ \mathbf{v}_h \in V_h^{\text{cf}} : \mathbf{v}_h(x) = \mathbf{u}_{\text{D},h}(x) \text{ for all nodal points } x \in \partial\Omega_{\text{D}} \right\},$$

with a suitable continuous approximation $\mathbf{u}_{\text{D},h} \in C^0(\partial\Omega_{\text{D}}; \mathbb{R}^{\text{dim}})$ of the Dirichlet data, and the conforming discrete solution $\mathbf{u}_h^{\text{cf}} \in V_h^{\text{cf}}(\mathbf{u}_{\text{D},h})$ is determined by

$$a(\mathbf{u}_h^{\text{cf}}, \mathbf{v}_h) = \langle \ell, \mathbf{v}_h \rangle, \quad \mathbf{v}_h \in V_{0,h}^{\text{cf}} = V_h^{\text{cf}}(\mathbf{0}).$$

For conforming functions in $V = H^1(\Omega; \mathbb{R}^{\text{dim}})$, the inequalities by Poincaré and Korn

$$\|\mathbf{v}\|_{1,\Omega} \leq C_{\text{K}} \|\boldsymbol{\varepsilon}(\mathbf{v})\|_{0,\Omega}, \quad \mathbf{v} \in V(\mathbf{0}) \quad (3.3)$$

with $C_{\text{K}} > 0$ depending on Ω and $\partial\Omega_{\text{D}} \subset \partial\Omega$ yield

$$\|\mathbf{v}\|_{1,\Omega} \leq C_{\text{K}} \|\mathbb{C}^{-\frac{1}{2}}\|_{\infty,\Omega} |\mathbf{v}|_{\text{E},\Omega}, \quad \mathbf{v} \in V(0) \quad (3.4)$$

and thus coercivity of the bilinear form and convergence for *conforming* finite element approximations in $V_h \subset V$, see, e.g., [21, 24]. Here $|\mathbf{v}|_{\text{E},\Omega} = \sqrt{(\mathbb{C}\boldsymbol{\varepsilon}(\mathbf{v}), \boldsymbol{\varepsilon}(\mathbf{v}))_{0,\Omega}}$ is the energy (semi)-norm.

Discontinuous Galerkin method

Contrary to a conforming method, the *discontinuous Galerkin method* uses ansatz functions, which are, as the name implies, discontinuous. To ensure continuity between the cells for the solution, classical discontinuous methods use penalty parameter. There are many established forms; in this work we use the *symmetric interior penalty method*, see, e.g., [39], as a benchmark method.

For the discontinuous Galerkin method, the bilinear form $a(\cdot, \cdot)$ is extended to $a_h^{\text{dG}}(\cdot, \cdot)$ and the discrete solution $\mathbf{u}_h^{\text{dG}} \in V_h^{\text{dG}}$ is determined by

$$a_h^{\text{dG}}(\mathbf{u}_h^{\text{dG}}, \mathbf{v}_h) = \langle \ell_h^{\text{dG}}, \mathbf{v}_h \rangle, \quad \mathbf{v}_h \in V_h^{\text{dG}}. \quad (3.5)$$

Let \mathcal{F}_K be the set of faces $F \subset \partial K$ and define $\mathcal{F}_h = \cup \mathcal{F}_K$. We assume that $\partial\Omega_D = \overline{\cup_{F \subset \partial\Omega_D} F}$, so that the mesh resolves the boundary decomposition. We set $h_F = \text{diam } F$ and we select a fixed orientation \mathbf{n}_F . For inner faces $F \in \mathcal{F}_K \cap \Omega$ let K_F be the neighboring cell. Finally, we set $h_K = \text{diam}(K)$ and $h = \max h_K$. We observe for the solution of (2.4) and broken test functions $\mathbf{v} \in H^1(\Omega_h; \mathbb{R}^{\text{dim}})$

$$\begin{aligned} \langle \ell, \mathbf{v}_h \rangle &= \left(-\text{div } \boldsymbol{\sigma}(\mathbf{u}), \mathbf{v}_h \right)_{0,\Omega} + \left(\boldsymbol{\sigma}(\mathbf{u})\mathbf{n}_K, \mathbf{v}_h \right)_{0,\partial\Omega_N} \\ &= \sum_K \left(\left(\mathbb{C}\boldsymbol{\varepsilon}(\mathbf{u}), \boldsymbol{\varepsilon}(\mathbf{v}_K) \right)_{0,K} - \sum_{F \in \mathcal{F}_K \setminus \partial\Omega_N} \left(\boldsymbol{\sigma}(\mathbf{u})\mathbf{n}_K, \mathbf{v}_K \right)_{0,F} \right) \\ &= a_h(\mathbf{u}, \mathbf{v}_h) - \sum_{F \in \mathcal{F}_h \setminus \partial\Omega_N} \left(\boldsymbol{\sigma}(\mathbf{u}), \llbracket \mathbf{v}_h \rrbracket_F \right)_{0,F}, \end{aligned} \quad (3.6)$$

with jump terms $\llbracket \mathbf{v}_h \rrbracket_F = \mathbf{v}_K \otimes \mathbf{n}_K + \mathbf{v}_{K_F} \otimes \mathbf{n}_{K_F}$ on inner faces $F = \partial K \cap \partial K_F$ and $\llbracket \mathbf{v}_h \rrbracket_F = \mathbf{v}_K \otimes \mathbf{n}_K$ on boundary faces $F = \partial K \cap \partial\Omega$ using $\mathbf{v}_K = \mathbf{v}_h|_K$, and where $\mathbf{a} \otimes \mathbf{b} = (a_i b_j)_{i,j=1,\dots,\text{dim}}$ denotes the tensor product for vectors $\mathbf{a} = (a_i)_{i=1,\dots,\text{dim}}$ and $\mathbf{b} = (b_j)_{j=1,\dots,\text{dim}}$.

For the symmetric interior penalty method a consistent extension of (3.6) to discontinuous ansatz functions is defined by

$$\begin{aligned} a_h^{\text{dG}}(\mathbf{u}_h, \mathbf{v}_h) &= a_h(\mathbf{u}, \mathbf{v}_h) \\ &\quad - \sum_{F \in \mathcal{F}_h \setminus \partial\Omega_N} \left(\left(\{\{\boldsymbol{\sigma}(\mathbf{u}_h)\}\}_F, \llbracket \mathbf{v}_h \rrbracket_F \right)_{0,F} + \left(\llbracket \mathbf{u}_h \rrbracket_F, \{\{\boldsymbol{\sigma}(\mathbf{v}_h)\}\}_F \right)_{0,F} \right) \\ &\quad + \sum_{F \in \mathcal{F}_h \setminus \partial\Omega_N} \frac{\theta}{h_F} \left(\llbracket \mathbf{u}_h \rrbracket_F, \llbracket \mathbf{v}_h \rrbracket_F \right)_{0,F}, \end{aligned} \quad (3.7)$$

$$\langle \ell_h^{\text{dG}}, \mathbf{v}_h \rangle = \langle \ell, \mathbf{v}_h \rangle + \sum_{F \in \mathcal{F}_h \cap \partial\Omega_D} \frac{\theta}{h_F} \left(\mathbf{u}_D, \mathbf{v}_h \right)_{0,F}$$

depending on a penalty parameter $\theta > 0$ and with $\{\{\boldsymbol{\sigma}_h\}\}_F = \frac{1}{2}(\boldsymbol{\sigma}_K + \boldsymbol{\sigma}_{K_F})$ on inner faces $F = \partial K \cap \partial K_F$ and $\{\{\boldsymbol{\sigma}_h\}\}_F = \boldsymbol{\sigma}_K$ on $F = \partial K \cap \partial\Omega$. The penalty parameter has to be carefully balanced for each different computation. If chosen too large, the penalty term becomes dominant and the method effectively behaves like a continuous method, with the disadvantage of having far more degrees of freedom and a much more dense global system matrix. If the parameter is chosen too small, the bilinear form is not coercive, this holds only true for $\theta \geq \theta_0 > 0$, where θ_0 depends on the polynomial degree and the shape regularity [39, Prop. 3]. Finite element convergence of the non-conforming method is established with robust estimates for the incompressible

limit [39, Thm. 8], and energy norm a posteriori error estimation is addressed in [19].

3.2 Weakly conforming method

The weakly conforming method uses a generalized conception of continuity between cells. To get rid of the penalty parameters, which are a key feature of other non-conforming methods like the discontinuous Galerkin method, and to avoid the task of parameter balancing, continuity is not enforced by a system of penalty parameters, but in a weak sense.

For the *weakly conforming method*, the ansatz space is constraint to $V_h^{\text{wc}} \subset V_h^{\text{dG}}$, and the discrete solution $\mathbf{u}_h^{\text{wc}} \in V_h^{\text{wc}}(\mathbf{u}_D)$ is determined by

$$a_h(\mathbf{u}_h^{\text{wc}}, \mathbf{v}_h) = \langle \ell, \mathbf{v}_h \rangle, \quad \mathbf{v}_h \in V_{0,h}^{\text{wc}} = V_h^{\text{wc}}(\mathbf{0}). \quad (3.8)$$

We select on every face a multiplier space $M_F \subset \mathbb{P}(F; \mathbb{R}^{\text{dim}})$ as an ansatz space and we define

$$V_h^{\text{wc}} = \left\{ \mathbf{v}_h \in V_h^{\text{dG}} : (\mathbf{v}_K, \boldsymbol{\mu}_F)_{0,F} = (\mathbf{v}_{K_F}, \boldsymbol{\mu}_F)_{0,F} \text{ for } \boldsymbol{\mu}_F \in M_F, F \in \mathcal{F}_h \cap \Omega \right\},$$

where K_F is the neighboring cell of K , which shares the face F . This definition already explains how the cells are weakly coupled for this method. As for the other methods, we select the ansatz functions not in the whole space V_h^{wc} , but rather define a subspace, where the Dirichlet conditions are fulfilled, i.e.

$$V_h^{\text{wc}}(\mathbf{u}_D) = \left\{ \mathbf{v}_h \in V_h^{\text{wc}} : (\mathbf{v}_h, \boldsymbol{\mu}_F)_{0,F} = (\mathbf{u}_D, \boldsymbol{\mu}_F)_{0,F} \text{ for } \boldsymbol{\mu}_F \in M_F, F \in \mathcal{F}_h \cap \partial\Omega_D \right\},$$

and use this subspace as an ansatz space.

3.3 Choice of local multiplier spaces

We note that for all choices of $M_h = \prod_{F \in \mathcal{F}_h \setminus \partial\Omega_N} M_F$ we get $V_h^{\text{cf}} \subset V_h^{\text{wc}} \subset V_h^{\text{dG}}$. However, only for M_h large enough the broken bilinear form (3.2) is coercive and the consistency error is at least of the same order as the best approximation error. On the other hand, if M_h is too large, we get $V_h^{\text{cf}} = V_h^{\text{wc}}$ and we cannot profit from the improved robustness properties of nonconforming

schemes, additionally no local static condensation to face degrees of freedom is possible.

For the *weakly conforming method*, the coercivity of the broken bilinear form (3.2) requires a sufficient large number of constraints per face so that piecewise rigid body modes are globally continuous: we need at least as many face constraints as rigid body modes per cell. A possible and sufficient condition is $\mathbb{P}_1(F; \mathbb{R}^{\dim}) \subset M_F$ for all $F \in \mathcal{F}_h \setminus \partial\Omega_N$. Then, (3.3) extends to $\mathbf{v}_h \in V_{0,h}^{\text{wc}}$, see [23]. It is known from [42] that the most simple choice $M_F = \mathbb{P}_0(F; \mathbb{R}^{\dim})$ yields an h -dependent constant, hence is insufficient. However, only few degrees of freedom are missing as the following lemma shows that for $\dim = 2$ the choice $M_F = M_F^{\min} = \mathbb{P}_0(F; \mathbb{R}^{\dim}) + \mathbf{n}_F \mathbb{P}_1(F)$ is sufficient. For $\dim = 3$ the basis must be extended by the in-face rotation, i.e.,

$$M_F^{\min} = \mathbb{P}_0(F; \mathbb{R}^{\dim}) + \mathbf{n}_F \mathbb{P}_1(F) + \text{span } \mathbf{v}_F^r, \quad \mathbf{v}_F^r(\mathbf{x}) = \mathbf{n}_F \times \mathbf{x}. \quad (3.9)$$

Lemma 5. *If $M_F^{\min} \subset M_F$ for all $F \in \mathcal{F}_h \setminus \partial\Omega_N$, a constant $\hat{C}_K > 0$ only depending on the mesh regularity exists such that*

$$\|\mathbf{v}_h\|_{1,\Omega_h} \leq \hat{C}_K \|\boldsymbol{\varepsilon}(\mathbf{v}_h)\|_{0,\Omega_h}, \quad \mathbf{v}_h \in V_{0,h}^{\text{wc}}. \quad (3.10)$$

For the proof of this lemma we refer to [44].

When we choose at least $M_F = \mathbb{P}_1(F; \mathbb{R}^{\dim})$, we can use the result in [23], where (3.10) is shown for larger face multiplier spaces satisfying $\mathbb{P}_1(F; \mathbb{R}^{\dim}) \subset M_F$.

3.4 Static condensation

The efficient implementation is based on a hybrid formulation. This enables us to cut all inner-cell nodal points, which reduces the global system matrix to the size of the skeleton degrees of freedom. Moreover, the approximation error is limited by the polynomial order of the multiplier spaces, and additional cell degrees of freedom only increase the robustness but not the approximation order. Using the local L_2 -projection $\hat{\Pi}_F^{\text{wc}}: L_2(F; \mathbb{R}^{\dim}) \rightarrow M_F$, we note that by the definition of the weakly conforming space V_h^{wc} the skeleton projection $\hat{\Pi}_h^{\text{wc}} \mathbf{v} = \left(\hat{\Pi}_F^{\text{wc}} \mathbf{v}_F \right)_{F \in \mathcal{F}_h \setminus \partial\Omega_N}$ is well-defined on V_h^{wc} , i.e., $\hat{\Pi}_F^{\text{wc}} \mathbf{v}_K = \hat{\Pi}_F^{\text{wc}} \mathbf{v}_{K_F}$ for

$F \in \mathcal{F}_h \cap \Omega$ and $\mathbf{v}_h \in V_h^{\text{wc}}$. Our implementation is based on the observation

$$V_h^{\text{wc}} = \left\{ \mathbf{v}_h \in V_h^{\text{dG}} : \hat{\mathbf{v}}_h \in M_h \text{ exists such that } \hat{\Pi}_K^{\text{wc}} \mathbf{v}_K = \hat{\mathbf{v}}_K \text{ for all } K \right\} \quad (3.11)$$

with $\hat{\Pi}_K^{\text{wc}} \mathbf{v}_K = \left(\hat{\Pi}_F^{\text{wc}} \mathbf{v}_F \right)_{F \in \mathcal{F}_K \setminus \partial\Omega_N}$ and $\hat{\mathbf{v}}_K = \left(\hat{\mathbf{v}}_F \right)_{F \in \mathcal{F}_K \setminus \partial\Omega_N}$. Moreover, the skeleton projection maps $V_h^{\text{wc}}(\mathbf{u}_D)$ onto

$$M_h(\mathbf{u}_D) = \left\{ \hat{\mathbf{v}}_h \in M_h : \hat{\mathbf{v}}_F = \hat{\Pi}_F^{\text{wc}} \mathbf{u}_D \text{ for all } F \in \mathcal{F}_h \cap \partial\Omega_D \right\}. \quad (3.12)$$

The hybrid method is obtained by minimizing

$$J_h(\mathbf{v}_h) = \frac{1}{2} a_h(\mathbf{v}_h, \mathbf{v}_h) - (\mathbf{f}, \mathbf{v}_h)_{0,\Omega} + (\mathbf{t}_N, \mathbf{v}_h)_{0,\partial\Omega_N} \quad (3.13)$$

in $V_h^{\text{wc}}(\mathbf{u}_D)$ or, equivalently, in V_h^{dG} subject to the constraints in (3.11) and (3.12). Therefore we compute a critical point of the corresponding saddle point functional

$$\Phi_h(\mathbf{v}_h, \hat{\mathbf{v}}_h, (\boldsymbol{\mu}_K)_K) = \frac{1}{2} \sum_K \left(\langle A_K \mathbf{v}_K, \mathbf{v}_K \rangle - \langle \ell_K, \mathbf{v}_K \rangle + \langle B_K \mathbf{v}_K - \hat{B}_K \hat{\mathbf{v}}_K, \boldsymbol{\mu}_K \rangle \right) \quad (3.14)$$

for $(\mathbf{v}_h, \hat{\mathbf{v}}_h, (\boldsymbol{\mu}_K)_K) \in V_h^{\text{dG}} \times M_h(\mathbf{u}_D) \times \prod_K M_K$, where

$$\begin{aligned} A_K &\in \mathcal{L}(V_K, V'_K), & \langle A_K \mathbf{u}_K, \mathbf{v}_K \rangle &= (\mathbf{C}\boldsymbol{\varepsilon}(\mathbf{u}_h), \boldsymbol{\varepsilon}(\mathbf{v}_h))_{0,K}, \\ B_K &\in \mathcal{L}(V_K, M'_K), & \langle B_K \mathbf{v}_K, \boldsymbol{\mu}_K \rangle &= (\mathbf{v}_K, \boldsymbol{\mu}_K)_{0,\partial K \setminus \partial\Omega_N}, \\ \hat{B}_K &\in \mathcal{L}(M_K, M'_K), & \langle \hat{B}_K \hat{\mathbf{v}}_K, \boldsymbol{\mu}_K \rangle &= (\hat{\mathbf{v}}_K, \boldsymbol{\mu}_K)_{0,\partial K \setminus \partial\Omega_N}, \\ \ell_K &\in V'_K, & \langle \ell_K, \mathbf{v}_K \rangle &= (\mathbf{f}, \mathbf{v}_K)_{0,K} + (\mathbf{t}_N, \mathbf{v}_K)_{0,\partial K \cap \partial\Omega_N}. \end{aligned}$$

Lemma 6. *Assume that (3.10) is satisfied, and that $\hat{\Pi}_h^{\text{wc}}(V_h^{\text{wc}}) = M_h$ is surjective.*

Then, a saddle point $(\mathbf{u}_h^{\text{wc}}, \hat{\mathbf{u}}_h^{\text{wc}}, (\boldsymbol{\lambda}_K^{\text{wc}})_K) \in V_h^{\text{dG}} \times M_h(\mathbf{u}_D) \times \prod_K M_K$ of (3.14) exists solving locally for all K

$$A_K \mathbf{u}_K^{\text{wc}} + B'_K \boldsymbol{\lambda}_K^{\text{wc}} = \ell_K, \quad (3.15a)$$

$$B_K \mathbf{u}_K^{\text{wc}} = \hat{B}_K \hat{\mathbf{u}}_K^{\text{wc}}, \quad (3.15b)$$

with the global constraint

$$\sum_K \langle \hat{B}_K \hat{\mathbf{v}}_K, \boldsymbol{\lambda}_K^{\text{wc}} \rangle = 0, \quad \hat{\mathbf{v}}_h \in M_{0,h} = M_h(\mathbf{0}). \quad (3.15c)$$

Moreover, $\mathbf{u}_h^{\text{wc}} \in V_h^{\text{wc}}(\mathbf{u}_D)$ is the solution of (3.8).

Proof. Coercivity of the quadratic functional (3.13) follows from (3.10), so that a unique minimizer $\mathbf{u}_h^{\text{wc}} \in V_h^{\text{wc}}(\mathbf{u}_D)$ exists characterized by

$$\sum_K \left(\langle A_K \mathbf{u}_K^{\text{wc}}, \mathbf{v}_K \rangle - \langle \ell_K, \mathbf{v}_K \rangle \right) = 0, \quad \mathbf{v}_h \in V_{0,h}^{\text{wc}}. \quad (3.16)$$

Then, defining $\hat{\mathbf{u}}_h^{\text{wc}} = \hat{\Pi}_h^{\text{wc}} \mathbf{u}_h \in M_h(\mathbf{u}_D)$ yields $B_K \mathbf{u}_K^{\text{wc}} = \hat{B}_K \hat{\mathbf{u}}_K^{\text{wc}}$ for all K and thus (3.15b). Now we show that Lagrange parameters $\boldsymbol{\lambda}_K^{\text{wc}} \in M_K$ exist so that $(\mathbf{u}_h^{\text{wc}}, \hat{\mathbf{u}}_h^{\text{wc}}, (\boldsymbol{\lambda}_K^{\text{wc}})_K)$ solves (3.15).

We define $\mathcal{N}(B_K) = \left\{ \mathbf{v}_K \in V_K : B_K \mathbf{v}_K = \mathbf{0} \right\}$. This gives

$$V_{0,h}^{\text{wc}} \supset \left\{ \mathbf{v}_h \in V_h^{\text{dG}} : \mathbf{v}_K \in \mathcal{N}(B_K) \text{ for all } K \right\},$$

so that we obtain locally $\langle A_K \mathbf{u}_K^{\text{wc}}, \mathbf{v}_K \rangle = \langle \ell_K, \mathbf{v}_K \rangle$ for $\mathbf{v}_K \in \mathcal{N}(B_K)$ and

$$\begin{aligned} \boldsymbol{\lambda}'_K &= \ell_K - A_K \mathbf{u}_K^{\text{wc}} \in \mathcal{N}(B_K)^\perp \\ &= \left\{ \boldsymbol{\mu}'_K \in V'_K : \langle \boldsymbol{\mu}'_K, \mathbf{v}_K \rangle = 0 \text{ for all } \mathbf{v}_K \in \mathcal{N}(B_K) \right\}. \end{aligned}$$

By duality, $\boldsymbol{\lambda}'_K \in \mathcal{R}(B'_K)$, i.e., $\boldsymbol{\lambda}_K^{\text{wc}} \in M_K$ exists such that $B'_K \boldsymbol{\lambda}_K^{\text{wc}} = \boldsymbol{\lambda}'_K$.

This gives (3.15a), and for $\hat{\mathbf{v}}_h = \hat{\Pi}_h^{\text{wc}} \mathbf{v}_h \in M_{0,h}$ with $\mathbf{v}_h \in V_{0,h}^{\text{wc}}$, we obtain

$$\sum_K \langle \hat{B}_K \hat{\mathbf{v}}_K, \boldsymbol{\lambda}_K^{\text{wc}} \rangle = \sum_K \langle \mathbf{v}_K, \boldsymbol{\lambda}_K^{\text{wc}} \rangle_{0,\partial K} = \sum_K \left(\langle A_K \mathbf{u}_K^{\text{wc}}, \mathbf{v}_K \rangle - \langle \ell_K, \mathbf{v}_K \rangle \right) = 0.$$

Since $\hat{\Pi}_h^{\text{wc}}$ is surjective, this shows (3.15c). \square

When A_K is invertible on $\mathcal{N}(B_K)$ and B_K is surjective, cf. Sec. 3.5, the discrete local problem (3.15a) and (3.15b) has a unique solution

$$\begin{pmatrix} \mathbf{u}_K \\ \boldsymbol{\lambda}_K \end{pmatrix} = \begin{pmatrix} A_K & B'_K \\ B_K & 0 \end{pmatrix}^{-1} \begin{pmatrix} \ell_K \\ \hat{B}_K \hat{\mathbf{u}}_h \end{pmatrix}, \quad (3.17)$$

and inserting into (3.15c) this yields for the skeleton approximation $\hat{\mathbf{u}}_h^{\text{wc}} \in M_h(\mathbf{u}_D)$

$$\hat{a}_h(\hat{\mathbf{u}}_h^{\text{wc}}, \hat{\mathbf{v}}_h) = \langle \hat{\ell}_h, \hat{\mathbf{v}}_h \rangle, \quad \hat{\mathbf{v}}_h \in M_{0,h} \quad (3.18)$$

with

$$\begin{aligned} \hat{a}_h(\hat{\mathbf{u}}_h, \hat{\mathbf{v}}_h) &= \sum_K \begin{pmatrix} 0 \\ \hat{B}'_K \end{pmatrix}^\top \begin{pmatrix} A_K & B'_K \\ B_K & 0 \end{pmatrix}^{-1} \begin{pmatrix} 0 \\ \hat{B}_K \end{pmatrix}, \\ \hat{\ell}_h &= \sum_K \begin{pmatrix} 0 \\ \hat{B}'_K \end{pmatrix}^\top \begin{pmatrix} A_K & B'_K \\ B_K & 0 \end{pmatrix}^{-1} \begin{pmatrix} \ell_K \\ 0 \end{pmatrix}. \end{aligned}$$

The bilinear form $\hat{a}_h(\cdot, \cdot)$ is symmetric, and we now show that it is also positive definite. For $\hat{\mathbf{v}}_h \in M_{0,h}$ we define locally in K

$$\begin{pmatrix} \mathbf{v}_K \\ \boldsymbol{\mu}_K \end{pmatrix} = \begin{pmatrix} A_K & B'_K \\ B_K & 0 \end{pmatrix}^{-1} \begin{pmatrix} 0 \\ \hat{B}_K \hat{\mathbf{v}}_h \end{pmatrix} \in V_K \times M_K.$$

We observe $\mathbf{v}_h \in V_{0,h}^{\text{wc}}$ and $\hat{\mathbf{v}}_h = \hat{\Pi}_h^{\text{wc}} \mathbf{v}_h$, and using (3.15c), we obtain

$$\begin{aligned} \hat{a}_h(\hat{\mathbf{v}}_h, \hat{\mathbf{v}}_h) &= \sum_K \left\langle \begin{pmatrix} A_K & B'_K \\ B_K & 0 \end{pmatrix}^{-1} \begin{pmatrix} 0 \\ B_K \mathbf{v}_h \end{pmatrix}, \begin{pmatrix} 0 \\ B_K \mathbf{v}_h \end{pmatrix} \right\rangle \\ &= \sum_K \left\langle \begin{pmatrix} A_K & B'_K \\ B_K & 0 \end{pmatrix} \begin{pmatrix} \mathbf{v}_K \\ \boldsymbol{\mu}_K \end{pmatrix}, \begin{pmatrix} \mathbf{v}_K \\ \boldsymbol{\mu}_K \end{pmatrix} \right\rangle \\ &= \sum_K \left(\langle A_K \mathbf{v}_K, \mathbf{v}_K \rangle + 2 \langle B_K \mathbf{v}_K, \boldsymbol{\mu}_K \rangle \right) = a_h(\mathbf{v}_h, \mathbf{v}_h). \end{aligned}$$

This local reconstruction can also be used to define an interpolation into the weakly conforming space: given $\mathbf{u} \in H^1(\Omega, \mathbb{R}^{\dim})$, we define $\Pi_h^{\text{wc}} \mathbf{u} \in V_h^{\text{wc}}$ and $\Lambda_K^{\text{wc}} \mathbf{u} \in M_K$ locally by

$$\begin{pmatrix} \Pi_K^{\text{wc}} \mathbf{u} \\ \Lambda_K^{\text{wc}} \mathbf{u} \end{pmatrix} = \begin{pmatrix} A_K & B'_K \\ B_K & 0 \end{pmatrix}^{-1} \begin{pmatrix} \ell_K \\ \hat{B}_K \hat{\Pi}_K^{\text{wc}} \mathbf{u} \end{pmatrix}. \quad (3.19)$$

3.5 Choice of local cell spaces

After a sensible choice of M_h is made, we need to look at its relation to the local spaces V_K . Obviously we want the local saddle-point matrices to be regular, since we want to invert them.

The weakly conforming method needs in each cell at least as many degrees of freedom in the cells, as it has on all the faces of this cell combined, since $B_K \in \mathbb{R}^{n \times m}$ with $n = |V_K|$ and $m = \sum_{F \in \mathcal{F}_K} |M_F|$ and if $n < m$ the local saddle point matrices cannot be regular, cf. [20]. In Tab. 3.1 some stable pairings for two-dimensional meshes consisting of triangles or quadrilaterals can be seen. Since we have no sharp condition, of what p has to be in $\mathbb{P}_p(K, \mathbb{R}^{\dim}) \subset V_K$ for every choice of M_h , these pairings are numerically tested. Note, that the inner degree can be increased without causing numerical instabilities. However, this is usually not recommended, since this does not increase the quality of the solution but does increase the computational cost. However, in some numerical

Triangles	$\mathbb{P}_2\mathbb{P}_{1+}$	$\mathbb{P}_2\mathbb{P}_2$	$\mathbb{P}_3\mathbb{P}_3$	$\mathbb{P}_4\mathbb{P}_4$	$\mathbb{P}_4\mathbb{P}_5$
$n m$	12 9	12 12	20 18	30 24	30 30
Quadrilaterals	$\mathbb{P}_2\mathbb{P}_{1+}$	$\mathbb{P}_3\mathbb{P}_2$	$\mathbb{P}_4\mathbb{P}_3$	$\mathbb{P}_5\mathbb{P}_4$	$\mathbb{P}_6\mathbb{P}_5$
$n m$	18 12	32 16	50 24	72 32	98 40

Table 3.1: Possible numerical stable pairings of $V_K|M_K$ for triangular and quadrilateral elements.

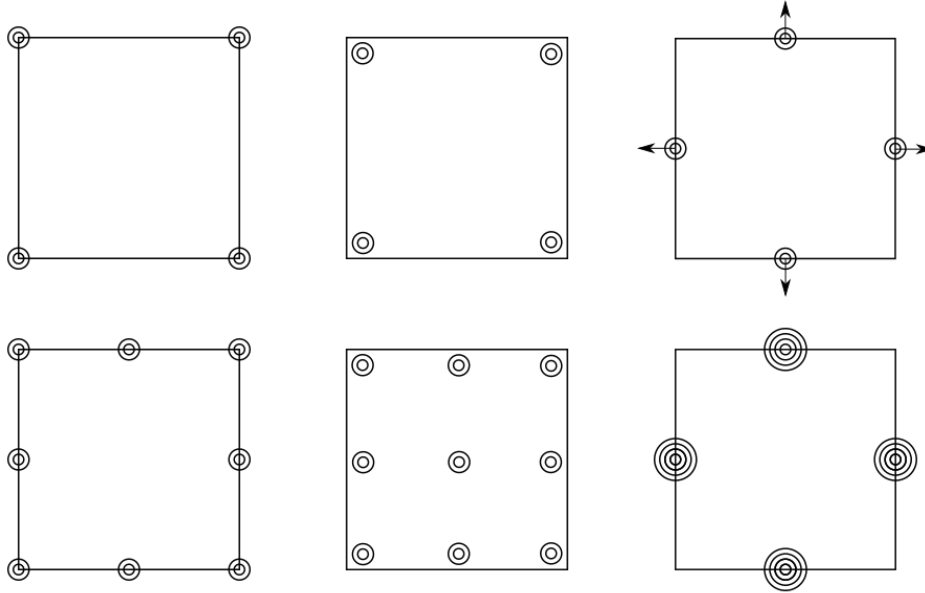


Figure 3.1: Quadrilateral meshes: Degrees of freedom on individual cells for all lowest order (top) and higher order (bottom) schemes: conforming (left), discontinuous Galerkin (middle) and weakly conforming (right).

tests this has increased the robustness of the weakly conforming method, cf. the thin beam example in Sec. 4.3.

3.6 Numerical costs compared to established methods

For the evaluation of the numerical cost for the different methods we have to quantify the approximation error in comparison to the degrees of freedom in the global linear system. The degrees of freedom in 2d are illustrated in Fig. 3.1 and Fig. 3.2 and an overview of the numerical costs for large meshes

Quadrilaterals			
Discretization	DoFs per cell	total DoFs	matrix entries per row
conforming Serendepity \mathbb{Q}_1	2 per vertex	$2 \cdot N_{\mathcal{K}_h}$	18
conforming Serendepity \mathbb{Q}_2	2 per vertex, 2 per edge	$6 \cdot N_{\mathcal{K}_h}$	42
conforming Serendepity \mathbb{Q}_3	2 per vertex, 4 per edge	$10 \cdot N_{\mathcal{K}_h}$	70
linear dG	8 per cell	$8 \cdot N_{\mathcal{K}_h}$	40
quadratic dG	18 per cell	$18 \cdot N_{\mathcal{K}_h}$	90
cubic dG	32 per cell	$32 \cdot N_{\mathcal{K}_h}$	160
$\mathbb{P}_2\mathbb{P}_{0+}$ hybrid wc	3 per face	$6 \cdot N_{\mathcal{K}_h}$	21
$\mathbb{P}_3\mathbb{P}_1$ hybrid wc	4 per face	$8 \cdot N_{\mathcal{K}_h}$	28
$\mathbb{P}_4\mathbb{P}_2$ hybrid wc	6 per face	$12 \cdot N_{\mathcal{K}_h}$	42
Triangles			
conforming \mathbb{P}_1	2 per vertex	$2 \cdot N_{\mathcal{K}_h}$	18
conforming \mathbb{P}_2	2 per vertex, 2 per edge	$6 \cdot N_{\mathcal{K}_h}$	50
conforming \mathbb{P}_3	2 per vertex, 4 per edge, 1 inside the cell	$10 \cdot N_{\mathcal{K}_h}$	98
linear dG	6 per cell	$6 \cdot N_{\mathcal{K}_h}$	32
quadratic dG	12 per cell	$12 \cdot N_{\mathcal{K}_h}$	60
cubic dG	20 per cell	$20 \cdot N_{\mathcal{K}_h}$	80
$\mathbb{P}_2\mathbb{P}_{0+}$ hybrid wc	3 per face	$6 \cdot N_{\mathcal{K}_h}$	15
$\mathbb{P}_3\mathbb{P}_1$ hybrid wc	4 per face	$8 \cdot N_{\mathcal{K}_h}$	20
$\mathbb{P}_4\mathbb{P}_2$ hybrid wc	6 per face	$12 \cdot N_{\mathcal{K}_h}$	30

Table 3.2: Allocation and asymptotic number of the degrees of freedom (DoFs) and matrix entries per row for the condensed system on uniform meshes (dim = 2) with $N_{\mathcal{K}_h}$ cells.

is given in Tab. 3.2:

- The ansatz functions for linear conforming \mathbb{P}_1 elements and for bilinear conforming \mathbb{Q}_1 elements methods are defined by the nodal values on the vertices in \mathbb{R}^{\dim} , and for the quadratic \mathbb{P}_1 elements on simplices or Serendipity \mathbb{Q}_2 elements on quadrilaterals and hexahedra in addition on the edge midpoints. The matrix graph couples all degrees of freedom of cells connected by a nodal point.
- Discontinuous elements use the same degrees of freedom independently on every cell. The matrix graph couples all degrees of freedom of the cells connected by a face; this becomes especially expensive for high degrees of freedom, where the system matrix is extremely dense compared to the other methods and requires a lot of memory.
- The lowest order hybrid method $\mathbb{P}_2\mathbb{P}_{0+}$ requires $\dim + 1$ degrees of freedom per face, which is combined with quadratic polynomials in the cells, i.e., we use $M_F = \mathbb{P}_0(F; \mathbb{R}^{\dim}) + \mathbf{n}_F\mathbb{P}_1(F)$ and $V_h^{\text{dG}} = \mathbb{P}_2(\Omega_h)$. The $\mathbb{P}_3\mathbb{P}_1$ hybrid method uses linear multiplier on the faces and discontinuous cubic polynomials in the cells. The matrix graph only couples degrees of freedom on faces with cells with shared faces. However, the overall numerical costs are higher than it appears here, since the local degrees of freedom are not counted here. The local degrees of freedom can be much higher, depending on the choice of degree pairing, cf. Tab. 3.1, but they are only needed to assemble the local saddle point matrices and only increase the assembly time, not the time which the global solver needs, which can be efficiently parallelized, cf. Table 3.3.

In the following tests, the linear, bilinear and lowest order hybrid method are denoted by $V_{h,1}^{\text{cf}}$, $V_{h,1}^{\text{dG}}$, $M_{h,1}^{\text{wc}}$, respectively, and the higher order families are denoted by $V_{h,2}^{\text{cf}}$, $V_{h,2}^{\text{dG}}$, $M_{h,2}^{\text{wc}}$.

In our numerical tests, we investigate the approximation error of the different discretizations with respect to the L_2 norm and the energy (semi)-norm

$$\|\mathbf{v}\|_{0,\Omega} = \sqrt{(\mathbf{v}, \mathbf{v})_{0,\Omega}}, \quad |\mathbf{v}|_{\mathbf{E},\Omega_h} = \sqrt{(\mathbb{C}\boldsymbol{\varepsilon}(\mathbf{v}), \boldsymbol{\varepsilon}(\mathbf{v}))_{0,\Omega_h}}. \quad (3.20)$$

Note that $\|\cdot\|_{\mathbf{E}} = |\cdot|_{\mathbf{E},\Omega_h}$ is a norm in $V_h^{\text{cf}} \subset V$ and in V_h^{wc} (see the conditions in Chapter 5) but only a seminorm in V_h^{dG} .

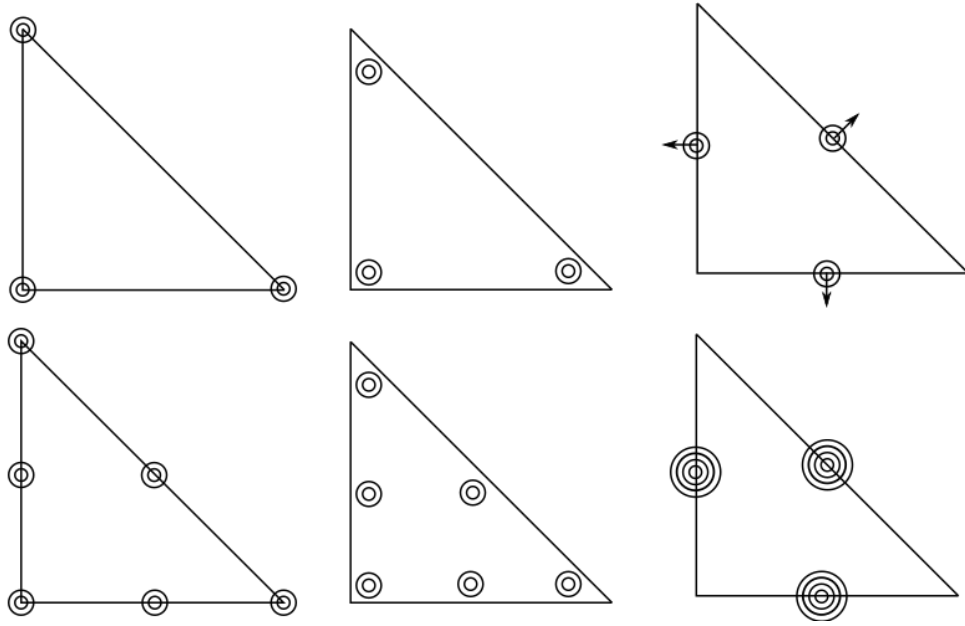


Figure 3.2: Triangular meshes: Degrees of freedom on individual cells for all lowest order (top) and higher order (bottom) schemes: conforming (left), discontinuous Galerkin (middle) and weakly conforming (right).

3.7 Implementation of the weakly conforming method

The described method was implemented in the parallel finite element framework M++, which was introduced and is administered by Christian Wieners [58, 14]. M++ is an open-source parallel finite element software, which is developed since 15 years by the staff of the research group scientific computing at the Karlsruhe Institute of Technology. As a solver we used the parallel block LU decomposition method as a preconditioner introduced by Daniel Maurer and Christian Wieners in [49], which employs a parallel block LU decomposition, and the generalized minimal residual method as a solver. Of course other solvers and preconditioners can be utilized as well, especially since the global system matrix is positive definite and symmetric.

Within the M++ library we implemented the weakly conforming method, which included the implementation of several element variants, for the broad spectrum of discussed models. Furthermore we implemented high order shape

Number of process	1	4	16	64	256	Overall
Assemble time (s)	38.15	9.58	3.04	0.96	0.26	
Speedup		3.98	3.15	3.17	3.69	146.73
Solving time (s)	196.74	50.86	15.72	5.22	2.43	
Speedup		3.87	3.23	3.01	2.15	80.96
Total time (s)	938.42	238.69	74.55	24.58	9.27	
Speedup		3.93	3.20	3.03	2.65	101.23

Table 3.3: Computation times for a small linear problem, computed with varying numbers of parallel processes, including overall speedup if computing with 256 cores instead of 1.

functions for triangles, quadrilaterals, tetrahedra and hexahedra to utilize high order approximations, especially for the case of p -adaptive refinement. And to integrate the new shapes without errors we needed to implement high order Gaussian quadratures for each shape.

In Table 3.3 a short overview of assemble time, solving time and total time is given for various number of processes, while computing the same benchmark problem in linear elasticity on 4096 congruent cells. It can be seen, that the speedup of the local assembly is much higher than of the solver itself, since considerably less communication between processes is needed. Note, that the assemble time already includes the final assembly of the global system, which requires some communication.

Algorithm 1 Weakly conforming method for linear elasticity

```

1: Input:  $\mathcal{K}_h, \mathbf{t}_N, \mathbf{f}$ 
2:  $\hat{\mathbf{u}}_h^{wc} = \mathbf{0}, \hat{A}_h = 0, \hat{\ell}_h = \mathbf{0}$ 
3: Compute  $\hat{\mathbf{u}}_h^{wc}$  from  $\mathbf{u}_D$ 
4: for  $K \in \mathcal{K}_h$  do
5:    $n_{\text{test},K} =$  number of test functions in cell  $K$ 
6:   for ( $i = 0; i < n_{\text{test},K}; i++$ ) do
7:     for ( $j = 0; j < n_{\text{test},K}; j++$ ) do
8:        $(A_K)_{ij} = \int_K \mathbb{C}\boldsymbol{\varepsilon}(\mathbf{D}\mathbf{v}_i) : \mathbf{D}\mathbf{v}_j \, d\mathbf{x}$ 
9:     end for
10:     $(\ell_K)_i = - \int_K \mathbf{f}\mathbf{v}_i \, d\mathbf{x}$ 
11:     $n_{\text{faces}} =$  number of faces of cell  $K$ 
12:     $n_j = 0$ 
13:    for ( $f = 0; f < n_{\text{faces}}; f++$ ) do
14:       $n_{\text{Lagr},f} =$  number of Lagrange parameters on face  $f$ 
15:      for ( $j = 0; j < n_{\text{Lagr},f}; j++$ ) do
16:         $(B_K)_{in_j} = \int_{F_f} \boldsymbol{\sigma}(\mathbf{v}_i)\mathbf{n}\boldsymbol{\mu}_{F,j} \, d\mathbf{a}$ 
17:         $n_j = n_j + 1$ 
18:      end for
19:      for ( $j = 0; j < n_{\text{test},K}; j++$ ) do
20:         $(\ell_K)_j = \int_{F_f} \mathbf{t}_N\mathbf{v}_j \, d\mathbf{a}$ 
21:      end for
22:    end for
23:  end for
24:   $\hat{A}_h = \hat{A}_h + \begin{pmatrix} 0 \\ \hat{B}'_K \end{pmatrix}^\top \begin{pmatrix} A_K & B'_K \\ B_K & 0 \end{pmatrix}^{-1} \begin{pmatrix} 0 \\ \hat{B}_K \end{pmatrix},$ 
25:   $\hat{\ell}_h = \hat{\ell}_h + \begin{pmatrix} 0 \\ \hat{B}'_K \end{pmatrix}^\top \begin{pmatrix} A_K & B'_K \\ B_K & 0 \end{pmatrix}^{-1} \begin{pmatrix} \ell_K \\ 0 \end{pmatrix}.$ 
26:  compute  $\hat{\mathbf{u}}_h^{wc}$  with  $\hat{A}_h\hat{\mathbf{u}}_h^{wc} = \hat{\ell}_h$ 
27: end for
28: Output:  $\hat{\mathbf{u}}_h^{wc}$ 

```

Chapter 4

Numerical properties of the weakly conforming finite element method

In this chapter we look at various properties of the new discretization. There are a lot of important challenges and tasks, that a method needs to fulfill, so that it can be a sensible choice of discretization for a problem based in solid mechanics. For example, there may be singularities, arising either from geometrical circumstances or material transitions; in other cases the material can be incompressible. Furthermore we are interested in the convergence properties of a method, for various choices of ansatz spaces and for various materials. The example of the locking beam in Section 4.3 was already published in [17]; the other examples of the chapter will be submitted with our SPP partners for a book chapter [15] within the final report of our SPP 1748.

In our first two numerical tests with known solution, the approximation error is compared with the interpolation error. We use

- the nodal interpolation $\Pi_h^{\text{cf}}: C^0(\Omega; \mathbb{R}^{\text{dim}}) \longrightarrow V_h^{\text{cf}}$ for conforming elements,
- the L_2 projection $\Pi_h^0: L_2(\Omega; \mathbb{R}^{\text{dim}}) \longrightarrow V_h^{\text{dG}}$ for discontinuous Galerkin elements,
- the interpolation $\Pi_h^{\text{wc}}: H^1(\Omega; \mathbb{R}^{\text{dim}}) \longrightarrow V_h^{\text{wc}}$ defined by the L_2 projec-

tion onto the multiplier space M_h and the local reconstruction in V_h^{wc} , cf. (3.19).

Convergence rates

To quantify the development of the errors of the computed methods, we define the convergence rate κ as

$$e(N) = N^{-\frac{\kappa}{\dim}} C,$$

where C is assumed to be independent of N asymptotically for $N \rightarrow \infty$ and N is the number of cells, while $e(\cdot)$ is the chosen error measure. For uniform mesh refinement, this is equivalent to the widespread definition

$$e(h) = h^\kappa C,$$

asymptotically for $h \rightarrow 0$, with a different constant C . The optimal convergence rates for p -methods can be found in [10]. They are given by

$$\kappa_{L_2} = p + 1, \quad \kappa_E = p, \quad (4.1)$$

for the L_2 error and for the energy error respectively, where p is the order of the chosen method.

Since we do not compute the convergence rates analytically, but rather deduce them from observing results of computations, we state the experimental order of convergence (EOC), with $\text{EOC} \sim \kappa$. When we compute various mesh levels of an example, we often state the ratio of errors between cell levels

$$R_l = \frac{e_l}{e_{l-1}} = \left(\frac{N_l}{N_{l-1}} \right)^{\frac{\text{EOC}}{\dim}},$$

where $l, l-1$ are mesh levels, e_l, e_{l-1} their corresponding errors and from which we can compute the EOC.

4.1 Convergence rates in a smooth setting

We evaluate the quality and efficiency of the weakly conforming method for a smooth problem and compare it to our benchmark methods. The domain is chosen to be $\Omega = (0, 10)^2 \setminus [2, 8]^2$ and we use a linear material with the

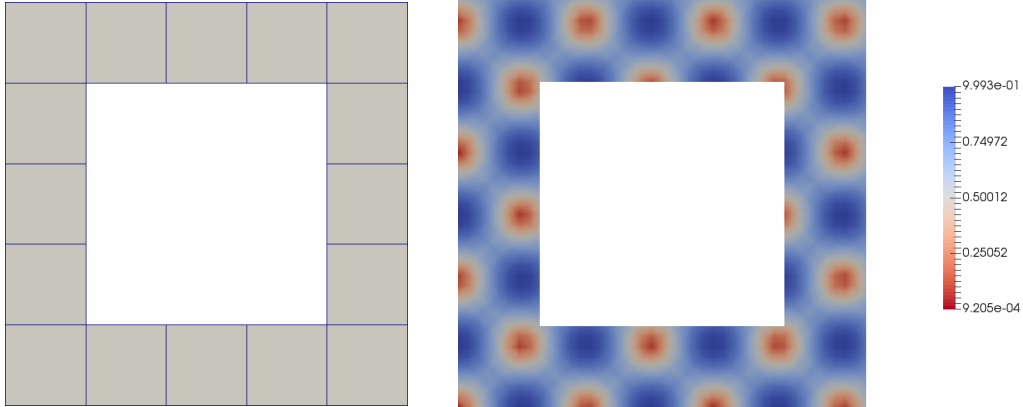


Figure 4.1: Sinus example: Initial mesh with 16 quadrilaterals (left) and deformation \mathbf{u} (right) for $\Omega = (0, 10)^2 \setminus [2, 8]^2$.

parameters $E = 2.5 \text{ MPa}$, $\nu = 0.25$. The Dirichlet boundary conditions on $\Gamma_D = \partial\Omega$ obtained are obtained from the solution \mathbf{u} , which is given by

$$\mathbf{u} \begin{pmatrix} x \\ y \end{pmatrix} = \begin{pmatrix} \sin(x) \cos(y) \\ \cos(x) \sin(y) \end{pmatrix}. \quad (4.2)$$

For the numerical test we use quadrilateral meshes, starting with the mesh depicted in Fig. 4.1, with mesh size $h_l = 2^{1-l}$, where $l \geq 0$ is the number of refinement steps. Since this is an example with a smooth solution, we expect on a sequence of uniformly refined meshes for discretizations of degree k the asymptotic convergence rate 2^{k+1} in the L_2 norm and 2^k in the energy norm.

The convergence is tested in Tab. 4.1 for conforming approximations in V_h^{cf} , in Tab. 4.2 for discontinuous Galerkin approximations in V_h^{dG} , and in Tab. 4.3 for the new weakly conforming finite element space V_h^{wc} . In Fig. 4.2 the results are illustrated in convergence graphs for a quick overview. We observe that

- In the lowest order case, the conforming method is more efficient than the discontinuous Galerkin method. This behavior shows that such a smooth example is being already sufficiently well discretized by conforming methods and there is no need for the additional computational effort which is introduced by discontinuous methods. However, this observation holds only true for sufficiently smooth examples, as we show in further examples. The experimental order of convergence is equal to the optimal convergence rate for methods, cf. equation (4.1).

There is no truly linear weakly conforming method, the lowest stable

cells	1024	4096	16384	65536	262144
$\dim V_{h,1}^{\text{cf}}$	2 304	8 704	33 792	133 120	528 384
$\ \mathbf{u} - \mathbf{u}_{h,1}^{\text{cf}}\ _{0,\Omega}$	0.03713	0.00927	0.00232	5.787e-04	1.447e-04
R_l	4.01	4.00	4.00	4.00	4.00
$\ \mathbf{u} - \Pi_h^{\text{cf}} \mathbf{u}\ _{0,\Omega}$	0.05858	0.01470	0.00368	9.195e-04	2.299e-04
R_l	3.99	4.00	4.00	4.00	4.00
$ \mathbf{u} - \mathbf{u}_{h,1}^{\text{cf}} _{\mathbb{E},\Omega_h}$	0.25805	0.12896	0.06447	0.03224	0.01612
R_l	2.00	2.00	2.00	2.00	2.00
$ \mathbf{u} - \Pi_h^{\text{cf}} \mathbf{u} _{\mathbb{E},\Omega_h}$	0.25922	0.12911	0.06449	0.03224	0.01612
R_l	2.01	2.00	2.00	2.00	2.00
$\dim V_{h,2}^{\text{cf}}$	6 656	25 600	100 352	397 312	1 581 056
$\ \mathbf{u} - \mathbf{u}_{h,1}^{\text{cf}}\ _{0,\Omega}$	6.049e-04	7.536e-05	9.411e-06	1.176e-06	1.470e-07
R_l	8.03	8.01	8.00	8.00	8.00
$\ \mathbf{u} - \Pi_h^{\text{cf}} \mathbf{u}\ _{0,\Omega}$	6.275e-04	7.607e-05	9.434e-06	1.177e-06	1.470e-07
R_l	8.25	8.06	8.02	8.00	8.00
$ \mathbf{u} - \mathbf{u}_{h,2}^{\text{wc}} _{\mathbb{E},\Omega_h}$	0.00857	0.00214	5.342e-04	1.335e-04	3.338e-05
R_l	4.01	4.00	4.00	4.00	4.00
$ \mathbf{u} - \Pi_h^{\text{cf}} \mathbf{u} _{\mathbb{E},\Omega_h}$	0.00870	0.00215	5.348e-04	1.336e-04	3.339e-05
R_l	4.06	4.01	4.00	4.00	4.00

Table 4.1: Sinus example: Interpolation and approximation error for the energy and the L_2 norm for the linear and quadratic conforming Galerkin method. $\text{EOC}_{L_2} \sim p + 1$ and $\text{EOC}_{\mathbb{E}} \sim p$ for both variations.

cells	1024	4096	16384	65536	262144
$\dim V_{h,1}^{\text{dG}}$	8 192	32 768	131 072	524 288	2 097 152
$\ \mathbf{u} - \mathbf{u}_{h,1}^{\text{dG}}\ _{0,\Omega}$	0.03490	0.00810	0.00194	4.759e-04	1.177e-04
R_l	4.31	4.18	4.09	4.04	
$\ \mathbf{u} - \Pi_h^0 \mathbf{u}\ _{0,\Omega}$	0.01859	0.00465	0.00116	2.908e-04	7.270e-05
R_l	4.00	4.00	4.00	4.00	
$ \mathbf{u} - \mathbf{u}_{h,1}^{\text{dG}} _{\mathbb{E},\Omega_h}$	0.28438	0.13596	0.06627	0.03269	0.01623
R_l	2.09	2.05	2.03	2.01	
$ \mathbf{u} - \Pi_h^0 \mathbf{u} _{\mathbb{E},\Omega_h}$	0.25811	0.12897	0.06448	0.03224	0.01612
R_l	2.00	2.00	2.00	2.00	
$\dim V_{h,2}^{\text{dG}}$	18 432	73 728	294 912	1 179 648	4 718 592
$\ \mathbf{u} - \mathbf{u}_{h,2}^{\text{dG}}\ _{0,\Omega}$	5.545e-04	6.948e-05	8.700e-06	1.089e-06	1.383e-07
R_l	7.98	7.99	7.99	7.87	
$\ \mathbf{u} - \Pi_h^0 \mathbf{u}\ _{0,\Omega}$	3.939e-04	4.926e-05	6.159e-06	7.699e-07	9.624e-08
R_l	8.00	8.00	8.00	8.00	
$ \mathbf{u} - \mathbf{u}_{h,2}^{\text{dG}} _{\mathbb{E},\Omega_h}$	0.00900	0.00223	5.555e-04	1.386e-04	3.461e-05
R_l	4.03	4.02	4.01	4.00	
$ \mathbf{u} - \Pi_h^0 \mathbf{u} _{\mathbb{E},\Omega_h}$	0.00972	0.00243	6.079e-04	1.520e-04	3.799e-05
R_l	4.00	4.00	4.00	4.00	
$\dim V_{h,3}^{\text{dG}}$	32 768	131 072	524 288	2 097 152	8 388 608
$\ \mathbf{u} - \mathbf{u}_{h,3}^{\text{dG}}\ _{0,\Omega}$	8.009e-06	5.103e-07	3.218e-08	2.020e-09	1.692e-10
R_l	15.70	15.86	15.93	11.94	
$ \mathbf{u} - \mathbf{u}_{h,3}^{\text{dG}} _{\mathbb{E},\Omega_h}$	1.785e-04	2.215e-05	2.759e-06	3.442e-07	4.297e-08
R_l	8.06	8.03	8.02	8.01	
$ \mathbf{u} - \Pi_h^0 \mathbf{u} _{\mathbb{E},\Omega_h}$	2.101e-04	2.627e-05	3.284e-06	4.105e-07	5.132e-08
R_l	8.00	8.00	8.00	8.00	

Table 4.2: Sinus example: Interpolation and approximation error for the energy and the L_2 norm for the linear, quadratic and cubic discontinuous Galerkin method. $\text{EOC}_{L_2} \sim p + 1$ and $\text{EOC}_E \sim p$ for all three variations.

cells	1024	4096	16384	65536	262144
dim $M_{h,1}^{\text{wc}}$	6 528	25 344	99 840	396 288	1 579 008
$\ \mathbf{u} - \mathbf{u}_{h,1}^{\text{wc}}\ _{0,\Omega}$	0.00124	1.553e-04	1.943e-05	2.429e-06	3.036e-07
R_l	8.26	8.09	8.03	8.01	
$\ \mathbf{u} - \Pi_h^{\text{wc}}\mathbf{u}\ _{0,\Omega}$	0.00124	1.553e-04	1.943e-05	2.429e-06	3.036e-07
R_l	7.98	8.00	8.00	8.00	
$ \mathbf{u} - \mathbf{u}_{h,1}^{\text{wc}} _{E,\Omega_h}$	0.02020	0.00504	0.00126	3.151e-04	7.879e-05
R_l	4.01	4.00	4.00	4.00	4.00
$ \mathbf{u} - \Pi_h^{\text{wc}}\mathbf{u} _{E,\Omega_h}$	0.01942	0.00486	0.00122	3.043e-04	7.607e-05
R_l	3.99	4.00	4.00	4.00	4.00
dim $M_{h,2}^{\text{wc}}$	8 704	33 792	133 120	528 384	2 105 344
$\ \mathbf{u} - \mathbf{u}_{h,2}^{\text{wc}}\ _{0,\Omega}$	3.503e-04	4.353e-05	5.430e-06	6.782e-07	8.474e-08
R_l	8.05	8.02	8.01	8.00	
$\ \mathbf{u} - \Pi_h^{\text{wc}}\mathbf{u}\ _{0,\Omega}$	1.755e-04	2.008e-05	2.448e-06	3.040e-07	3.793e-08
R_l	8.74	8.20	8.05	8.01	
$ \mathbf{u} - \mathbf{u}_{h,2}^{\text{wc}} _{E,\Omega_h}$	0.00618	0.00155	3.891e-04	9.741e-05	2.437e-05
R_l	3.98	3.99	3.99	4.00	
$ \mathbf{u} - \Pi_h^{\text{wc}}\mathbf{u} _{E,\Omega_h}$	0.00431	0.00106	2.637e-04	6.586e-05	1.646e-05
R_l	4.06	4	.02	4.00	4.00
dim $M_{h,2}^{\text{wc}}$	13 056	50 688	199 680	792 576	3 158 016
$\ \mathbf{u} - \mathbf{u}_{h,2}^{\text{wc}}\ _{0,\Omega}$	8.438e-06	5.333e-07	3.345e-08	2.093e-09	1.435e-10
R_l	15.82	15.94	15.98	16.00	
$\ \mathbf{u} - \Pi_h^{\text{wc}}\mathbf{u}\ _{0,\Omega}$	7.393e-06	4.645e-07	2.907e-08	1.818e-09	1.136e-10
R_l	15.91	15.98	15.99	16.00	
$ \mathbf{u} - \mathbf{u}_{h,2}^{\text{wc}} _{E,\Omega_h}$	1.454e-04	1.829e-05	2.290e-06	2.864e-07	3.581e-08
R_l	7.95	7.99	8.00	8.00	
$ \mathbf{u} - \Pi_h^{\text{wc}}\mathbf{u} _{E,\Omega_h}$	1.393e-04	1.749e-05	2.189e-06	2.737e-07	3.421e-08
R_l	7.97	7.99	8.00	8.00	

Table 4.3: Sinus example: Interpolation and approximation error for the energy and the L_2 norm for the weakly conforming $\mathbb{P}_2\mathbb{P}_{0+}$, $\mathbb{P}_3\mathbb{P}_1$, and $\mathbb{P}_4\mathbb{P}_2$ discretizations. $\text{EOC}_{L_2} \sim 3$ and $\text{EOC}_E \sim 2$ for the two lower order methods and $\text{EOC}_{L_2} \sim 4$ and $\text{EOC}_E \sim 3$ for the $\mathbb{P}_4\mathbb{P}_2$ variant.

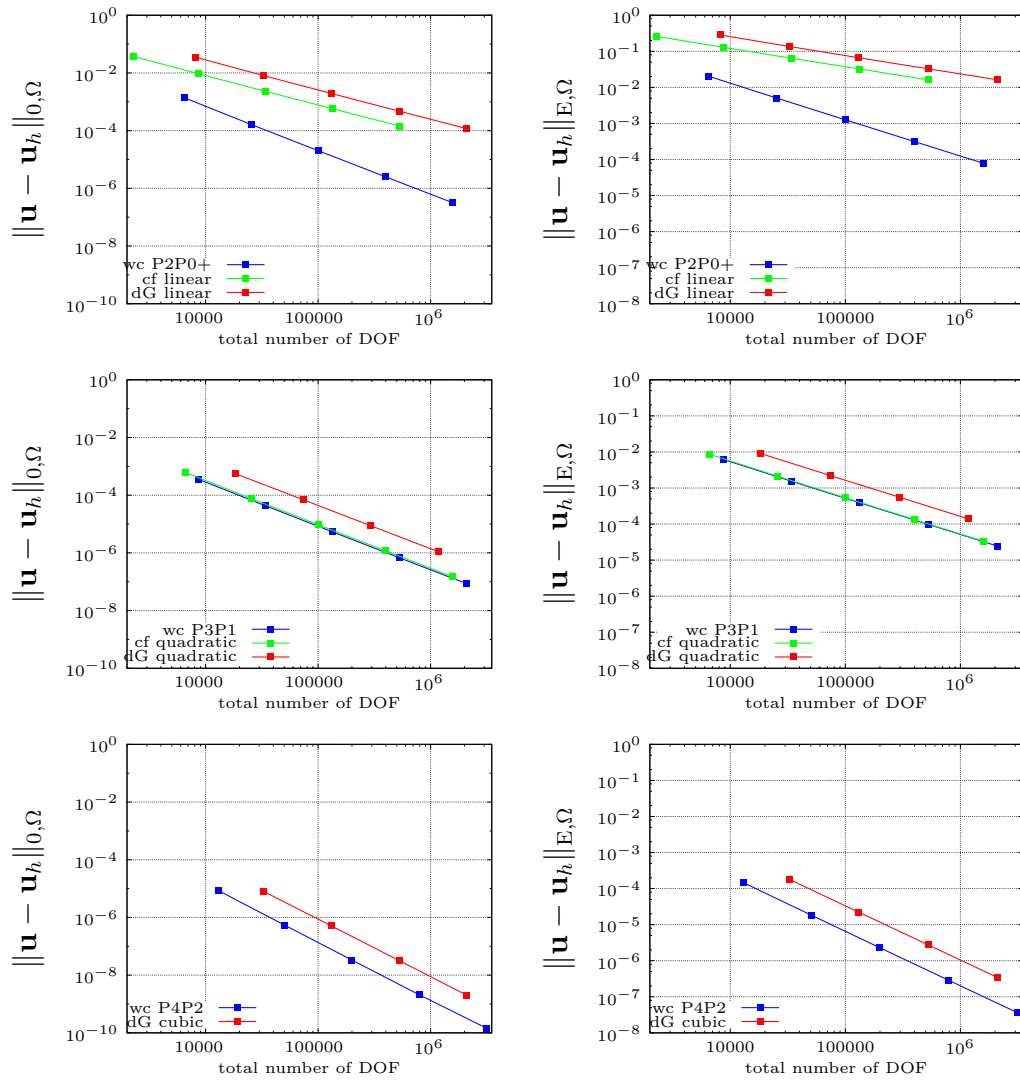


Figure 4.2: Sinus example: Convergence study in the L_2 -norm and the energy norm of the smooth example for all linear (top row), quadratic (middle row) and cubic (bottom row) schemes.

order uses a quadratic ansatz space in the local cells, which explains the high efficiency compared to the linear methods and it explains, why the EOC is equivalent to the optimal rate for quadratic methods.

- When we compare the quadratic methods with the $\mathbb{P}_3\mathbb{P}_1$ ansatz of the weakly conforming method, we see that the relation between the conforming and nonconforming methods are very similar, where again the increased global size of the nonconforming dG method cannot translate into additional accuracy. The weakly conforming method can compete with the conforming method, the reduction of global degrees of freedom increases its efficiency enough to be on the level of a conforming method. Additionally all three quadratic methods achieve the optimal EOC.
- The cubic dG scheme and the $\mathbb{P}_4\mathbb{P}_2$ wc method show again a comparable behavior. On the same mesh refinement level the errors are nearly the same, but the dG method has a much larger global system, which leads to a worse efficiency. Again, both methods yield the optimal convergence rate.

4.2 Geometrical singularities

As a next step, we increase the difficulty, by considering a well known benchmark problem [27, Sect. 3.4] with a singularity in the L-shaped domain $\Omega = (-1, 1)^2 \setminus [0, -1] \times [-1, 0]$.

The solution

$$\mathbf{u} \begin{pmatrix} r \cos(\varphi - \pi/6) \\ r \sin \varphi - \pi/6 \end{pmatrix} = \begin{pmatrix} \cos(\varphi)u_1(r, \varphi) - \sin(\varphi)u_2(r, \varphi) \\ \sin(\varphi)u_1(r, \varphi) + \cos(\varphi)u_2(r, \varphi) \end{pmatrix}, \quad |\varphi| < \pi/3 \quad (4.3)$$

is given explicitly in radial coordinates by the radial and angular displacements

$$u_1(r, \varphi) = \frac{r^\alpha}{2\mu} \left(-(\alpha + 1) \cos((\alpha + 1)\varphi) + (C_2 - \alpha - 1)C_1 \cos((\alpha - 1)\varphi) \right),$$

$$u_2(r, \varphi) = \frac{r^\alpha}{2\mu} \left((\alpha + 1) \sin((\alpha + 1)\varphi) + (C_2 + \alpha - 1)C_1 \sin((\alpha - 1)\varphi) \right)$$

with $C_1 = -\cos((\alpha + 1)\omega) / \cos((\alpha - 1)\omega)$, $C_2 = 2(\lambda + 2\mu) / (\lambda + \mu)$, $\omega = 3\pi/4$, where $\alpha \approx 0.54448373678$ is the positive solution of $\alpha \sin(2\omega) + \sin(2\omega\alpha) = 0$.

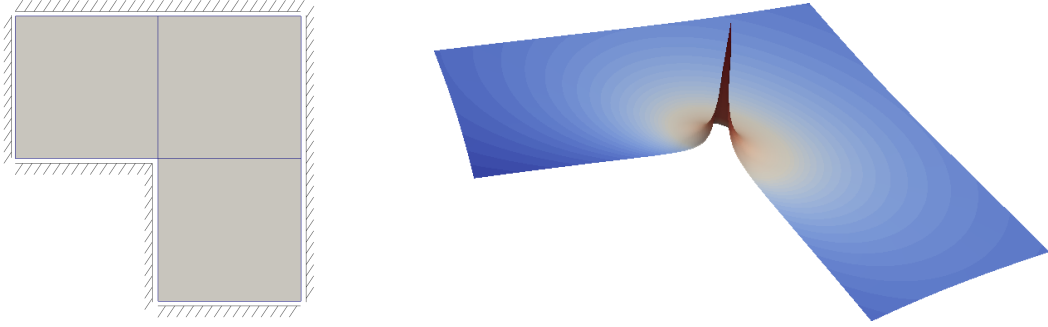


Figure 4.3: L-shaped example: Initial mesh with 3 quadrilaterals and Dirichlet boundary conditions (left), distribution of $|\boldsymbol{\sigma}(\mathbf{u})|$ with strong corner singularity (right).

Then, $\operatorname{div} \boldsymbol{\sigma}(\mathbf{u}) = \mathbf{0}$. For our tests, we use the Lamé parameters $\lambda = 1$ and $\mu = 1$ and Dirichlet boundary conditions on $\Gamma_D = \partial\Omega$ obtained from the solution (4.3).

In case of conforming approximations the error in the energy norm is minimized by the finite element solution, but in general, we only expect that L_2 and energy error are converging with the same rate. This is now tested for uniform and graded meshes as well as for an adaptive scheme.

Uniform meshes

In the first test on *uniformly refined meshes*, we use quadrilateral meshes with mesh size $h_l = 2^{-l}$, where $l \geq 0$ is the number of refinement steps, cf. Fig. 4.2. Due to the singularity we expect on a sequence of uniformly refined meshes the asymptotic convergence rate $\kappa_{L_2} = \frac{3}{2}$ which corresponds to $R_l = 2\sqrt{2}$ in the L_2 norm and $\kappa_E = \frac{1}{2}$ which corresponds to $R_l = \sqrt{2}$ in the energy norm. We observe in Tab. 4.4 that

- compared to the conform methods, the dG method yields better results on the same mesh but with far more degrees of freedom. Nevertheless, the same accuracy level is achieved with less degrees of freedom, hence the discontinuous method is more efficient than its continuous counterpart;
- the weakly conforming method performs similar to the dG method, but the hybridization allows to reduce the global number of degrees of freedom substantially. Thus, in this example the hybrid weakly conforming

cells	48	192	768	3 072	12 288
$\dim V_{h,1}^{\text{cf}}$	130	450	1 666	6 402	25 090
$\ \mathbf{u} - \mathbf{u}_{h,1}^{\text{cf}}\ _{0,\Omega}$	0.00468	0.00197	0.00082	0.00034	0.00014
R_l	2.37	2.40	2.41	2.41	
$\ \mathbf{u} - \Pi_h^{\text{cf}} \mathbf{u}\ _{0,\Omega}$	0.00342	0.00120	0.00041	0.00014	0.00005
R_l	2.86	2.89	2.90	2.91	
$ \mathbf{u} - \mathbf{u}_{h,1}^{\text{cf}} _{\mathbb{E},\Omega_h}$	0.07256	0.05027	0.03471	0.02390	0.01642
R_l	1.44	1.45	1.45	1.46	
$ \mathbf{u} - \Pi_h^{\text{cf}} \mathbf{u} _{\mathbb{E},\Omega_h}$	0.08077	0.05615	0.03878	0.02669	0.01833
R_l	1.44	1.45	1.45	1.46	
$\dim V_{h,2}^{\text{cf}}$	354	1 282	4 866	18 946	74 754
$\ \mathbf{u} - \mathbf{u}_{h,2}^{\text{cf}}\ _{0,\Omega}$	0.00173	0.00066	0.00025	0.00010	0.00004
R_l	2.63	2.59	2.56	2.53	
$\ \mathbf{u} - \Pi_h^{\text{cf}} \mathbf{u}\ _{0,\Omega}$	0.00221	0.00076	0.00026	0.00009	0.00003
R_l	2.92	2.92	2.92	2.92	
$ \mathbf{u} - \mathbf{u}_{h,2}^{\text{cf}} _{\mathbb{E},\Omega_h}$	0.05357	0.03671	0.02517	0.01725	0.01183
R_l	1.46	1.46	1.46	1.46	
$ \mathbf{u} - \Pi_h^{\text{cf}} \mathbf{u} _{\mathbb{E},\Omega_h}$	0.07307	0.05010	0.03435	0.02355	0.01615
R_l	1.46	1.46	1.46	1.46	
$\dim V_{h,1}^{\text{dG}}$	384	1 536	6 144	24 576	98 304
$\ \mathbf{u} - \mathbf{u}_{h,1}^{\text{dG}}\ _{0,\Omega}$	0.00233	0.00083	0.00030	0.00011	0.00004
R_l	2.79	2.76	2.73	2.70	
$\ \mathbf{u} - \Pi_{h,1}^0 \mathbf{u}\ _{0,\Omega}$	0.07061	0.04919	0.00020	0.00007	0.00002
R_l	2.84	2.88	2.90	2.91	
$ \mathbf{u} - \mathbf{u}_{h,1}^{\text{dG}} _{\mathbb{E},\Omega_h}$	0.07061	0.04919	0.03403	0.02344	0.01611
R_l	1.44	1.45	1.45	1.46	
$ \mathbf{u} - \Pi_{h,1}^0 \mathbf{u} _{\mathbb{E},\Omega_h}$	0.06606	0.04622	0.03203	0.02208	0.01519
R_l	1.43	1.44	1.45	1.45	
$\dim V_{h,2}^{\text{dG}}$	864	3 456	13 824	55 296	221 184
$\ \mathbf{u} - \mathbf{u}_{h,2}^{\text{dG}}\ _{0,\Omega}$	0.00058	0.00020	0.00007	0.00003	0.00001
R_l	2.84	2.82	2.79	2.75	
$\ \mathbf{u} - \Pi_{h,2}^0 \mathbf{u}\ _{0,\Omega}$	0.00039	0.00014	0.00005	0.00002	5.440e-06
R_l	2.92	2.92	2.92	2.92	
$ \mathbf{u} - \mathbf{u}_{h,2}^{\text{dG}} _{\mathbb{E},\Omega_h}$	0.03250	0.02228	0.01528	0.01048	0.01006
R_l	1.46	1.46	1.46	1.46	
$ \mathbf{u} - \Pi_{h,2}^0 \mathbf{u} _{\mathbb{E},\Omega_h}$	0.03066	0.02103	0.01442	0.00989	0.00678
R_l	1.46	1.46	1.46	1.46	
$\dim M_{h,1}^{\text{wc}}$	336	1 248	4 800	18 816	74 496
$\ \mathbf{u} - \mathbf{u}_{h,1}^{\text{wc}}\ _{0,\Omega}$	0.00147	0.00051	0.00018	0.00006	0.00002
R_l	2.88	2.88	2.87	2.85	
$\ \mathbf{u} - \Pi_h^{\text{wc}} \mathbf{u}\ _{0,\Omega}$	0.00105	0.00036	0.00012	0.00004	0.00001
R_l	2.92	2.92	2.92	2.92	
$ \mathbf{u} - \mathbf{u}_{h,1}^{\text{wc}} _{\mathbb{E},\Omega_h}$	0.04579	0.03140	0.02153	0.01476	0.01012
R_l	1.46	1.46	1.46	1.46	
$ \mathbf{u} - \Pi_h^{\text{wc}} \mathbf{u} _{\mathbb{E},\Omega_h}$	0.04472	0.03067	0.02103	0.01442	0.00989
R_l	1.46	1.46	1.46	1.46	
$\dim M_{h,2}^{\text{wc}}$	448	1 664	6 400	25 088	99 328
$\ \mathbf{u} - \mathbf{u}_{h,2}^{\text{wc}}\ _{0,\Omega}$	0.00080	0.00028	0.00010	0.00004	0.00001
R_l	2.83	2.80	2.75	2.69	
$\ \mathbf{u} - \Pi_h^{\text{wc}} \mathbf{u}\ _{0,\Omega}$	0.00061	0.00020	0.00007	0.00002	8.364e-06
R_l	2.92	2.92	2.92	2.92	
$ \mathbf{u} - \mathbf{u}_{h,2}^{\text{wc}} _{\mathbb{E},\Omega_h}$	0.03527	0.02419	0.01659	0.01137	0.00780
R_l	1.46	1.46	1.46	1.46	
$ \mathbf{u} - \Pi_h^{\text{wc}} \mathbf{u} _{\mathbb{E},\Omega_h}$	0.03332	0.02284	0.01566	0.01074	0.00736
R_l	1.46	1.46	1.46	1.46	

Table 4.4: L-shaped example: Energy and L_2 interpolation and approximation error for the bilinear and biquadratic discretizations $V_{h,k}^{\text{cf}}$, $V_{h,k}^{\text{dG}}$, $V_{h,k}^{\text{wc}}$, $k = 1, 2$, on uniform quadrilateral meshes.

method is clearly more efficient.

- all methods yield the reduced optimal convergence rates κ in both error measures.

Graded meshes

As we could see, the convergence rates are capped for all methods on uniform meshes for this example. On *graded meshes* this can be improved, cf. [7]. To construct a series of graded meshes we start with a mesh of two quadrilaterals. Then, in every refinement step, we refine each cell K by selecting on every face $F \in \mathcal{F}_K$ a point $x_r \in \overline{F} = \text{conv}\{x_a, x_b\}$ such that $|x_r - x_a| = |x_b - x_a|^{\frac{1}{\gamma}}$.

For the graduation γ we test two cases. We start with $\gamma = \alpha$. Based on [6] we know, that this choice ensures that linear schemes converge optimally with respect to the L_2 norm as α is the parameter of the singularity. Two examples of the resulting graded meshes can be seen in Fig. 4.4. We observe in our computations, cf. Tab. 4.5, that

- the rate of convergence has increased due to the better resolution of the singularity for all methods, especially for all higher order schemes. For all methods $\text{EOC}_E \approx 1$. For the linear conforming method $\text{EOC}_{L_2} \approx 2$, while the quadratic conforming method and both weakly conforming method achieve $\text{EOC}_{L_2} \approx 2.5$;
- the conforming method is again less accurate than the non-conforming methods. But this time the efficiency is comparable to the DG method since the conforming method uses far less degrees of freedom and the same accuracy level requires about the same computational effort;
- the weakly conforming method is again more efficient than the discontinuous Galerkin method, due to the reduction of global degrees of freedom by static condensation.

On a hierarchy of graded mesh the penalty parameter θ in the dG method cannot be chosen uniformly so that the method is slightly different on subsequent levels. Therefore, we only compare the conforming and weakly conforming methods.

cells	32	128	512	2048	8192
$\dim V_{h,1}^{cf}$	90	306	1122	4290	16770
$\ \mathbf{u} - \mathbf{u}_{h,1}^{cf}\ _{0,\Omega}$	0.00241	0.00064	0.00017	0.00004	1.157e-05
R_l	3.77	3.78	3.81	3.84	
$\ \mathbf{u} - \Pi_h^{cf} \mathbf{u}\ _{0,\Omega}$	0.00303	0.00083	0.00022	0.00005	1.379e-05
R_l	3.67	3.84	3.93	3.97	
$ \mathbf{u} - \mathbf{u}_{h,1}^{cf} _{E,\Omega_h}$	0.07660	0.04517	0.02584	0.01446	0.00797
R_l	1.70	1.75	1.79	1.81	
$ \mathbf{u} - \Pi_h^{cf} \mathbf{u} _{E,\Omega_h}$	0.07902	0.04636	0.02637	0.01469	0.00807
R_l	1.70	1.76	1.79	1.82	
$\dim V_{h,2}^{cf}$	242	866	3266	12674	49922
$\ \mathbf{u} - \mathbf{u}_{h,2}^{cf}\ _{0,\Omega}$	0.00123	0.00022	0.00004	7.382e-06	1.400e-06
R_l	5.66	5.50	5.37	5.27	
$\ \mathbf{u} - \Pi_h^{cf} \mathbf{u}\ _{0,\Omega}$	0.00091	0.00014	0.00002	2.996e-06	4.361e-07
R_l	6.62	6.75	6.80	6.87	
$ \mathbf{u} - \mathbf{u}_{h,2}^{cf} _{E,\Omega_h}$	0.05744	0.02966	0.01506	0.00761	0.00384
R_l	1.94	1.97	1.98	1.98	
$ \mathbf{u} - \Pi_h^{cf} \mathbf{u} _{E,\Omega_h}$	0.06727	0.03450	0.01747	0.00883	0.00446
R_l	1.95	1.97	1.98	1.98	
$\dim M_{h,1}^{wc}$	228	840	3216	12576	49728
$\ \mathbf{u} - \mathbf{u}_{h,1}^{wc}\ _{0,\Omega}$	0.00087	0.00014	0.00002	3.641e-06	5.823e-07
R_l	6.31	6.10	6.21	6.25	
$\ \mathbf{u} - \Pi_h^{wc} \mathbf{u}\ _{0,\Omega}$	0.00062	0.00010	0.00002	2.519e-06	3.839e-07
R_l	6.14	6.25	6.40	6.56	
$ \mathbf{u} - \mathbf{u}_{h,1}^{wc} _{E,\Omega_h}$	0.03905	0.02008	0.01026	0.00519	0.00261
R_l	1.94	1.96	1.98	1.99	
$ \mathbf{u} - \Pi_h^{wc} \mathbf{u} _{E,\Omega_h}$	0.04128	0.02142	0.01092	0.00550	0.00276
R_l	1.93	1.96	1.99	2.00	
$\dim M_{h,2}^{wc}$	304	1120	4288	16768	66304
$\ \mathbf{u} - \mathbf{u}_{h,2}^{wc}\ _{0,\Omega}$	0.00045	0.00007	0.00001	2.104e-06	3.505e-07
R_l	6.05	5.89	5.95	6.00	
$\ \mathbf{u} - \Pi_h^{wc} \mathbf{u}\ _{0,\Omega}$	0.00027	0.00004	6.323e-06	9.477e-07	1.396e-07
R_l	6.47	6.54	6.67	6.79	
$ \mathbf{u} - \mathbf{u}_{h,2}^{wc} _{E,\Omega_h}$	0.02784	0.01417	0.00717	0.00361	0.00181
R_l	1.97	1.98	1.99	1.99	
$ \mathbf{u} - \Pi_h^{wc} \mathbf{u} _{E,\Omega_h}$	0.02638	0.01339	0.00674	0.00338	0.00169
R_l	1.97	1.99	2.00	2.00	

Table 4.5: L-shaped example: Energy and L_2 interpolation and approximation error for the bilinear and biquadratic discretizations on graded quadrilateral meshes corresponding to the singularity r^α .

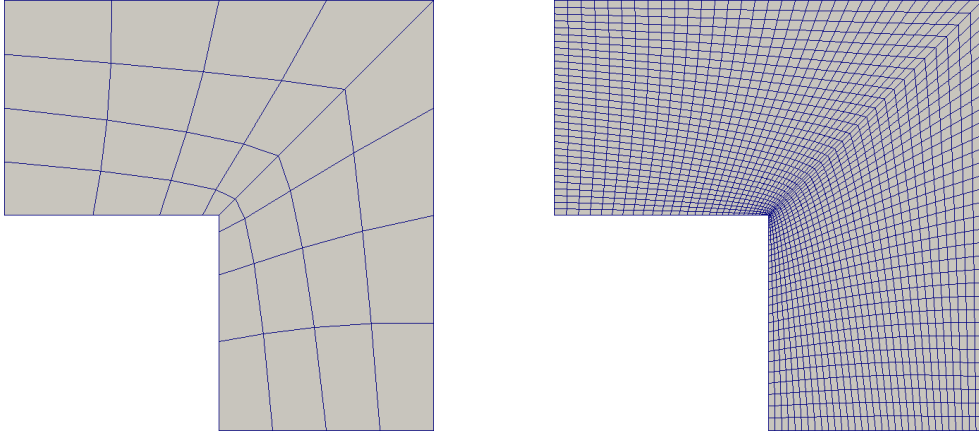


Figure 4.4: L-shaped example: Exemplary graded meshes of level 2 (left) and 5 (right), $\gamma = \alpha$.

Next we select $\gamma = \alpha^{\frac{3}{2}}$ to improve the rate of convergence. We observe, cf. Tab. 4.6, that

- the rate of convergence increases for all schemes only slightly with respect to the energy error, however, for the quadratic conforming method and both weakly conforming variants the experimental order of convergence for the L_2 error increases to $\text{EOC}_{L_2} \approx 3$;
- however, the graduation reduces the mesh regularity: the diameter ratios of the graduated cells are given by $\frac{h_x}{h_y} = (2^l - 1)^{\frac{1}{\gamma}}$ for the mesh on level l . Thus, the degeneration increases for smaller γ . E.g., for $\gamma = \alpha^{\frac{3}{2}}$ the ratio on mesh level $l = 6$ is $\frac{h_x}{h_y} \approx 34200$, so that we cannot refine these meshes beyond a certain point;
- the two weakly conforming approaches differ only in the error constant, the observed convergence order is the same for both, which is again due to the fact, that they are both of the same order.

Both examples showed, that the weakly conforming method is capable of solving basic problems in solid mechanics. The convergence rates were the ones we expected and because of the static condensation, the overall efficiency surpassed that of its non-hybrid competitors in most cases.

To further improve the efficiency of the weakly conforming method we considered adaptive refinement strategies for the weakly conforming method for the L-shape example. The results are depicted in Chapter 5.

cells	32	128	512	2 048	8 192
$\dim V_{h,1}^{\text{cf}}$	90	306	1 122	4 290	16 770
$\ \mathbf{u} - \mathbf{u}_{h,1}^{\text{cf}}\ _{0,\Omega}$	0.00253	0.00062	0.00016	0.00004	9.750e-06
R_l	4.05	4.01	4.00	3.99	
$\ \mathbf{u} - \Pi_h^{\text{cf}} \mathbf{u}\ _{0,\Omega}$	0.00288	0.00074	0.00019	0.00005	1.165e-05
R_l	3.89	3.97	3.99	4.00	
$ \mathbf{u} - \mathbf{u}_{h,1}^{\text{cf}} _{\mathbb{E},\Omega_h}$	0.05944	0.03226	0.01728	0.00918	0.00485
R_l	1.84	1.87	1.88	1.89	
$ \mathbf{u} - \Pi_h^{\text{cf}} \mathbf{u} _{\mathbb{E},\Omega_h}$	0.06185	0.03352	0.01787	0.00947	0.00500
R_l	1.85	1.88	1.89	1.89	
$\dim V_{h,2}^{\text{cf}}$	242	866	3 266	12 674	49 922
$\ \mathbf{u} - \mathbf{u}_{h,2}^{\text{cf}}\ _{0,\Omega}$	0.00042	0.00005	6.222e-06	8.559e-07	1.307e-07
R_l	8.56	7.79	7.27	6.55	
$\ \mathbf{u} - \Pi_h^{\text{cf}} \mathbf{u}\ _{0,\Omega}$	0.00043	0.00005	5.599e-06	6.951e-07	9.105e-08
R_l	9.12	8.50	8.05	7.63	
$ \mathbf{u} - \mathbf{u}_{h,2}^{\text{cf}} _{\mathbb{E},\Omega_h}$	0.03084	0.01174	0.00474	0.00212	0.00105
R_l	2.63	2.48	2.23	2.03	
$ \mathbf{u} - \Pi_h^{\text{cf}} \mathbf{u} _{\mathbb{E},\Omega_h}$	0.03580	0.01372	0.00564	0.00253	0.00123
R_l	2.61	2.43	2.23	2.06	
$\dim M_{h,1}^{\text{wc}}$	228	840	3 216	12 576	49 728
$\ \mathbf{u} - \mathbf{u}_{h,1}^{\text{wc}}\ _{0,\Omega}$	0.00061	0.00008	1.021e-05	1.377e-06	1.944e-07
R_l	7.78	7.73	7.41	7.08	
$\ \mathbf{u} - \Pi_h^{\text{wc}} \mathbf{u}\ _{0,\Omega}$	0.00050	0.00007	8.831e-06	1.157e-06	1.526e-07
R_l	7.43	7.59	7.63	7.58	
$ \mathbf{u} - \mathbf{u}_{h,1}^{\text{wc}} _{\mathbb{E},\Omega_h}$	0.02972	0.01295	0.00573	0.00265	0.00130
R_l	2.30	2.26	2.16	2.04	
$ \mathbf{u} - \Pi_h^{\text{wc}} \mathbf{u} _{\mathbb{E},\Omega_h}$	0.03263	0.01470	0.00680	0.00336	0.00180
R_l	2.22	2.16	2.02	1.86	
$\dim M_{h,2}^{\text{wc}}$	304	1 120	4 288	16 768	66 304
$\ \mathbf{u} - \mathbf{u}_{h,2}^{\text{wc}}\ _{0,\Omega}$	0.00027	0.00004	6.021e-06	8.172e-07	1.094e-07
R_l	6.62	6.85	7.37	7.47	
$\ \mathbf{u} - \Pi_h^{\text{wc}} \mathbf{u}\ _{0,\Omega}$	0.00015	1.710e-05	2.116e-06	2.715e-07	3.565e-08
R_l	8.57	8.08	7.79	7.61	
$ \mathbf{u} - \mathbf{u}_{h,2}^{\text{wc}} _{\mathbb{E},\Omega_h}$	0.01841	0.00799	0.00358	0.00165	0.00081
R_l	2.31	2.23	2.16	2.05	
$ \mathbf{u} - \Pi_h^{\text{wc}} \mathbf{u} _{\mathbb{E},\Omega_h}$	0.01741	0.00748	0.00339	0.00162	0.00081
R_l	2.33	2.21	2.09	2.00	

Table 4.6: L-shaped example: Energy and L_2 interpolation and approximation error for the bilinear and biquadratic discretizations on graded quadrilateral meshes corresponding to the singularity $\alpha^{\frac{3}{2}}$.

4.3 Locking phenomena

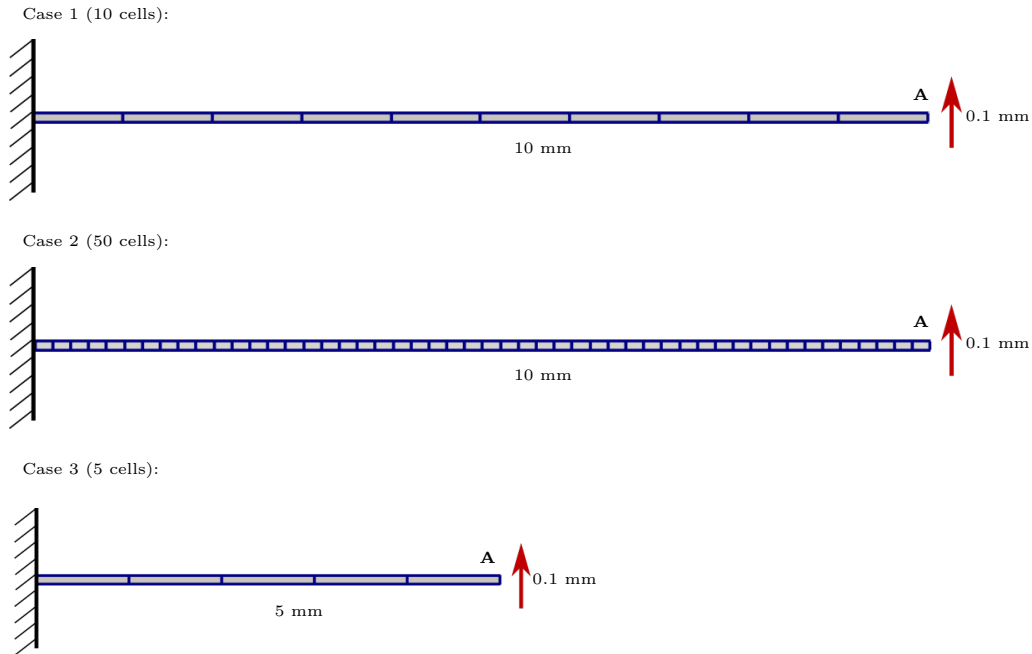


Figure 4.5: Thin beam example: The domains of the three considered configurations including boundary conditions and cell distributions.

The phenomena of *locking* is well-known and widespread in the field of numerical treatment of solid mechanical problems. It describes a stiffening of the discrete solution, leading to a very slow convergence. For details see for example [9]. Whether locking occurs depends on the considered example, but also on the chosen discretization, for example simple low order conforming methods provide heavy locking. There are many *locking-free elements* and in this section we want to test, whether this holds true for the weakly conforming method as well.

For this test we compute three thin beams, which are fixed on the left side and loaded vertically on the right side. Two of those beams are identical in their dimensions, but are discretized in different manners. All three beam have one starting cell layer in vertical direction a height of 0.1 mm, but not all are of the same length. Case 1 has a length of 10 mm and is discretized with 10 cells in horizontal direction, which means, that the cells have a length/height ratio

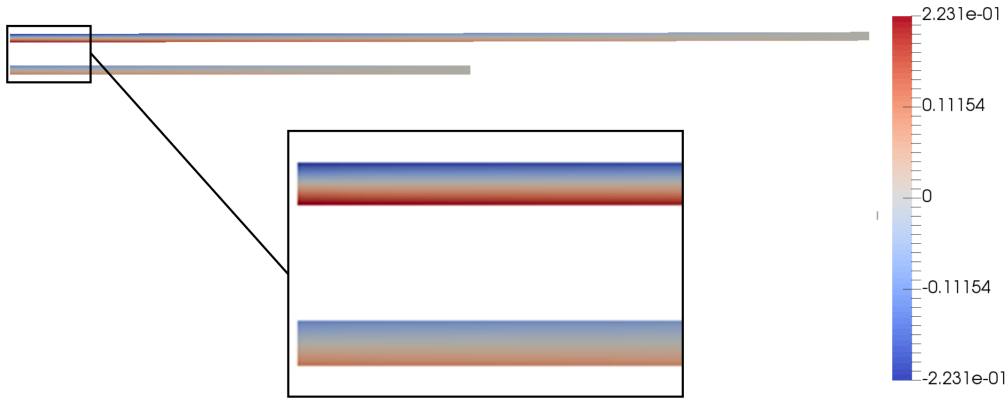


Figure 4.6: Thin beam example: Distribution of $|\boldsymbol{\sigma}(\mathbf{u})|$ for the 10 mm long beams and the 5 mm long beam, as well as a close-up of the Dirichlet boundary and the nearby region.

of 10. Case 2 has the length 10 mm as well, but is discretized with 50 starting cells in horizontal direction, the ratio is therefore only 2. In case 3 we have only a length of 5 mm, but cells with the same length/height ratio as in Case 1, because we only use 5 cells for the starting mesh of this beam. Since we want to test the artificial increased stiffness of the methods, we use the vertical deformation $u_2(\mathbf{A})$ at a point \mathbf{A} , which is placed on the right side of the beams, as a measurement. The geometry of the beams, the boundary conditions and the test point \mathbf{A} are shown in Fig. 4.5. On the Neumann boundary $\partial\Omega_N$ a downward pressure of 0.001 MPa is applied in all cases. As a material we use a isotropic linear elastic one with the Lamé parameter $E = 16.8 \text{ GPa}$ and $\nu = 0.4$.

In Tab. 4.7 the results of case 1 are given. We can see, that we have two schemes which show locking, namely the linear conforming method and the linear discontinuous Galerkin method. The locking effect makes itself noticeable with high relative errors in lower levels and low experimental orders of convergence for both schemes. The other four provide significantly better results even on the lowest levels. The fact, that the lowest order weakly conform-

$\dim V_{h,1}^{\text{cf}}$	1 458		5 474		21 186
$u_2(\mathbf{A})$	0.01344		0.01780		0.01938
difference		0.0044		0.0016	
R_l			2.75		
$\dim V_{h,2}^{\text{cf}}$	4 194		16 066		62 850
$u_2(\mathbf{A})$	0.019949		0.019973		0.019983
difference		2.42e-05		9.8e-06	
R_l			2.47		
$\dim V_{h,1}^{\text{dG}}$	1 280		5 120		20 480
$u_2(\mathbf{A})$	0.01307		0.01740		0.01924
difference		0.00434		0.00184	
R_l			2.36		
$\dim V_{h,2}^{\text{dG}}$	2 880		11 520		46 080
$u_2(\mathbf{A})$	0.0199954		0.0199942		0.01999
difference		1.201e-06		4.20e-06	
R_l			0.29		
$\dim M_{h,1}^{\text{wc}}$	4 104		15 888		62 496
$u_2(\mathbf{A})$	0.0199975		0.019994		0.0199914
difference		3.445e-06		2.655e-06	
R_l			1.30		
$\dim M_{h,2}^{\text{wc}}$	5 136		20 512		81 984
$u_2(\mathbf{A})$	0.0199845		0.0199842		0.0199771
difference		2.715e-07		7.082e-06	
R_l			0.04		

Table 4.7: Case 1 of the thin beam example: Comparison of $u_2(\mathbf{A})$ for the different discretization schemes, including experimental rate of convergence between levels (R_l).

dim $V_{h,1}^{\text{cf}}$	7 218		27 234		105 666
$u_2(\mathbf{A})$	0.01937		0.01983		0.01995
difference		4.594e-04		1.196e-04	
R_l			3.84		
dim $V_{h,2}^{\text{cf}}$	20 834		80 066		313 730
$u_2(\mathbf{A})$	0.019983		0.0199856		0.0199863
difference		2.606e-06		7.268e-07	
R_l			3.59		
dim $V_{h,1}^{\text{dG}}$	25 600		102 400		409 600
$u_2(\mathbf{A})$	0.0197231		0.0199174		0.0199703
difference		1.94e-04		5.29e-05	
R_l			3.67		
dim $V_{h,2}^{\text{dG}}$	57 600		230 400		921 600
$u_2(\mathbf{A})$	0.0199792		0.0199877		0.0199852
difference		8.50e-06		2.50e-06	
R_l			3.40		
dim $M_{h,1}^{\text{wc}}$	20 424		79 248		312 096
$u_2(\mathbf{A})$	0.0199882		0.0199867		0.0199843
difference		1.425e-06		2.379e-06	
R_l			0.60		
dim $M_{h,2}^{\text{wc}}$	25 616		102 432		409 664
$u_2(\mathbf{A})$	0.0199874		0.0199878		0.0199859
difference		3.858e-07		1.818e-06	
R_l			0.212		

Table 4.8: Case 2 of the thin beam example: Comparison of $u_2(\mathbf{A})$ for the different discretization schemes, including experimental rate of convergence between levels (R_l).

ing method does not show signs of locking, might be explained by the fact, that there is no truly linear version of this discretization family and the lowest order method includes already quadratic polynomial spaces inside the cells. Another observation is, that all methods can provide convergence only up to a certain level. All methods start to oscillate around values in the range of $u_2(\mathbf{A}) \in [0.0199, 0.02]$ and have varying values for R_l , which makes it impossible to estimate κ . This behavior can be explained with the ill-posedness of the problem. The beam itself has a high length/height ratio of 100 and the cells have a comparable high dimensional ratio as well, which makes this problem hard to solve and prone to errors.

In Tab. 4.8 we can see the results for case 2, where we use the same geometry, which is this time subdivided into more vertical cells compared to case 1. The results are similar, but less pronounced than before. Again, the linear conforming method and the linear discontinuous Galerkin method start with

dim $V_{h,1}^{\text{cf}}$	738		2754		10626
$u_2(\mathbf{A})$	0.00167		0.00222		0.00242
difference		5.461e-04		2.004e-04	
R_l			2.72		
dim $V_{h,2}^{\text{cf}}$	2114		8066		31490
$u_2(\mathbf{A})$	0.00248763		0.00249371		0.0024961
difference		6.085e-06		2.389e-06	
R_l			2.55		
dim $V_{h,1}^{\text{dG}}$	2560		10240		40960
$u_2(\mathbf{A})$	0.00217736		0.00240484		0.00247341
difference		2.275e-04		6.857e-05	
R_l			3.32		
dim $V_{h,2}^{\text{dG}}$	5760		23040		92160
$u_2(\mathbf{A})$	0.00249904		0.00249803		0.00249732
difference		1.01e-06		7.036e-07	
R_l			1.44		
dim $M_{h,1}^{\text{wc}}$	2064		7968		31296
$u_2(\mathbf{A})$	0.00250006		0.00249931		0.00249871
difference		7.496e-07		5.966e-07	
R_l			1.26		
dim $M_{h,2}^{\text{wc}}$	2576		10272		41024
$u_2(\mathbf{A})$	0.00249695		0.00249778		0.00249753
difference		8.278e-07		2.423e-07	
R_l			3.42		

Table 4.9: Case 3 of the thin beam example: Comparison of $u_2(\mathbf{A})$ for the different discretization schemes, including experimental orders of convergence.

higher relative errors than the other method and converge slowly towards the correct solution. The oscillation of the other methods is also still there, but in a damped form. Again, the experimental orders of convergence for the weakly conforming method is low, but its results are very close to the estimated solution, even on the coarse refinement levels, which explains again the lack of convergence due to the high influence of rounding errors and high condition numbers.

The results of case 3 can be seen in Tab. 4.9. This case is very similar in its difficulty to case 2, since the beam is shorter, but less refined, which results in comparable level of difficulty. Again, the locking methods are lacking behind the others, in terms of relative error and again no method shows a clear pattern of convergence when it is close to the estimated solution, only the $\mathbb{P}_3\mathbb{P}_1$ version of the weakly conforming method has an adequate high experimental convergence rate, which however might not hold for further refinement steps.

In these tests we could observe, that both discussed orders of the weakly

conforming method show no signs of locking. In Fig. 4.7 it becomes clear, which methods are locking and which are not. The oscillatory behavior of all methods are probably caused by the errors due to the stopping criteria of the underlying solvers and by rounding errors, which are amplified by the ill-posed nature of this example.

It is notable for the weakly conforming method, that in cases 1 and 2 it was beneficiary to increase V_K , which is why we computed these cases with the $\mathbb{P}_4\mathbb{P}_1$ version of the weakly conforming method. This increases the assembly time of the local matrices, but bettered the performance significantly, due to the increased robustness.

4.4 Geometrical anisotropy

In the next test we increase the difficulty of the computation and consider anisotropic meshes. For this we discretize a thin plate $\Omega = \omega \times (0, 0.01) \text{ mm}^3$ with $\omega = (0, 1)^2$. The plate is loaded by a constant normal pressure $\mathbf{t}_N = 10^{-7} \text{ N} \cdot \mathbf{n}$ on the top boundary $\partial\Omega_{0.01} = \omega \times \{0.01\}$ and fixed on the sides, i.e., we impose homogeneous Dirichlet boundary on $\partial\Omega_D = \partial\omega \times [0, 0.01]$. The material is compressible with $E = 250 \text{ MPa}$ and $\nu = 0.3$. The applied force results into a very small deformation so that linearized elasticity is appropriate.

For this test we compare two different mesh refinement strategies for linear and higher order approximations. The first strategy is uniform refinement in all three spatial dimensions, which results in similar cells on all mesh refinement levels. For the second refinement strategy we refine the cells only in the two horizontal directions, but leave the vertical direction at the four starting cell layers. This results in cells which change their height to width ratio with each refinement level.

Asymptotic convergence usually requires refinement in all directions. However, for the second order methods, convergence up to the prescribed accuracy is observed for both strategies. This leads for the second strategy to a reduced number of degrees of freedom and a high efficiency. In Fig. 4.9 we present the results of this two-dimensional refinement strategy and for comparison, also the results for the full refinement. We observe that the results of both lowest

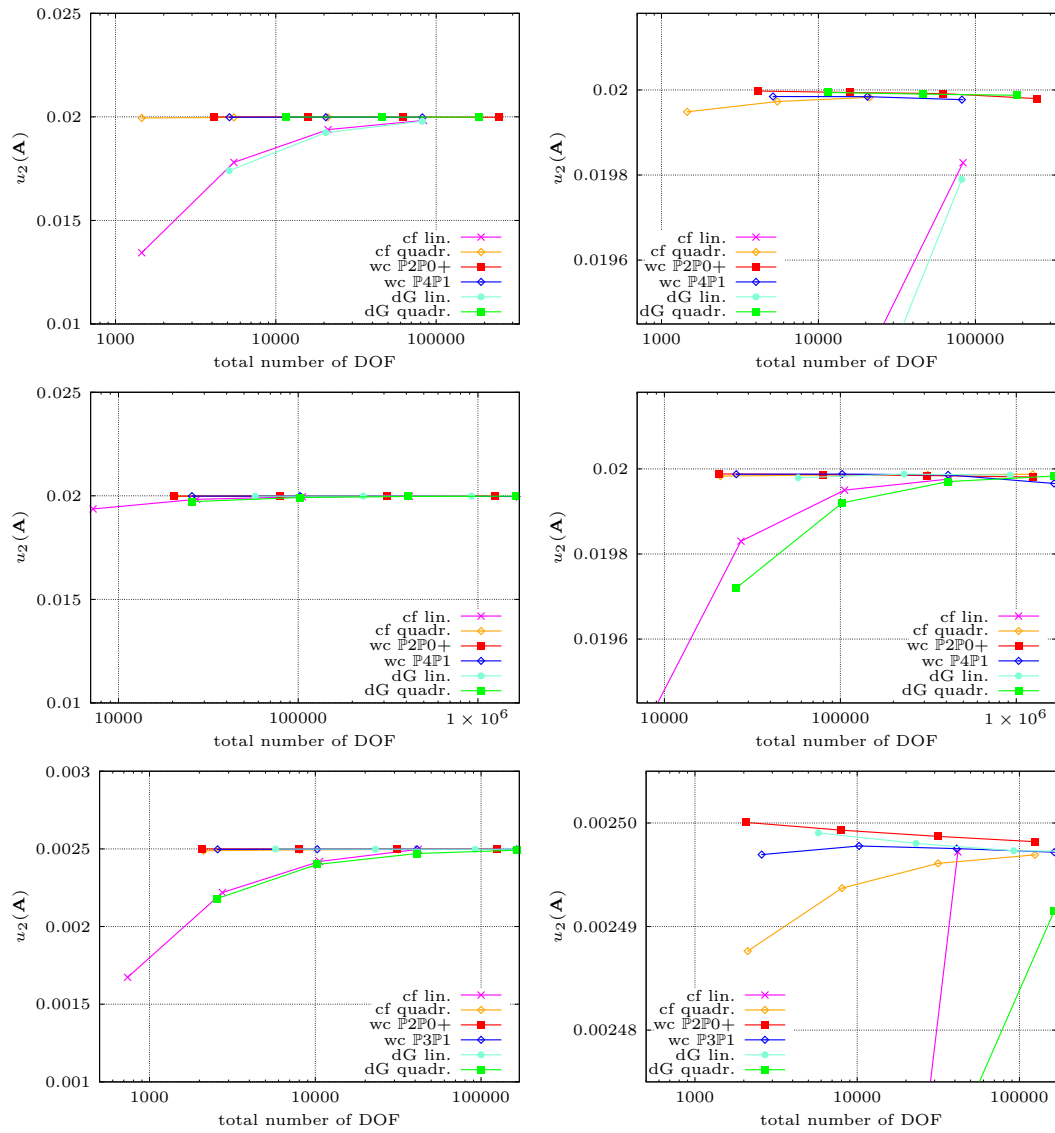


Figure 4.7: Thin beam example: Study of locking behavior for all discussed schemes. On the left side $u_2(\mathbf{A})$ is depicted for all cases, on the right side a zoom-in is provided. From top to bottom: Case 1, case 2, case 3.

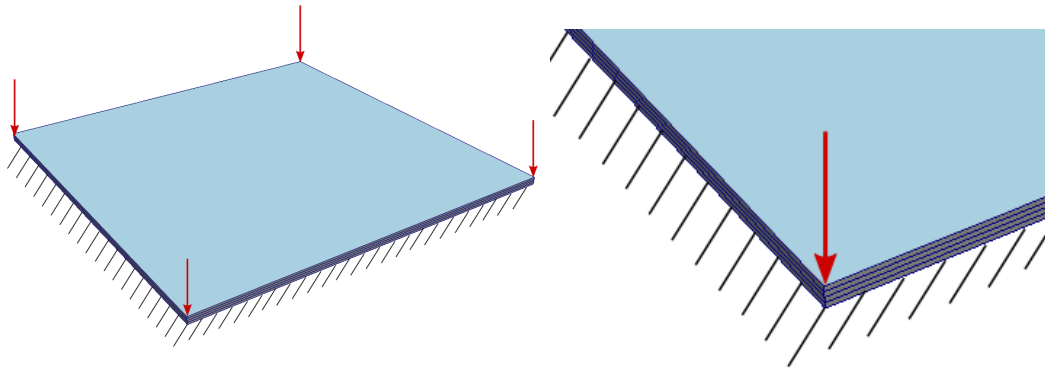


Figure 4.8: Thin plate example: Geometric configuration of the thin plate and a close-up of one corner, illustrating the cell layers.

order methods are not optimal, since the weakly conforming method converges towards a wrong, albeit somewhat accurate solution, whereas the linear conforming method converges only very slowly. Both higher order methods are quite accurate with only few degrees of freedom, indicating a strong robustness with respect to the anisotropic cells of this refinement method. In Tab. 4.10 this observation can be checked. The experimental orders of convergence for the high order methods are surprisingly high for this incomplete refinement strategy, with $R \approx 2$. The rates for the $\mathbb{P}_2\mathbb{P}_{0+}$ weakly conforming method are high as well, but not useful since it converges towards a wrong solution.

These observations are less pronounced when the full refinement is applied. The efficiency of the high order methods is worse than before, which is expected since they handled the incomplete refined already sufficiently well and do not benefit from the additional degrees of freedom and the over-refinement in the vertical direction. However, the lowest order weakly conforming method performs significantly better with this setup, it is even more efficient than the quadratic conforming method. In Tab. 4.11 $R_l \approx 2$ for both weakly conforming methods and the quadratic conforming method can be seen. The linear conforming method shows again severe locking and needs a huge amount of degrees of freedom to produce even remotely accurate solutions, with an R_l which is slowly climbing upwards with increasing refinement. We omitted the last refinement level of the higher order weakly conforming method, since it is already close enough to the exact solution.

$\dim V_{h,1}^{\text{cf}}$	1 215		4 335		16 335		63 375
$\ \mathbf{u}_h\ _{0,\partial\Omega_{0.01}} \cdot 10^6$	0.201		0.637		1.396		1.994
difference		0.436		0.759		0.598	
R_l			0.57		1.27		
$\dim V_{h,2}^{\text{cf}}$	4 347		15 963		61 083		238 875
$\ \mathbf{u}_h\ _{0,\partial\Omega_{0.01}} \cdot 10^6$	2.303		2.344		2.356		2.361
difference		0.041		0.012		0.005	
R_l			3.42		2.4		
$\dim M_{h,1}^{\text{wc}}$	3 328		13 056		51 712		205 824
$\ \mathbf{u}_h\ _{0,\partial\Omega_{0.01}} \cdot 10^6$	2.417		2.397		2.391		2.389
difference		0.020		0.006		0.002	
R_l			3.33		3.00		
$\dim M_{h,2}^{\text{wc}}$	9 088		35 840		142 336		567 296
$\ \mathbf{u}_h\ _{0,\partial\Omega_{0.01}} \cdot 10^6$	2.352		2.359		2.363		2.364
difference		0.007		0.004		0.001	
R_l			1.75		4.00		

Table 4.10: Thin plate example, refinement in the two horizontal directions: Comparison of $\|\mathbf{u}_h\|_{0,\partial\Omega_{0.01}}$ for the different discretization schemes, including experimental orders of convergence.

$\dim V_{h,1}^{\text{cf}}$	1 215		7 803		55 539		418 275
$\ \mathbf{u}_h\ _{0,\partial\Omega_{0.01}} \cdot 10^6$	0.2006		0.6388		1.407		2.017
difference		0.4382		0.7682		0.6101	
R_l			0.57		1.26		
$\dim V_{h,2}^{\text{cf}}$	4 347		29 427		215 523		1 647 555
$\ \mathbf{u}_h\ _{0,\partial\Omega_{0.01}} \cdot 10^6$	2.303		2.345		2.357		2.362
difference		0.042		0.012		0.005	
R_l			3.59		2.75		
$\dim M_{h,1}^{\text{wc}}$	3 328		25 600		200 704		158 9248
$\ \mathbf{u}_h\ _{0,\partial\Omega_{0.01}} \cdot 10^6$	2.417		2.380		2.369		2.367
difference		0.037		0.011		0.002	
R_l			3.62		3.88		
$\dim M_{h,2}^{\text{wc}}$	9 088		73 216		587 776		
$\ \mathbf{u}_h\ _{0,\partial\Omega_{0.01}} \cdot 10^6$	2.352		2.359		2.362		
difference		0.007		0.003			
R_l			2.33				

Table 4.11: Thin plate example, refinement in all three directions: Comparison of $\|\mathbf{u}_h\|_{0,\partial\Omega_{0.01}}$ for the different discretization schemes, including experimental orders of convergence.

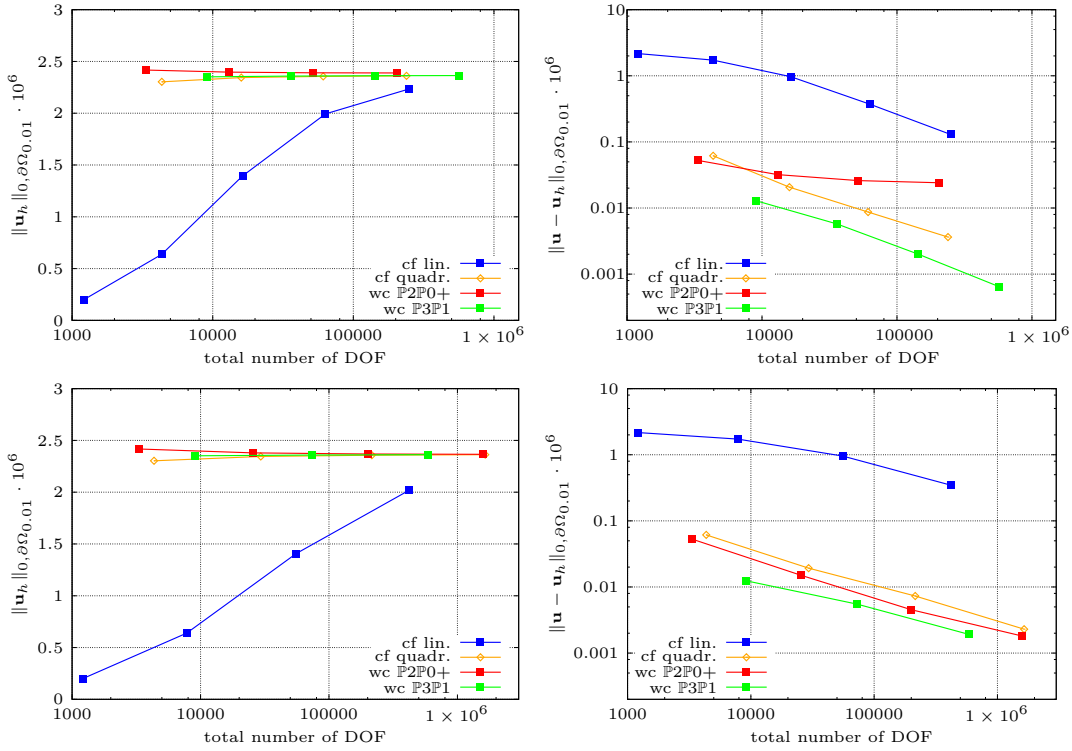


Figure 4.9: Thin plate example: Refinement of the plate in both horizontal directions only (top) and refinement in all directions (bottom). On the left, the resulting surface displacement $\|\mathbf{u}_h\|_{0, \partial\Omega_{0,01}}$ and on the right the corresponding error (estimated by extrapolation) is shown.

Together, this two scenarios for the thin plate indicate a strong robustness towards anisotropy for meshes with a ratio of width to height of 1 to 1000 for the weakly conforming method.

4.5 Material-induced anisotropy

For a robustness test of the weakly conforming method with respect to material interfaces we now consider a bi-material ring consisting of two layers: an incompressible rubber-type inner layer with $E = 10$ MPa and $\nu = 0.499$, and a compressible metal like outer layer with $E = 20000$ MPa and $\nu = 0.285$. The ring has an inner radius of 50 cm and an outer radius of 110 cm and the material boundary between the two layers has a radius of 100 cm, see Fig. 4.10.

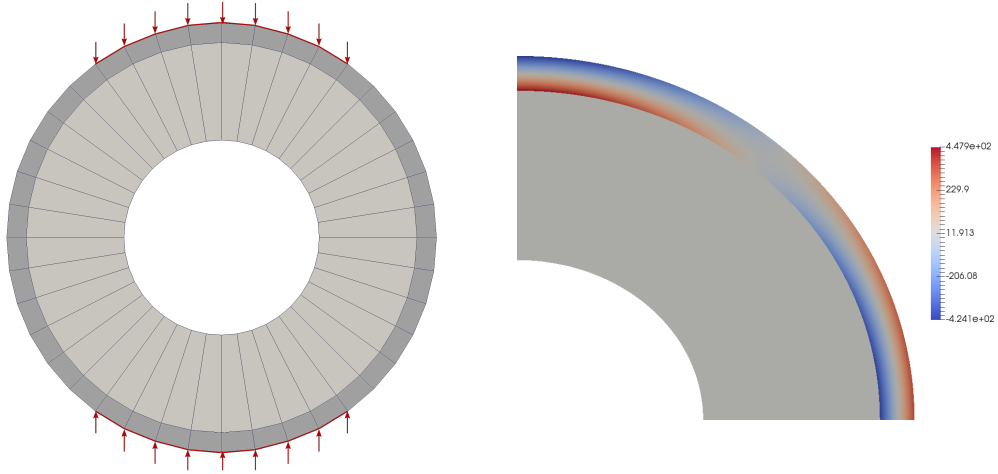


Figure 4.10: Bi-material ring example: Geometric configuration (left), distribution of $|\boldsymbol{\sigma}(\mathbf{u})|$, visualized on the quarter of the ring (right) which is used for the computations.

A traction force is acting symmetrically on top and on bottom. Due to the symmetry of the solution, the computation can be reduced to one quarter of the ring, and we use symmetry boundary conditions for $x_1 = 0$ and $x_2 = 0$.

We apply on the outer boundary $\partial\Omega_{110}$ a traction force $\mathbf{t}_N = (-1, 0, 0)^\top \text{ N}$, see Fig. 4.10 for the resulting stress distribution. The values of the stress $\boldsymbol{\sigma}(\mathbf{u})$ are much higher in the metal part, so that we clearly identify the material interface. For the a posteriori analysis of this example, we use a highly refined solution and extrapolate an accurate approximation \mathbf{u} to estimate the errors of all methods.

The displacement results $\|\mathbf{u}\|_{\partial\Omega_{110}}$ and the error with respect to the problem size are shown in Fig. 4.11. It becomes evident, that the linear conforming method does only provide a somewhat accurate approximation on finer meshes, with a high number of degrees of freedom. The material jump between the layers of the ring seems to impose a problem. On the other hand, the quadratic conforming method and both weakly conforming methods converge quickly towards the same solution and converge with the same rate towards the estimated solution \mathbf{u} . In Tab. 4.12 the experimental rate of convergence can be seen and two things are striking: The $\mathbb{P}_3\mathbb{P}_1$ variant of the weakly conforming method has a lower rate of convergence than expected, with $R_l \approx 3.65$, though it is climbing, which could mean, that this is only pre-asymptotic. On the

$\dim V_{h,1}^{\text{cf}}$	10 626	41 730	165 378	658 434
$\ \mathbf{u} - \mathbf{u}_h\ _{0,\partial\Omega_{110}}$	108.84677	109.39147	109.54768	109.58869
difference		0.54470	0.15620	0.04101
R_l		3.49	3.81	
$\dim V_{h,2}^{\text{cf}}$	31 490	124 418	494 594	1 972 226
$\ \mathbf{u} - \mathbf{u}_h\ _{0,\partial\Omega_{110}}$	109.60112	109.60233	109.60251	109.60255
difference		0.00121	1.798e-04	3.540e-05
R_l		6.74	5.08	
$\dim M_{h,1}^{\text{wc}}$	30 912	123 264	492 288	1 967 616
$\ \mathbf{u} - \mathbf{u}_h\ _{0,\partial\Omega_{110}}$	109.60682	109.60302	109.60260	109.60256
difference		0.00380	4.215e-04	3.724e-05
R_l		9.02	11.32	
$\dim M_{h,2}^{\text{wc}}$	40 960	163 840	655 360	2 621 440
$\ \mathbf{u} - \mathbf{u}_h\ _{0,\partial\Omega_{110}}$	109.60208	109.60242	109.60252	109.60255
difference		3.328e-04	1.047e-04	2.870e-05
R_l		3.18	3.65	

Table 4.12: Bi-material ring example: Comparison of $\|\mathbf{u} - \mathbf{u}_h\|_{0,\partial\Omega_{110}}$ for conforming and weakly conforming methods, including experimental rate of convergence between levels (R_l).

other hand, the $\mathbb{P}_2\mathbb{P}_{0+}$ variant exhibits an R_l which is higher than expected. This may be caused by the normal degrees of freedom which are added to $M_{h,1}^{\text{wc}}$, since the $\mathbb{P}_3\mathbb{P}_1$ does not feature this type of degree of freedom. It could also be another pre-asymptotic behavior.

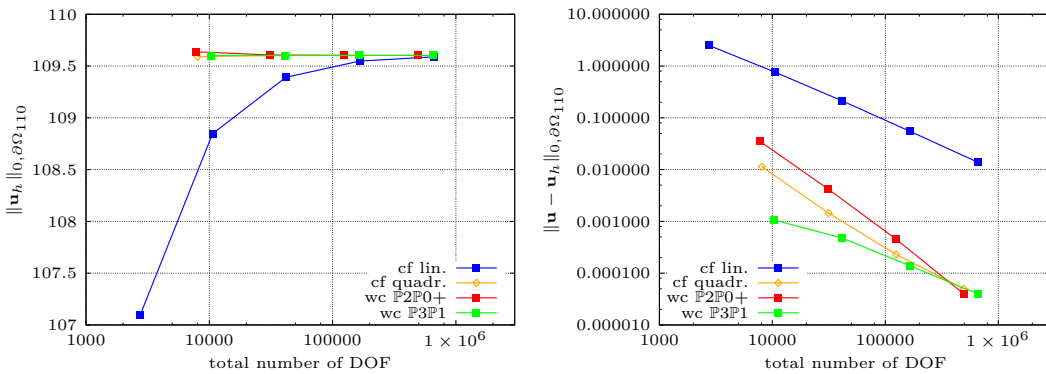


Figure 4.11: Bi-material ring example: Convergence of $\|\mathbf{u}_h\|_{\partial\Omega_{110}}$ for the different methods (left) and the error (right) estimated by extrapolation.

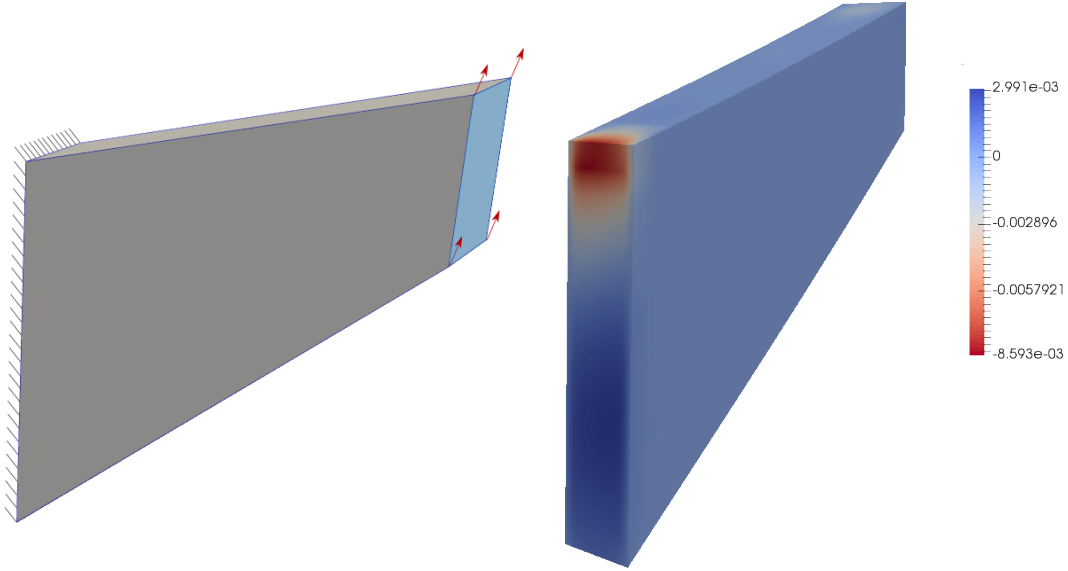


Figure 4.12: Cook's membrane: Domain including boundary conditions (left) and distribution of $|\boldsymbol{\sigma}(\mathbf{u})|$ (right) clearly indicating the stress singularity at the top edge of the Dirichlet boundary.

4.6 Incompressible materials - dependency on material parameters

In the last example of this chapter we demonstrate robustness of the weakly conforming method with respect to incompressibility. The compressibility of an elastic material is described by its Poisson ratio ν . If $\nu = 0.5$, the volume of the material does not change, when pressure or tractive forces are applied. In reality, a Poisson ratio of nearly 0.5 occurs for example in certain rubbers, whereas materials like metals usually are compressible with $\nu \approx 0.3$. From a numerical point of view, the computation of such materials can be an obstacle, if the error of the method depends on the material parameters. Such values of μ cause λ to blow up, since $\lambda = \frac{E\nu}{(1+\nu)(1-2\nu)} \rightarrow \infty$ for $\mu \rightarrow 0.5$.

To test the behavior of our method with respect to $\nu \approx 0.5$ we consider Cook's membrane in 3d given by $\Omega = \text{conv}\{(0, 0), (0, 44), (48, 44), (48, 60)\} \times (0, 1)$, cf. Fig. 4.12, with elasticity module $E = 2.5$ MPa and the Poisson ratios $\nu \in \{0.25, 0.49, 0.49999\}$. The domain is fixed on $\Omega_D = \{0\} \times [0, 44] \times [0, 1]$ with homogeneous Dirichlet boundary conditions $\mathbf{u}_D = \mathbf{0}$, and on the left side

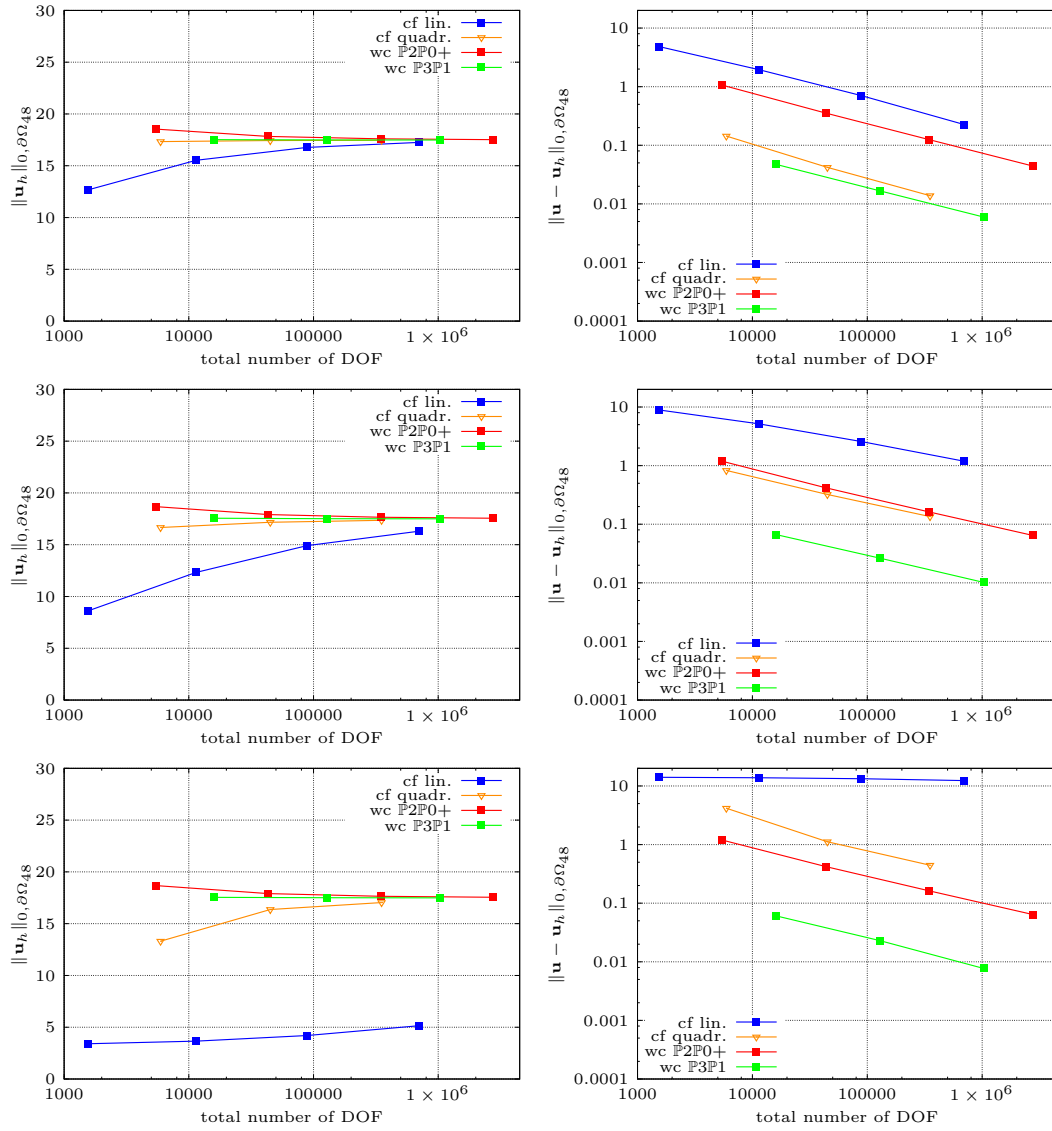


Figure 4.13: Cook's membrane: The resulting surface displacement $\|\mathbf{u}_h\|_{0, \{48\} \times (44, 60) \times (0, 1)}$ (left) and the error (right) estimated by extrapolation for different discretizations, $\nu = 0.25, 0.49, 0.49999$ (from top to bottom).

$\{48\} \times (44, 60) \times (0, 1)$ the traction force $\mathbf{t} = (0.002, -0.02, 0)^\top \text{N}$ is applied.

The resulting displacement at the face $x_1 = 48$ is compared for the different discretizations and materials, cf. Fig. 4.13. We observe that

- for the compressible material with $\nu = 0.25$ all tested discretizations resolve the problem sufficiently well with a reasonable computational effort, but the weakly conforming methods are more efficient with respect to the number of degrees of freedom compared to the conforming methods.
- For $\nu = 0.49$ the errors of the conforming methods increase significantly. The weakly conforming method again achieves a smaller error with less global degrees of freedom, but additionally the error does almost not change compared to the previous computation. This constitutes a huge gap in efficiency between the respective conforming and weakly conforming methods, compared to the more compressible material. The conforming quadratic method on the highest mesh refinement level needs about 200 times more degrees of freedom as the $\mathbb{P}_3\mathbb{P}_1$ method on the lowest level. Yet it has still a higher error compared to its competitor.
- For the incompressible material $\nu = 0.49999$ the conforming methods are completely locking with a large relative and absolute error, especially the linear scheme does not produce a suitable solution on any level. In contrast, the weakly conforming methods provides robust results with respect to incompressibility. The error changes again only by a small margin, compared to the other material settings. This indicates, that the error of the weakly conforming approximation does not depend on the material parameters.

This observation is punctuated by the comparison of the quadratic methods in Fig. 4.14 and by Tab.4.13. The quality of the approximation seems to be nearly independent of the Poisson number for the weakly conforming method, where $R_l \approx 3$ remains nearly the same, whereas the results for the conforming method heavily depend on ν . The experimental rate of convergence for the quadratic conforming method stays high with increasing ν , however the error constant is increasing significantly. Computations of nearly incompressible materials should therefore not be conducted with conforming methods and should rather be substituted by computations with more sophisticated schemes.

$\dim V_{h,1}^{\text{cf}}$	1 551		11 451		88 563
$\ \mathbf{u} - \mathbf{u}_h\ _{0,\partial\Omega_{48}}, \nu = 0.25$	12.66533		15.52933		16.77254
difference		2.86400		1.24321	
R_l			2.30		
$\ \mathbf{u} - \mathbf{u}_h\ _{0,\partial\Omega_{48}}, \nu = 0.49$	8.60550		12.33082		14.90968
difference		3.72532		2.57886	
R_l			1.44		
$\ \mathbf{u} - \mathbf{u}_h\ _{0,\partial\Omega_{48}}, \nu = 0.49999$	3.40223		3.65779		4.20172
difference		0.25556		0.54392	
R_l			0.47		
$\dim V_{h,2}^{\text{cf}}$	5 931		44 979		351 459
$\ \mathbf{u} - \mathbf{u}_h\ _{0,\partial\Omega_{48}}, \nu = 0.25$	17.33334		17.43497		17.46320
difference		0.10163		0.02823	
R_l			3.60		
$\ \mathbf{u} - \mathbf{u}_h\ _{0,\partial\Omega_{48}}, \nu = 0.49$	16.66127		17.16827		17.35505
difference		0.50700		0.18678	
R_l			2.71		
$\ \mathbf{u} - \mathbf{u}_h\ _{0,\partial\Omega_{48}}, \nu = 0.49999$	13.31185		16.36798		17.03996
difference		3.05612		0.67198	
R_l			4.54		
$\dim M_{h,1}^{\text{wc}}$	5 488		43 456		345 856
$\ \mathbf{u} - \mathbf{u}_h\ _{0,\partial\Omega_{48}}, \nu = 0.25$	18.53617		17.83157		17.60176
difference		0.70461		0.22981	
R_l			3.07		
$\ \mathbf{u} - \mathbf{u}_h\ _{0,\partial\Omega_{48}}, \nu = 0.49$	18.67627		17.90905		17.65176
difference		0.76722		0.25729	
R_l			2.98		
$\ \mathbf{u} - \mathbf{u}_h\ _{0,\partial\Omega_{48}}, \nu = 0.49999$	18.67650		17.90593		17.64647
difference		0.77057		0.25946	
R_l			2.97		
$\dim M_{h,2}^{\text{wc}}$	15 984		128 448		1 029 888
$\ \mathbf{u} - \mathbf{u}_h\ _{0,\partial\Omega_{48}}, \nu = 0.25$	17.52438		17.49372		17.48297
difference		0.03066		0.01075	
R_l			2.85		
$\ \mathbf{u} - \mathbf{u}_h\ _{0,\partial\Omega_{48}}, \nu = 0.49$	17.55685		17.51637		17.50017
difference		0.04048		0.01620	
R_l			2.50		
$\ \mathbf{u} - \mathbf{u}_h\ _{0,\partial\Omega_{48}}, \nu = 0.49999$	17.5449		17.507		17.4917
difference		0.0379		0.0153	
R_l			2.48		

Table 4.13: Cook's membrane: Comparison of $\|\mathbf{u} - \mathbf{u}_h\|_{0,\partial\Omega_{110}}$ for conforming and weakly conforming methods for $\nu = 0.25, 0.49, 0.49999$, including experimental rate of convergence between levels (R_l).

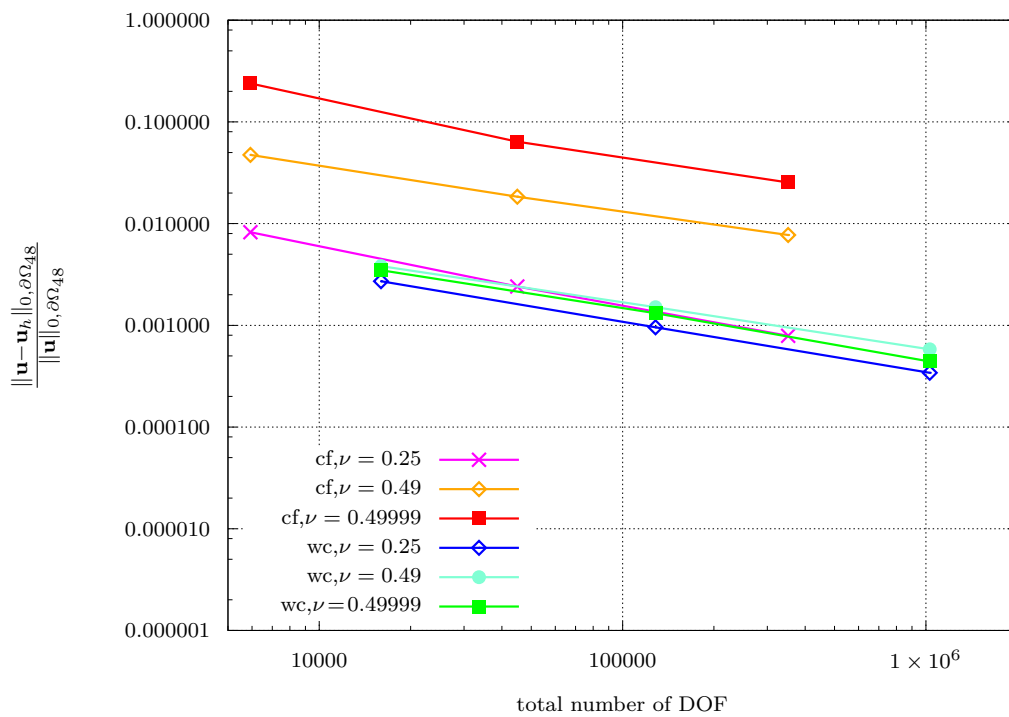


Figure 4.14: Cook's membrane: Relative errors for the quadratic conforming and $\mathbb{P}_3\mathbb{P}_1$ weakly conforming methods. Nearly no change for the weakly conforming method, while the conforming method is deteriorating with increasing ν .

Chapter 5

A priori error analysis of the weakly conforming method and adaptive applications

Content of this chapter The following chapter discusses the question of a priori error estimation. This is important for targeted mesh or polynomial refinement, since in general we do not know a priori in which parts of the domain we need more or less degrees of freedom. In this chapter we will first develop and analyze the error estimator, after which we will use this estimator to formulate an adaptive algorithm. Lastly the adaptive results of two examples will be shown for different refinement strategies. This includes a comparison with uniform refinement.

Origin of this chapter The main part of this chapter is published together with Christian Wieners and Barbara Wohlmuth and can be found at [44]. Some of the numerical results for the adaptive strategies on the L-shaped domain will be published in our final report of the SPP 1748 [15].

5.1 A residual error estimator

In the following we assume that at least $M_F^{\min} \subset M_F$ so that the broken Korn estimate (3.10) is satisfied. Then, the weakly conforming finite element system is positive definite, and a unique solution $\mathbf{u}_h^{\text{wc}} \in V_h^{\text{wc}}(\mathbf{u}_D)$ solving (3.8) exists.

The weakly conforming discretization is equivalent to an element-based mortar finite element method [59]. Based on the Strang Lemma, an *a priori error bound* can be derived by estimating separately the approximation error and the consistency error. We use the estimate [35, Lem. 1.59] for the L_2 projection $\Pi_K^0: L_2(\Omega) \rightarrow \mathbb{P}_0(K)$

$$\begin{aligned} \|\mathbf{v}_K - \Pi_F^{\text{wc}} \mathbf{v}_K\|_{0,F} &\leq \|\mathbf{v}_K - \Pi_K^0 \mathbf{v}_K\|_{0,F} \leq C_{0,K} h_K^{\frac{1}{2}} \|\mathbf{v}_K\|_{1,K}, \\ \left(\sum_K \sum_{F \in \mathcal{F}_K \setminus \partial\Omega_N} h_K^{-1} \|\mathbf{v}_K - \hat{\Pi}_F^{\text{wc}} \mathbf{v}_K\|_{0,F}^2 \right)^{\frac{1}{2}} &\leq C_0 \|\mathbf{v}\|_{1,\Omega_h}, \end{aligned} \quad (5.1)$$

with $\mathbf{v}_K \in H^1(K)$, $F \in \mathcal{F}_K$, $\mathbf{v} \in H^1(\Omega_h)$ and constants $C_{0,K}, C_0 > 0$ depending on the mesh regularity.

On the skeleton $\partial\Omega_h = \bigcup_{F \in \mathcal{F}_h \setminus \partial\Omega_N} F$, we introduce the mesh-dependent norms

$$\|\mathbf{v}\|_{\frac{1}{2}, \partial\Omega_h} = \left(\sum_K \sum_{F \in \mathcal{F}_K \setminus \partial\Omega_N} h_K^{-1} \|\mathbf{v}\|_{0,F}^2 \right)^{\frac{1}{2}}, \quad \|\boldsymbol{\mu}\|_{-\frac{1}{2}, \partial\Omega_h} = \left(\sum_K \sum_{F \in \mathcal{F}_K \setminus \partial\Omega_N} h_K \|\boldsymbol{\mu}\|_{0,F}^2 \right)^{\frac{1}{2}} \quad (5.2)$$

for $\mathbf{v}, \boldsymbol{\mu} \in L_2(\partial\Omega_h; \mathbb{R}^{\text{dim}})$. Using the scaled L_2 norms approximates the traces norms in $H^{\frac{1}{2}}$ and $H^{-\frac{1}{2}}$ for finite element functions. Note that for infinite dimensional spaces the norms are not equivalent. In the following lemma, an *a priori error bound* is derived, with a constant that only depends on the mesh parameters through $\|\mathbb{C}^{-\frac{1}{2}}\|_{\infty, \Omega}$ which is bound by $\frac{1}{\mu}$ for $\lambda \rightarrow \infty$ for isotropic linear elasticity. This shows, why the weakly conforming method is robust with respect to incompressibility in this case, since $\lim_{\nu \rightarrow 0.5} \lambda \rightarrow \infty$.

Lemma 7. *Let $\mathbf{u} \in V(\mathbf{u}_D)$ be the solution of the continuous problem, and let $\mathbf{u}_h^{\text{wc}} \in V_h^{\text{wc}}(\mathbf{u}_D)$ be the solution of the weakly conforming approximation (3.8). If the solution is sufficiently smooth with $\boldsymbol{\sigma}\mathbf{n}_F \in L_2(F; \mathbb{R}^{\text{dim}})$ for all $F \in \mathcal{F}_h \setminus \partial\Omega_N$, the error can be bounded by*

$$\|\mathbf{u} - \mathbf{u}_h^{\text{wc}}\|_{E, \Omega_h} \leq 2 \inf_{\mathbf{w}_h \in V_h^{\text{wc}}(\mathbf{u}_D)} \|\mathbf{u} - \mathbf{w}_h\|_{E, \Omega_h} + C \inf_{\boldsymbol{\mu}_h \in M_h} \|\boldsymbol{\sigma}\mathbf{n} - \boldsymbol{\mu}_h\|_{-\frac{1}{2}, \partial\Omega_h}$$

with a constant $C > 0$ depending on the mesh regularity, on \hat{C}_K , and on $\|\mathbb{C}^{-\frac{1}{2}}\|_{\infty, \Omega}$.

Proof. The proof for this lemma is taken from [44].

Evaluating (3.6) for $\mathbf{v}_h \in V_{0,h}^{\text{wc}}$ yields

$$\begin{aligned} \langle \ell, \mathbf{v}_h \rangle &= a_h(\mathbf{u}, \mathbf{v}_h) - \sum_K \sum_{F \in \mathcal{F}_K \setminus \partial\Omega_N} \left(\boldsymbol{\sigma}_K \mathbf{n}_K, \mathbf{v}_K \right)_{0,F} \\ &= a_h(\mathbf{u}, \mathbf{v}_h) - \sum_{F \in \mathcal{F}_h \setminus \partial\Omega_N} \left(\boldsymbol{\sigma}, \llbracket \mathbf{v}_h \rrbracket_F \right)_{0,F}. \end{aligned}$$

Inserting the face projections $\hat{\Pi}_F^{\text{wc}} \boldsymbol{\lambda}_K \in M_F$ for $\boldsymbol{\lambda}_K = \boldsymbol{\sigma}_K \mathbf{n}_K \in L_2(\partial K; \mathbb{R}^{\dim})$ gives

$$\begin{aligned} \sum_K \sum_{F \in \mathcal{F}_K \setminus \partial\Omega_N} \left(\hat{\Pi}_F^{\text{wc}} \boldsymbol{\lambda}_K, \mathbf{v}_K \right)_{0,F} &= \sum_K \left(\sum_{F \in \mathcal{F}_K \setminus \partial\Omega} \left(\hat{\Pi}_F^{\text{wc}} \boldsymbol{\lambda}_K, \mathbf{v}_K \right)_{0,F} + \sum_{F \in \mathcal{F}_K \cap \partial\Omega_D} \left(\hat{\Pi}_F^{\text{wc}} \boldsymbol{\lambda}_K, \mathbf{v}_K \right)_{0,F} \right) \\ &= \frac{1}{2} \sum_K \sum_{F \in \mathcal{F}_K \setminus \partial\Omega} \left(\hat{\Pi}_F^{\text{wc}} \boldsymbol{\lambda}_K, \llbracket \mathbf{v}_h \rrbracket_F \mathbf{n}_K \right)_{0,F} = 0 \end{aligned}$$

using $\boldsymbol{\lambda}_K = -\boldsymbol{\lambda}_{K_F}$ on inner faces and the weak boundary conditions in $V_{0,h}^{\text{wc}}$, so that we obtain

$$\begin{aligned} \sum_K \sum_{F \in \mathcal{F}_K \setminus \partial\Omega_N} \left(\boldsymbol{\lambda}_K, \mathbf{v}_K \right)_{0,F} &= \sum_K \sum_{F \in \mathcal{F}_K \setminus \partial\Omega_N} \left(\boldsymbol{\lambda}_K - \hat{\Pi}_F^{\text{wc}} \boldsymbol{\lambda}_K, \mathbf{v}_K \right)_{0,F} \\ &= \sum_K \sum_{F \in \mathcal{F}_K \setminus \partial\Omega_N} \left(\boldsymbol{\lambda}_K - \hat{\Pi}_F^{\text{wc}} \boldsymbol{\lambda}_K, \mathbf{v}_K - \hat{\Pi}_F^{\text{wc}} \mathbf{v}_h \right)_{0,F} \\ &\leq \left\| \boldsymbol{\lambda} - \hat{\Pi}_h^{\text{wc}} \boldsymbol{\lambda} \right\|_{-\frac{1}{2}, \partial\Omega_h} \left\| \mathbf{v}_h - \hat{\Pi}_h^{\text{wc}} \mathbf{v}_h \right\|_{\frac{1}{2}, \partial\Omega_h} \quad (5.3) \end{aligned}$$

with $\boldsymbol{\lambda} = \left(\boldsymbol{\lambda}_K \right)_{K \in \mathcal{K}_h}$ and $\hat{\Pi}_h^{\text{wc}} \mathbf{v} = \left(\hat{\Pi}_F^{\text{wc}} \mathbf{v}_F \right)_{F \in \mathcal{F}_h \setminus \partial\Omega_N}$.

Inserting (5.1) and (5.2) we obtain for all $\mathbf{w}_h \in V_h^{\text{wc}}(\mathbf{u}_D)$

$$\begin{aligned} a_h(\mathbf{u}_h^{\text{wc}} - \mathbf{w}_h, \mathbf{v}_h) &= \langle \ell, \mathbf{v}_h \rangle - a_h(\mathbf{w}_h, \mathbf{v}_h) \\ &= a_h(\mathbf{u} - \mathbf{w}_h, \mathbf{v}_h) - \sum_K \sum_{F \in \mathcal{F}_K \setminus \partial\Omega_N} \left(\boldsymbol{\lambda}_K, \mathbf{v}_K \right)_{0,F} \\ &\leq \left| \mathbf{u} - \mathbf{w}_h \right|_{E, \Omega_h} \left| \mathbf{v}_h \right|_{E, \Omega_h} + \left\| \boldsymbol{\lambda} - \hat{\Pi}_h^{\text{wc}} \boldsymbol{\lambda} \right\|_{-\frac{1}{2}, \partial\Omega_h} C_0 \left| \mathbf{v}_h \right|_{1, \Omega_h} \end{aligned}$$

and thus

$$\begin{aligned} \left| \mathbf{u}_h^{\text{wc}} - \mathbf{w}_h \right|_{E, \Omega_h} &= \sup_{\mathbf{v}_h \in V_h^{\text{wc}} \setminus \{0\}} \frac{a_h(\mathbf{u}_h^{\text{wc}} - \mathbf{w}_h, \mathbf{v}_h)}{\left| \mathbf{v}_h \right|_{E, \Omega_h}} \\ &\leq \left| \mathbf{u} - \mathbf{w}_h \right|_{E, \Omega_h} + C_0 \hat{C}_K \left\| \mathbb{C}^{-\frac{1}{2}} \right\|_{\infty, \Omega} \left\| \boldsymbol{\lambda} - \hat{\Pi}_h^{\text{wc}} \boldsymbol{\lambda} \right\|_{-\frac{1}{2}, \partial\Omega_h}. \end{aligned}$$

The assertion now follows from $\left| \mathbf{u} - \mathbf{u}_h^{\text{wc}} \right|_{E, \Omega_h} \leq \left| \mathbf{u} - \mathbf{w}_h \right|_{E, \Omega_h} + \left| \mathbf{u}_h^{\text{wc}} - \mathbf{w}_h \right|_{E, \Omega_h}$ and $\left\| \boldsymbol{\lambda}_F - \hat{\Pi}_F^{\text{wc}} \boldsymbol{\lambda}_F \right\|_{0,F} \leq \inf_{\boldsymbol{\mu}_F \in M_F} \left\| \boldsymbol{\lambda}_F - \boldsymbol{\mu}_F \right\|_{0,F}$. \square

In the next step, we derive an *a posteriori* error bound. We define for the discontinuous stress approximation $\boldsymbol{\sigma}_h^{\text{wc}} = \mathbb{C}\boldsymbol{\varepsilon}(\mathbf{u}_h^{\text{wc}})$ the jump term $[[\boldsymbol{\sigma}_h^{\text{wc}}]]_F = \boldsymbol{\sigma}_{K_F}^{\text{wc}} - \boldsymbol{\sigma}_K^{\text{wc}}$ on inner faces $F \in \mathcal{F}_h \cap \Omega$, and

$$\begin{aligned}\eta_{\text{vol},K} &= h_K \left\| \operatorname{div} \boldsymbol{\sigma}_h^{\text{wc}} + \mathbf{f}_h \right\|_{0,K}, \\ \eta_{\text{dual},K} &= \left(\frac{1}{2} \sum_{F \in \mathcal{F}_K \cap \Omega} h_K \left\| [[\boldsymbol{\sigma}_h^{\text{wc}}]]_F \mathbf{n}_F \right\|_{0,F}^2 + \sum_{F \in \mathcal{F}_K \cap \partial\Omega_N} h_K \left\| \boldsymbol{\sigma}_h^{\text{wc}} \mathbf{n} - \mathbf{t}_{N,h} \right\|_{0,F}^2 \right)^{\frac{1}{2}}, \\ \eta_{\text{primal},K} &= \left(\frac{1}{2} \sum_{F \in \mathcal{F}_K \cap \Omega} h_K^{-1} \left\| [[\mathbf{u}_h]]_F \right\|_{0,F}^2 + \sum_{F \in \mathcal{F}_K \cap \partial\Omega_D} h_K^{-1} \left\| \mathbf{u}_h^{\text{wc}} - \mathbf{u}_{D,h} \right\|_{0,F}^2 \right)^{\frac{1}{2}}, \\ \eta_K &= \left(\eta_{\text{vol},K}^2 + \mu^{-1} \eta_{\text{dual},K}^2 + \mu \eta_{\text{primal},K}^2 \right)^{\frac{1}{2}}\end{aligned}$$

depending on approximations \mathbf{f}_h , $\mathbf{u}_{D,h}$ and $\mathbf{t}_{N,h}$ of the data.

Lemma 8. *Assume that the Dirichlet data $\mathbf{u}_D = \mathbf{u}_{D,h}$ are piecewise polynomials with $\mathbf{u}_{D,F} \in \mathbb{P}_k(F; \mathbb{R}^{\dim})$ on $F \in \mathcal{F}_h \cap \partial\Omega_D$ for some $k \in \mathbb{N}$ such that $\mathbb{P}_k(\Omega_h; \mathbb{R}^{\dim}) \cap H^1(F; \mathbb{R}^{\dim}) \subset V_h^{\text{wc}}$, and assume that traction and body forces can be evaluated exactly, i.e., $\mathbf{t}_N = \mathbf{t}_{N,h}$ and $\mathbf{f} = \mathbf{f}_h$.*

Then, the residual estimator η_K is reliable, i.e., a constant $C > 0$ exists such that the error is bounded by

$$\left| \mathbf{u} - \mathbf{u}_h^{\text{wc}} \right|_{\mathbb{E}, \Omega_h} \leq C \left(\sum_K \eta_K^2 \right)^{\frac{1}{2}}.$$

Proof. The proof for this lemma is taken from [44].

We combine an estimate for the conforming part using Galerkin orthogonality with an estimate for the relaxed conformity. Therefore, let $\mathbf{u}^* \in V(\mathbf{u}_D)$ be a conforming reconstruction of the discrete solution defined by

$$a(\mathbf{u}^*, \mathbf{v}) = a_h(\mathbf{u}_h^{\text{wc}}, \mathbf{v}), \quad \mathbf{v} \in V(\mathbf{0}).$$

Then, the error

$$\begin{aligned}\left| \mathbf{u} - \mathbf{u}_h^{\text{wc}} \right|_{\mathbb{E}, \Omega_h}^2 &= a_h(\mathbf{u} - \mathbf{u}_h^{\text{wc}}, \mathbf{u} - \mathbf{u}_h^{\text{wc}}) \\ &= a_h(\mathbf{u} - \mathbf{u}_h^{\text{wc}}, \mathbf{u} - \mathbf{u}^*) + a_h(\mathbf{u} - \mathbf{u}_h^{\text{wc}}, \mathbf{u}^* - \mathbf{u}_h^{\text{wc}})\end{aligned}\quad (5.4)$$

is estimated separately for the approximation and the consistency error in (i) and (ii).

(i) For the estimate of the the approximation error, we observe for $\mathbf{e}^* = \mathbf{u} - \mathbf{u}^* \in V(\mathbf{0})$

$$|\mathbf{e}^*|_{\mathbf{E},\Omega}^2 = a(\mathbf{u} - \mathbf{u}^*, \mathbf{e}^*) = a_h(\mathbf{u} - \mathbf{u}_h^{\text{wc}}, \mathbf{e}^*) \leq |\mathbf{u} - \mathbf{u}_h^{\text{wc}}|_{\mathbf{E},\Omega_h} |\mathbf{e}^*|_{\mathbf{E},\Omega}, \quad (5.5)$$

i.e., $|\mathbf{e}^*|_{\mathbf{E},\Omega} \leq |\mathbf{u} - \mathbf{u}_h^{\text{wc}}|_{\mathbf{E},\Omega_h}$. We insert a Scott-Zhang quasi-interpolation $\Pi_h^{\text{SZ}} \mathbf{e}^* \in V_{0,h}^{\text{cf}}$ to lowest order conforming finite elements [12, Def. 4.10] satisfying

$$\left(\sum_K \left(h_K^{-2} \|\mathbf{e}^* - \Pi_h^{\text{SZ}} \mathbf{e}^*\|_{0,K}^2 + \sum_{F \in \mathcal{F}_K \setminus \partial\Omega_D} h_K^{-1} \|\mathbf{e}^* - \Pi_h^{\text{SZ}} \mathbf{e}^*\|_{0,F}^2 \right) \right)^{\frac{1}{2}} \leq C_1 \|\mathbf{e}^*\|_{1,\Omega} \quad (5.6)$$

with a constant $C_1 > 0$ only depending on the mesh regularity [12, Thm. 4.6]. We have $\Pi_h^{\text{SZ}} \mathbf{e}^* \in V(\mathbf{0}) \cap V_h^{\text{wc}}$, and using Galerkin orthogonality in (3.1) and

(3.8), we obtain

$$\begin{aligned}
a_h(\mathbf{u} - \mathbf{u}_h^{\text{wc}}, \mathbf{e}^*) &= \left(\boldsymbol{\sigma} - \boldsymbol{\sigma}_h^{\text{wc}}, \boldsymbol{\varepsilon}(\mathbf{e}^* - \Pi_h^{\text{SZ}} \mathbf{e}^*) \right)_{0, \Omega_h} \\
&= \left(\operatorname{div} \boldsymbol{\sigma}_h^{\text{wc}} + \operatorname{div} \boldsymbol{\sigma}, \mathbf{e}^* - \Pi_h^{\text{SZ}} \mathbf{e}^* \right)_{0, \Omega_h} \\
&\quad + \left(\mathbf{g}_{\text{N},h}, \mathbf{e}^* - \Pi_h^{\text{SZ}} \mathbf{e}^* \right)_{0, \partial \Omega_{\text{N}}} - \sum_K \left(\boldsymbol{\sigma}_h^{\text{wc}} \mathbf{n}_K, \mathbf{e}^* - \Pi_h^{\text{SZ}} \mathbf{e}^* \right)_{0, \partial K} \\
&= \left(\operatorname{div} \boldsymbol{\sigma}_h^{\text{wc}} + \mathbf{f}_h, \mathbf{e}^* - \Pi_h^{\text{SZ}} \mathbf{e}^* \right)_{0, \Omega_h} \\
&\quad + \left(\mathbf{g}_{\text{N},h} - \boldsymbol{\sigma}_h^{\text{wc}} \mathbf{n}, \mathbf{e}^* - \Pi_h^{\text{SZ}} \mathbf{e}^* \right)_{0, \partial \Omega_{\text{N}}} - \sum_{F \in \mathcal{F}_h \cap \Omega} \left(\llbracket \boldsymbol{\sigma}_h^{\text{wc}} \rrbracket_F \mathbf{n}_F, \mathbf{e}^* - \Pi_h^{\text{SZ}} \mathbf{e}^* \right)_{0, F} \\
&\leq \sum_K \left(\left\| \operatorname{div} \boldsymbol{\sigma}_h^{\text{wc}} + \mathbf{f}_h \right\|_{0, K} \left\| \mathbf{e}^* - \Pi_h^{\text{SZ}} \mathbf{e}^* \right\|_{0, K} \right. \\
&\quad + \frac{1}{2} \sum_{F \in \mathcal{F}_K \cap \Omega} \left\| \llbracket \boldsymbol{\sigma}_h^{\text{wc}} \rrbracket_F \mathbf{n}_F \right\|_{0, F} \left\| \mathbf{e}^* - \Pi_h^{\text{SZ}} \mathbf{e}^* \right\|_{0, F} \\
&\quad \left. + \sum_{F \in \mathcal{F}_K \cap \partial \Omega_{\text{N}}} \left\| \boldsymbol{\sigma}_h^{\text{wc}} \mathbf{n} - \mathbf{g}_{\text{N},h} \right\|_{0, F} \left\| \mathbf{e}^* - \Pi_h^{\text{SZ}} \mathbf{e}^* \right\|_{0, F} \right) \\
&\leq \left(\sum_K \left(\eta_{\text{vol}, K}^2 + \eta_{\text{dual}, K}^2 \right) \right)^{\frac{1}{2}} \\
&\quad \cdot \left(\sum_K \left(h_K^{-2} \left\| \mathbf{e}^* - \Pi_h^{\text{SZ}} \mathbf{e}^* \right\|_{0, K}^2 + \sum_{F \in \mathcal{F}_K \setminus \partial \Omega_{\text{D}}} h_K^{-1} \left\| \mathbf{e}^* - \Pi_h^{\text{SZ}} \mathbf{e}^* \right\|_{0, F}^2 \right) \right)^{\frac{1}{2}} \\
&\leq \left(\sum_K \left(\eta_{\text{vol}, K}^2 + \eta_{\text{dual}, K}^2 \right) \right)^{\frac{1}{2}} C_1 \left\| \mathbf{e}^* \right\|_{1, \Omega} \\
&\leq C_1 \mu^{-\frac{1}{2}} \left(\sum_K \left(\eta_{\text{vol}, K}^2 + \eta_{\text{dual}, K}^2 \right) \right)^{\frac{1}{2}} \left| \mathbf{u} - \mathbf{u}_h^{\text{wc}} \right|_{\text{E}, \Omega_h}
\end{aligned}$$

using the estimate (5.6) and $\left\| \mathbf{e}^* \right\|_{1, \Omega} \leq \left\| \mathbb{C}^{-\frac{1}{2}} \right\|_{\infty, \Omega} \left| \mathbf{e}^* \right|_{\text{E}, \Omega_h} \leq \mu^{-\frac{1}{2}} \left| \mathbf{e}^* \right|_{\text{E}, \Omega_h}$.

(ii) For the estimate of the consistency error in (5.4) we construct a conforming interpolation \mathbf{u}_h^* of the weakly conforming approximation \mathbf{u}_h^{wc} . We select V_h^{dG} such that $\mathbb{P}_k(\Omega_h; \mathbb{R}^{\text{dim}}) \subset V_h^{\text{dG}}$ and $V_h^{\text{cf}} = V_h^{\text{dG}} \cap \mathbf{H}^1(\Omega; \mathbb{R}^{\text{dim}}) \subset V_h^{\text{wc}}$. Let $\boldsymbol{\phi}_{z,j}^{\text{cf}} \in V_h^{\text{cf}}$ be the nodal basis with nodal points $z \in \mathcal{Z}_h \subset \bar{\Omega}$ and $j = 1, \dots, \text{dim}$, and let $\boldsymbol{\phi}_{K,z,j}^{\text{dG}} \in V_h^{\text{dG}}$ be the corresponding discontinuous nodal basis with nodal points $z \in \mathcal{Z}_K \subset \bar{K}$. Then, for $\mathbf{u}_h^{\text{wc}} \in V_h^{\text{wc}}(\mathbf{u}_{\text{D},h})$ with

$$\mathbf{u}_K^{\text{wc}} = \sum_{z \in \mathcal{Z}_K} \sum_{j=1}^{\text{dim}} u_{K,j}^{\text{wc}}(z) \boldsymbol{\phi}_{K,z,j}^{\text{dG}}, \quad \mathbf{u}_K^{\text{wc}} = \left(u_{K,j}^{\text{wc}} \right)_{j=1, \dots, \text{dim}}, \quad K \in \mathcal{K}_h$$

a conforming interpolation $\mathbf{u}_h^* \in V_h^{\text{cf}}(\mathbf{u}_{\text{D},h})$ is defined by

$$\mathbf{u}_h^* = \sum_{z \in \mathcal{Z}_h} \sum_{j=1}^{\dim} u_{h,j}^*(z) \phi_{z,j}^{\text{cf}}, \quad \mathbf{u}_h^* = (u_{h,j}^*)_{j=1, \dots, \dim}$$

with

$$\mathbf{u}_h^*(z) = \begin{cases} \mathbf{u}_K^{\text{wc}}(z) & z \in \mathcal{Z}_h \setminus \partial\Omega_{\text{D}} \text{ and } |\mathcal{K}_z| = 1, \\ \mathbf{u}_{\text{D},h}(z) & z \in \mathcal{Z}_h \cap \partial\Omega_{\text{D}}, \\ \frac{1}{|\mathcal{F}_z|} \sum_{F \in \mathcal{F}_z} \frac{1}{2} \left(\mathbf{u}_K^{\text{wc}}(z) + \mathbf{u}_{K_F}^{\text{wc}}(z) \right) & z \in \mathcal{Z}_h \setminus \partial\Omega_{\text{D}} \text{ and } |\mathcal{K}_z| > 1, \end{cases}$$

where $\mathcal{F}_z = \{F \in \mathcal{F}_h \setminus \partial\Omega : z \in \mathcal{Z}_F\}$, $\mathcal{Z}_F = \mathcal{Z}_h \cap \bar{F}$, and $\mathcal{K}_z = \{K \in \mathcal{K}_h : z \in \mathcal{Z}_K\}$.

Now we use the local estimates

$$\begin{aligned} \|\mathbf{v}_K\|_{1,K} &\leq C_{1,K} h_K^{-1} \|\mathbf{v}_K\|_{0,K}, & \mathbf{v}_K \in V_K, \\ \|\mathbf{v}_K\|_{0,K}^2 &\leq C_{2,K} h_K^{\dim} \sum_{z \in \mathcal{Z}_K} |\mathbf{v}_K(z)|^2, & \mathbf{v}_K \in V_K, \\ \sum_{z \in \mathcal{Z}_F} |\mathbf{v}_K(z)|^2 &\leq C_F h_K^{1-\dim} \|\mathbf{v}_K\|_{0,F}^2, & \mathbf{v}_K \in V_K, F \in \mathcal{F}_K \end{aligned}$$

with constants $C_{1,K}, C_{2,K}, C_F$ only depending on the mesh regularity and the polynomial degree in V_K . This gives

$$\begin{aligned} \|\mathbf{u}_h^{\text{wc}} - \mathbf{u}_h^*\|_{1,\Omega_h}^2 &\leq C_1 \sum_K h_K^{-2} \|\mathbf{u}_K^{\text{wc}} - \mathbf{u}_h^*\|_{0,K}^2 \\ &\leq C_2 \sum_K h_K^{\dim-2} \sum_{z \in \mathcal{Z}_K} |\mathbf{u}_K^{\text{wc}}(z) - \mathbf{u}_h^*(z)|^2 \\ &= C_2 \sum_K h_K^{\dim-2} \left(\sum_{z \in \mathcal{Z}_K \setminus \partial\Omega_{\text{D}}, |\mathcal{K}_z| > 1} \left| \mathbf{u}_K^{\text{wc}}(z) - \frac{1}{|\mathcal{F}_z|} \sum_{F \in \mathcal{F}_z} \frac{1}{2} \left(\mathbf{u}_K^{\text{wc}}(z) + \mathbf{u}_{K_F}^{\text{wc}}(z) \right) \right|^2 \right. \\ &\quad \left. + \sum_{z \in \mathcal{Z}_K \cap \partial\Omega_{\text{D}}} \left| \mathbf{u}_K^{\text{wc}}(z) - \mathbf{u}_{\text{D},h}(z) \right|^2 \right) \\ &\leq C_3 \sum_K h_K^{\dim-2} \left(\sum_{z \in \mathcal{Z}_K \setminus \partial\Omega_{\text{D}}, |\mathcal{K}_z| > 1} \left| \mathbf{u}_K^{\text{wc}}(z) - \mathbf{u}_{K_F}^{\text{wc}}(z) \right|^2 + \sum_{z \in \mathcal{Z}_K \cap \partial\Omega_{\text{D}}} \left| \mathbf{u}_K^{\text{wc}}(z) - \mathbf{u}_{\text{D},h}(z) \right|^2 \right) \\ &\leq C_4 \sum_K h_K^{-1} \left(\frac{1}{2} \sum_{F \in \mathcal{F}_K \cap \Omega} \|\llbracket \mathbf{u}_h^{\text{wc}} \rrbracket_F\|_{0,F}^2 + \sum_{F \in \mathcal{F}_K \cap \partial\Omega_{\text{D}}} \|\mathbf{u}_K^{\text{wc}} - \mathbf{u}_{\text{D},h}\|_{0,F}^2 \right) \\ &= C_4 \sum_K \eta_{\text{primal},K}^2 \end{aligned} \tag{5.7}$$

with constants C_1, C_2, C_3, C_4 depending on the mesh regularity and the polynomial degree in V_h^{dG} .

We observe for the conforming reconstruction \mathbf{u}^*

$$\begin{aligned} 0 &= a(\mathbf{u}^*, \mathbf{v}) - a_h(\mathbf{u}_h^{\text{wc}}, \mathbf{v}) \\ &= \left(\mathbb{C}_0 \boldsymbol{\varepsilon}(\mathbf{u}^* - \mathbf{u}_h^{\text{wc}}), \boldsymbol{\varepsilon}(\mathbf{v}) \right)_{0, \Omega_h} + \dim \lambda \left(\operatorname{div}(\mathbf{u}^* - \mathbf{u}_h^{\text{wc}}), \operatorname{div}(\mathbf{v}) \right)_{0, \Omega_h}, \quad \mathbf{v} \in V(\mathbf{0}). \end{aligned}$$

Now we select $\mathbf{v} \in V(\mathbf{0})$ such that $\operatorname{div} \mathbf{v} = \operatorname{div}(\mathbf{u}^* - \mathbf{u}_h^{\text{wc}})$ and

$$\|\mathbf{v}\|_{1, \Omega} \leq C_5 \|\operatorname{div}(\mathbf{u}^* - \mathbf{u}_h^{\text{wc}})\|_{0, \Omega_h}$$

with a constant $C_5 > 0$ depending on the domain and $\partial\Omega_D$. Together, this yields for this choice of \mathbf{v}

$$\begin{aligned} \dim \lambda \left\| \operatorname{div}(\mathbf{u}^* - \mathbf{u}_h^{\text{wc}}) \right\|_{0, \Omega_h}^2 &= \left(\mathbb{C}_0 \boldsymbol{\varepsilon}(\mathbf{u}^* - \mathbf{u}_h^{\text{wc}}), \boldsymbol{\varepsilon}(\mathbf{v}) \right)_{0, \Omega_h} \\ &\leq 2\mu \left\| \boldsymbol{\varepsilon}(\mathbf{u}^* - \mathbf{u}_h^{\text{wc}}) \right\|_{0, \Omega_h} \|\mathbf{v}\|_{1, \Omega_h} \\ &\leq 2\mu C_5 \left\| \boldsymbol{\varepsilon}(\mathbf{u}^* - \mathbf{u}_h^{\text{wc}}) \right\|_{0, \Omega_h} \left\| \operatorname{div}(\mathbf{u}^* - \mathbf{u}_h^{\text{wc}}) \right\|_{0, \Omega_h} \end{aligned}$$

and thus

$$\dim \lambda \left\| \operatorname{div}(\mathbf{u}^* - \mathbf{u}_h^{\text{wc}}) \right\|_{0, \Omega_h} \leq 2\mu C_6 \left\| \boldsymbol{\varepsilon}(\mathbf{u}^* - \mathbf{u}_h^{\text{wc}}) \right\|_{0, \Omega_h}. \quad (5.8)$$

Now we define $\mathbf{u}^{**} \in V(\mathbf{u}_D)$ solving

$$\left(\boldsymbol{\varepsilon}(\mathbf{u}^{**}), \boldsymbol{\varepsilon}(\mathbf{v}) \right)_{0, \Omega} = \left(\boldsymbol{\varepsilon}(\mathbf{u}_h^{\text{wc}}), \boldsymbol{\varepsilon}(\mathbf{v}) \right)_{0, \Omega_h}, \quad \mathbf{v} \in V(\mathbf{0}).$$

We have for consistent Dirichlet data $\mathbf{v} = \mathbf{u}^{**} - \mathbf{u}_h^* \in V(\mathbf{0})$, and we obtain

$$\begin{aligned} \left\| \boldsymbol{\varepsilon}(\mathbf{u}^{**} - \mathbf{u}_h^{\text{wc}}) \right\|_{0, \Omega_h}^2 &= \left(\boldsymbol{\varepsilon}(\mathbf{u}^{**} - \mathbf{u}_h^{\text{wc}}), \boldsymbol{\varepsilon}(\mathbf{u}^{**} - \mathbf{u}_h^{\text{wc}}) \right)_{0, \Omega_h} \\ &= \left(\boldsymbol{\varepsilon}(\mathbf{u}^{**} - \mathbf{u}_h^{\text{wc}}), \boldsymbol{\varepsilon}(\mathbf{u}^{**}) \right)_{0, \Omega_h} - \left(\boldsymbol{\varepsilon}(\mathbf{u}^{**} - \mathbf{u}_h^{\text{wc}}), \boldsymbol{\varepsilon}(\mathbf{u}_h^{\text{wc}}) \right)_{0, \Omega_h} \\ &= \left(\boldsymbol{\varepsilon}(\mathbf{u}^{**} - \mathbf{u}_h^{\text{wc}}), \boldsymbol{\varepsilon}(\mathbf{u}_h^*) \right)_{0, \Omega_h} - \left(\boldsymbol{\varepsilon}(\mathbf{u}^{**} - \mathbf{u}_h^{\text{wc}}), \boldsymbol{\varepsilon}(\mathbf{u}_h^{\text{wc}}) \right)_{0, \Omega_h} \\ &= \left(\boldsymbol{\varepsilon}(\mathbf{u}^{**} - \mathbf{u}_h^{\text{wc}}), \boldsymbol{\varepsilon}(\mathbf{u}_h^* - \mathbf{u}_h^{\text{wc}}) \right)_{0, \Omega_h} \\ &\leq \left\| \boldsymbol{\varepsilon}(\mathbf{u}^{**} - \mathbf{u}_h^{\text{wc}}) \right\|_{0, \Omega_h} \left\| \boldsymbol{\varepsilon}(\mathbf{u}_h^* - \mathbf{u}_h^{\text{wc}}) \right\|_{0, \Omega_h}, \end{aligned}$$

so that $\|\boldsymbol{\varepsilon}(\mathbf{u}^{**} - \mathbf{u}_h^{\text{wc}})\|_{0,\Omega_h} \leq \|\boldsymbol{\varepsilon}(\mathbf{u}_h^* - \mathbf{u}_h^{\text{wc}})\|_{0,\Omega_h}$. Then, using (5.8), we obtain

$$\begin{aligned}
|\mathbf{u}^* - \mathbf{u}_h^{\text{wc}}|_{\mathbf{E},\Omega_h}^2 &= a(\mathbf{u}^*, \mathbf{u}^*) - a_h(\mathbf{u}_h^{\text{wc}}, \mathbf{u}^*) - a_h(\mathbf{u}^* - \mathbf{u}_h^{\text{wc}}, \mathbf{u}_h^{\text{wc}}) \\
&= a(\mathbf{u}^*, \mathbf{u}^{**}) - a_h(\mathbf{u}_h^{\text{wc}}, \mathbf{u}^{**}) - a_h(\mathbf{u}^* - \mathbf{u}_h^{\text{wc}}, \mathbf{u}_h^{\text{wc}}) \\
&= a_h(\mathbf{u}^* - \mathbf{u}_h^{\text{wc}}, \mathbf{u}^{**} - \mathbf{u}_h^{\text{wc}}) \\
&= 2\mu \left(\boldsymbol{\varepsilon}(\mathbf{u}^* - \mathbf{u}_h^{\text{wc}}), \boldsymbol{\varepsilon}(\mathbf{u}^{**} - \mathbf{u}_h^{\text{wc}}) \right)_{0,\Omega_h} \\
&\quad + \dim\lambda \left(\operatorname{div}(\mathbf{u}^* - \mathbf{u}_h^{\text{wc}}), \operatorname{div}(\mathbf{u}^{**} - \mathbf{u}_h^{\text{wc}}) \right)_{0,\Omega_h} \\
&\leq 2\mu \|\boldsymbol{\varepsilon}(\mathbf{u}^* - \mathbf{u}_h^{\text{wc}})\|_{0,\Omega_h} \|\boldsymbol{\varepsilon}(\mathbf{u}^{**} - \mathbf{u}_h^{\text{wc}})\|_{0,\Omega_h} \\
&\quad + \dim\lambda \|\operatorname{div}(\mathbf{u}^* - \mathbf{u}_h^{\text{wc}})\|_{0,\Omega_h} \|\operatorname{div}(\mathbf{u}^{**} - \mathbf{u}_h^{\text{wc}})\|_{0,\Omega_h} \\
&\leq 2\mu(1 + C_5) \|\boldsymbol{\varepsilon}(\mathbf{u}^* - \mathbf{u}_h^{\text{wc}})\|_{0,\Omega_h} \|\boldsymbol{\varepsilon}(\mathbf{u}^{**} - \mathbf{u}_h^{\text{wc}})\|_{0,\Omega_h} \\
&\leq 2\mu(1 + C_5) \|\mathbb{C}^{-\frac{1}{2}}\|_{\infty,\Omega} |\mathbf{u}^* - \mathbf{u}_h^{\text{wc}}|_{\mathbf{E},\Omega_h} \|\boldsymbol{\varepsilon}(\mathbf{u}^* - \mathbf{u}_h^{\text{wc}})\|_{0,\Omega_h},
\end{aligned}$$

so that the assertion is obtained together with (5.7), i.e.,

$$|\mathbf{u}^* - \mathbf{u}_h^{\text{wc}}|_{\mathbf{E},\Omega_h} \leq 2\mu^{\frac{1}{2}}(1 + C_5) \|\boldsymbol{\varepsilon}(\mathbf{u}_h^* - \mathbf{u}_h^{\text{wc}})\|_{0,\Omega_h} \leq 2\mu^{\frac{1}{2}}(1 + C_5) C_4 \left(\sum_K \eta_{\text{primal},K}^2 \right)^{\frac{1}{2}}.$$

□

Here, the constant C depends on the mesh, on μ , and on the polynomial degree k which is required to represent the Dirichlet data. In the general case of non-polynomial data, an error bound can be achieved with a saturation assumption or an additional term depending on oscillations for sufficiently smooth data; this is discussed, e.g., in [37] for the Poisson equation.

For conforming discretizations, the finite element error can be bounded by $\eta_{\text{vol},K}$ and $\eta_{\text{dual},K}$. The additional term $\eta_{\text{primal},K}$ is required for residual estimators for nonconforming approximations, see, e.g., [4, 22, 28] for the Poisson equation, [38] for the Stokes equations, and [47, 11] for linear elasticity.

For the practical use of the error estimator for p -refinement of individual faces, we define

$$\eta_{\text{dual},F} = \begin{cases} \frac{1}{2} h_K^{\frac{1}{2}} \|\llbracket \boldsymbol{\sigma}_h^{\text{wc}} \rrbracket_F \mathbf{n}_F\|_{0,F} & F \in \mathcal{F}_K \cap \Omega \\ h_K^{\frac{1}{2}} \|\boldsymbol{\sigma}_h^{\text{wc}} \mathbf{n} - \mathbf{t}_{\text{N},h}\|_{0,F} & F \in \mathcal{F}_K \cap \partial\Omega_{\text{N}} \end{cases}$$

$$\eta_{\text{primal},F} = \begin{cases} \frac{1}{2} h_K^{-\frac{1}{2}} \|\llbracket \mathbf{u}_h \rrbracket_F\|_{0,F} & F \in \mathcal{F}_K \cap \Omega \\ h_K^{-\frac{1}{2}} \|\mathbf{u}_h^{\text{wc}} - \mathbf{u}_{\text{D},h}\|_{0,F} & F \in \mathcal{F}_K \cap \partial\Omega_{\text{D}} \end{cases}$$

Obviously it holds, that $\sum_{K \in \mathcal{K}_h} \eta_{\text{primal},K}^2 = \sum_{F \in \mathcal{F}_h} \eta_{\text{primal},F}^2$ and $\sum_{K \in \mathcal{K}_h} \eta_{\text{dual},K}^2 = \sum_{F \in \mathcal{F}_h} \eta_{\text{dual},F}^2$.

Since the volume term η_{vol} is depending linear on the mesh parameter h and the other terms only depend on \sqrt{h} , we omitted the volume term in our implementation, since it has no significant impact for small enough cells.

5.2 Adaptive algorithm

Large-scale problems create the need for efficient methods and one obvious way to increase the efficiency of a given method is to distribute the available computing power locally. This is especially necessary where we expect large stress magnitudes, for example at singularities, cf. Chapter 4.2 and Chapter 4.6. Since we want a fine discretization in the vicinity of singularities, but want to avoid unnecessary fineness in other parts of the domain, we use an adaptive scheme to distribute the ideal number of degrees of freedom over the domain. For the deployment of adaptive strategies for finite element methods, suitable sources are for example [5] and [51]. Our algorithm consists of the following steps:

1. **Generate coarse solution data.** In general, when we simulate the occurring displacements and stress in a mechanical part, we do not know where we need a fine mesh and where a coarse refinement is sufficient. For this reason we start by computing the problem on a coarse mesh to obtain the solution $\mathbf{u}_h^{\text{coarse}}$. This takes only a small fraction of time compared to a uniform mesh which would already resolve each area sufficiently.
2. **Evaluate error estimator.** In the next step we use the coarse solution $\mathbf{u}_h^{\text{coarse}}$ to compute $\eta_{\text{primal},F}$ and $\eta_{\text{dual},F}$, for every face $F \in \mathcal{F}_h$ and $\eta_{\text{primal},K}$ and $\eta_{\text{dual},K}$ for every cell $K \in \mathcal{K}_h$.
3. **Marking of entities to refine.** In the following we can choose between two types of refinement. To avoid conflicts caused by simultaneous cell and face refinements, we chose to implement the algorithm in such a

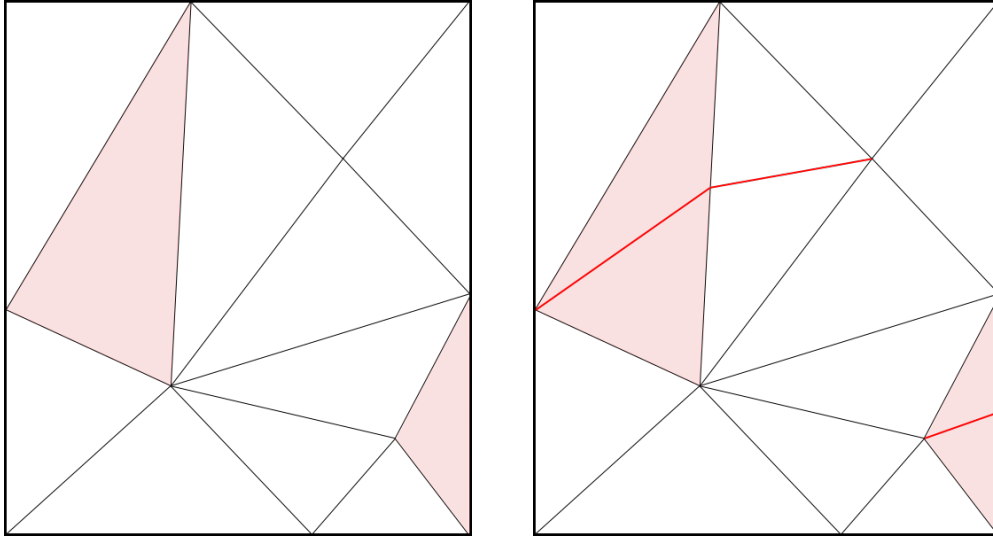


Figure 5.1: Red highlighted cells marked for h -refinement (left), marked cells after refinement, as well as one refined neighboring cell, to avoid a hanging node (right).

way, that we have in each adaptive loop either only h -refinement or only p -refinement.

- (a) **h -refinement** The cells $K \in \mathcal{K}_h$ are refined in a spatial sense, which means we divide the respective cells into smaller ones, this is called h -refinement. Since we want to avoid hanging nodes, we have to choose a strategy. In our case, we realized h -refinement only for triangles and we chose the strategy presented by Rosenberg and Stenger in [54]. When a triangular cell is marked for refinement, its longest side F_+ is split in half and two cells are created by dividing the triangle along the midpoint of F_+ and the opposing edge, cf. Fig. 5.1. The cell with which the marked cell shares the face F_+ is refined as well, to avoid hanging nodes. If there is no neighboring cell, only the marked one is refined. Note, that this is expendable to 3D by using tetrahedrons.
- (b) **p -refinement** We increase the ansatz-space of individual faces $F \in \mathcal{F}_h$ by adding more base-functions, this is called p -refinement. Since we increased the space M_F of all marked faces F , we need to check whether we need to increase the polynomial degree of V_K for each cell K with a refined face. For this we use a heuristic, where we

determine for each cell M_{Max,V_K} which is the maximum number of face degrees associated with cell K , which still guarantees a regular saddle point matrix, depending on the current polynomial degree of V_K . If $\sum_{F \in \mathcal{F}} M_F > M_{\text{Max},V_K}$, we increase the polynomial degree of V_K until this is no longer the case. If we do not increase V_K it is possible, that the local saddle point matrix becomes singular.

Depending on the choice we made, we mark either cells or faces by a Doerfler marking strategy, cf. [36]. We choose $0 < \Theta < 1$ and add cells or faces to the set \mathcal{M} until the condition

$$\Theta \sum_{n \in \mathcal{N}} \eta_n^2 \leq \sum_{m \in \mathcal{M}} \eta_m^2, \quad \mathcal{N} = \begin{cases} \mathcal{K}_h & \text{if } h\text{-refinement step} \\ \mathcal{F}_h & \text{if } p\text{-refinement step} \end{cases},$$

is fulfilled. We choose the set \mathcal{M} to be minimal, i.e. we mark the cells or faces with the highest error contribution first. Since we want to compute our problems highly parallelized, sorting the error estimation terms is not optimal. For this we use Algorithm 3, where we compute the value of a threshold τ to find a τ , such that $|\mathcal{N}_{h,al}| \cdot \Theta = \mathcal{M}_\tau$ with $\mathcal{M}_\tau = \{n \in \mathcal{N}_{h,al} : \eta_n^2 > \tau \eta_{\text{Max}}^2\}$. Here η_{Max}^2 is either $\max_F \eta_K^2$ in the case of h -refinement or $\max_F \eta_F^2$ in the case of p -refinement.

4. **Refinement of marked entities** Subsequently we refine the chosen entities.
5. **Generation of finer solution data** Afterwards we compute the problem on the new mesh and return to the estimation step. This process is repeated until a stopping criterion is satisfied.

An example of the resulting mesh after several p -adaptive refinement steps is depicted in Fig. 5.2. Here it can be clearly seen, that the algorithm marks and refines faces which are close to the known singularity and leaves faces untouched which are located towards the outward corners, where a small refinement is sufficient.

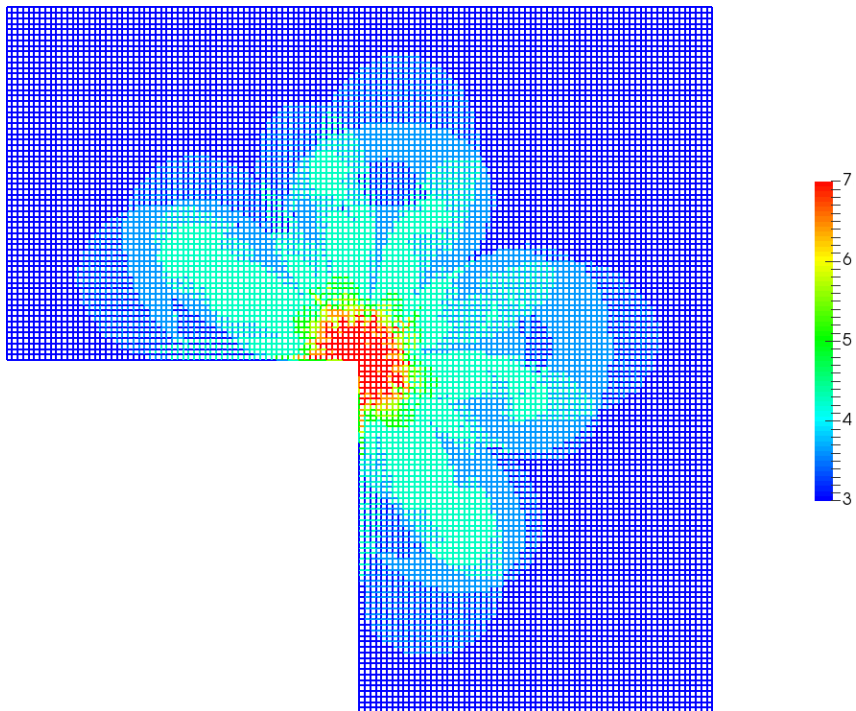


Figure 5.2: Number of degrees of freedom per face on a spatial uniform mesh of the L-shaped problem after several p -adaptive refinement steps.

Algorithm 2 Adaptive algorithm

```

1: Mesh  $\mathcal{M}_0$ ,  $al = 0$ 
2: Input:  $\Theta$ ,  $al_{\max}$ 
3: for  $al < al_{\max}$  do
4:   compute  $\mathbf{u}_{h,al}^{\text{wc}}$  on current mesh  $\mathcal{M}_{al}$ 
5:   decide if  $p$ - or  $h$ -refinement in current step
6:   for  $K \in \mathcal{K}_{h,al}$  do
7:     compute  $\eta_K^2$ ,  $\eta_{Max,K}^2 = \max_K \eta_K^2$ 
8:     if  $p$ -refinement then
9:       for  $F \in \mathcal{F}_K$  do
10:        compute  $\eta_F^2$ ,  $\eta_{Max,F}^2 = \max_F \eta_F^2$ 
11:       end for
12:     end if
13:   end for
14:   compute  $\tau_p, \tau_h$ , see Algorithm 3
15:   for  $K \in \mathcal{K}_h$  do
16:     if  $p$ -refinement then
17:       for  $F \in \mathcal{F}_K$  do
18:         if  $\eta_F^2 > \eta_{Max,F}^2 \cdot \tau_p$  then
19:           add ansatz function to  $F$ 
20:         end if
21:       end for
22:       if  $\sum_{F \in \mathcal{F}_K} M_F > M_{Max, V_K}$  then
23:         increase polynomial degree of  $V_K$ 
24:       end if
25:     else
26:       if  $\eta_K^2 > \eta_{Max,K}^2 \cdot \tau_h$  then
27:         refine cell  $K$ 
28:       end if
29:     end if
30:   end for
31:    $al = al + 1$ 
32:   if  $u_{al}$  fulfills convergence criteria then
33:     STOP
34:   end if
35: end for
36: Output:  $M_{al}$ ,  $\mathbf{u}_{h,al}^{\text{wc}}$ 

```

Algorithm 3 Determine threshold τ

1: **Input:** $\mathcal{N}_{h,al}$, η_n^2 for $n \in \mathcal{N}_{h,al}$, Θ
 2: $\tau = 0.5$
 3: $i = 1$
 4: $\eta_{\text{Max}}^2 = \begin{cases} \eta_{\text{Max},K}^2 & \text{if } h\text{-refinement} \\ \eta_{\text{Max},F}^2 & \text{if } p\text{-refinement} \end{cases}$
 5: $\mathcal{M}_\tau = \{n \in \mathcal{N}_{h,al} : \eta_n^2 > \tau \eta_{\text{Max}}^2\}$
 6: **while** $|\mathcal{N}_{h,al}| \cdot \Theta \neq \mathcal{M}_\tau$ **do**
 7: **if** $|\mathcal{N}_{h,al}| \cdot \Theta > \mathcal{M}_\tau$ **then**
 8: $\tau = \tau + 0.5^i$
 9: $i = i + 1$
 10: **end if**
 11: **if** $|\mathcal{N}_{h,al}| \cdot \Theta < \mathcal{M}_\tau$ **then**
 12: $\tau = \tau - 0.5^i$
 13: $i = i + 1$
 14: **end if**
 15: update \mathcal{M}_τ
 16: **end while**
 17: **Output:** τ

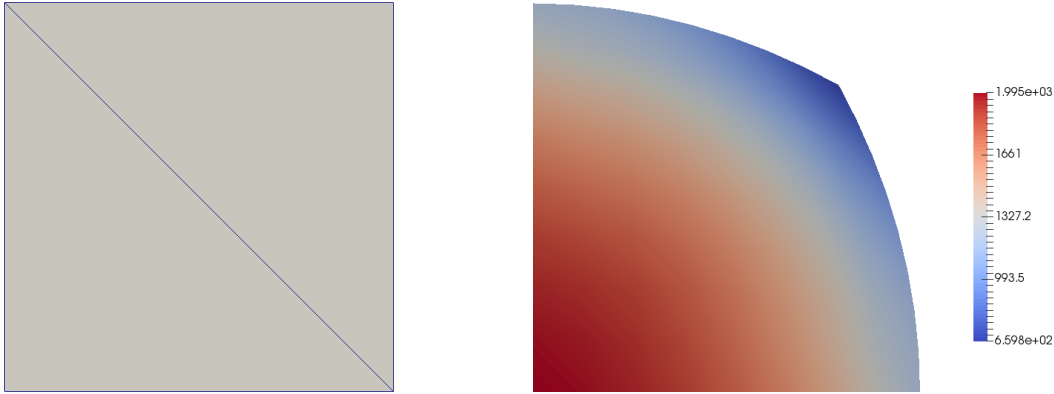


Figure 5.3: Unit square example: Domain with initial cells (left), distribution of $|\boldsymbol{\sigma}(\mathbf{u})|$ (right).

5.3 Example with known solution

In this section we provide a proof of concept for the presented adaptive algorithm. For this we compute the same example of Section 4.1 again, but this time on a different domain and using our h - and p -adaptive strategies. The exact solution remains the same and can be found in the aforementioned section, see equation (4.2). The new domain is the unit square, i.e. $\Omega = (0, 1)^2$. Since we need a triangular mesh for h -refinement, the domain is divided into two triangles, cf. Fig. 5.3. As a material we choose a linear elastic material with $E = 2.5$ MPa and $\nu = 0.25$.

h -adaptive strategy

To obtain a suitable starting point, we refine the initial mesh three times uniformly, thus starting the adaptive algorithm with 128 cells. We compute three adaptive loops with $\Theta = 0.05$. As an underlying method we chose the $\mathbb{P}_3\mathbb{P}_1$ variant of the weakly conforming method. The resulting errors and error estimator values can be seen in Tab. 5.1 and the resulting mesh in Fig. 5.4. It can be seen, that with increasing refinement both error measures decrease, as well as both error estimator terms. Note, that this example is not designed to be highly effective, but rather to demonstrate the functionality of the algorithm, since this example has no singularities or other stress spikes.

cells	128	200	242	342
dim M_h^{wc}	832	1 264	1 516	2 116
$\ \mathbf{u} - \mathbf{u}_h^{\text{wc}}\ _{0,\Omega}$	6.794e-05	2.318e-05	1.691e-05	1.332e-05
$ \mathbf{u} - \mathbf{u}_h^{\text{wc}} _{E,\Omega_h}$	0.05295	0.03585	0.03521	0.02691
η_{primal}	0.04719	0.02139	0.02057	0.01602
η_{dual}	0.11972	0.08459	0.06498	0.05126

Table 5.1: Unit square example: Resulting error estimator values and errors for the h -adaptive strategy.

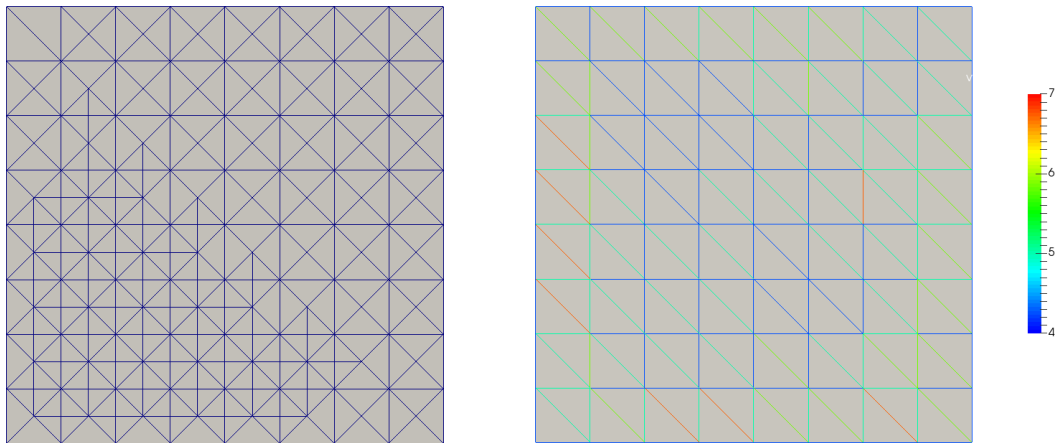


Figure 5.4: Unit square example: resulting mesh after three h -adaptive refinement steps with the weakly conforming method (left), distribution of face degrees of freedom after three p -adaptive refinement steps (right).

***p*-adaptive strategy**

To test the second strategy, *p*-refinement, we use the same example and compute two variants: In the first one we refine the initial mesh three times uniformly and set $\Theta = 0.03$. In the second variant we refine the initial mesh four times and set $\Theta = 0.05$. In both computations we start with cubic ansatz functions in the cells and four degrees of freedom per face, i.e. the $\mathbb{P}_3\mathbb{P}_1$ method. With this initial setup we compute three adaptive loops. The resulting face degrees of freedom are displayed in Fig. 5.4 for the first case; the resulting values of both error measures and error estimator terms for both cases are given in Tab. 5.2. The results are similar to the results with *h*-refinement. With increasing refinement of the faces all discussed values are decreasing, as expected. However, we observe that both errors as well as both estimators are decreasing much faster when the mesh is spatially refined, than with pure *p*-adaptive refinement. This is a known behavior, that *p*-refinement should always be coupled with a suitable spatial resolution of the mesh, for example in the next example we couple *p*-refinement with graded cells to sufficiently refine a singularity.

After this proof of concept for both refinement methods, we can move on to more difficult to compute meshes, where singularities allow for a highly efficient use of degrees of freedom and compare the adaptive efficiency to the efficiency of uniform refinement.

5.4 Adaptive strategies for the L-shaped domain

In the first adaptive test we compute the problem described in Sec. 4.2 again, but this time we use two different adaptive schemes to improve the efficiency.

***p*-adaptive strategy.**

For the first computation we use quadrilateral meshes and therefore only *p*-refinement, where we increase the multiplier spaces M_F on selected faces F but do not refine the spatial mesh to avoid hanging nodes. Since we do not refine

cells	128	128	128	128
dim M_h^{wc}	832	868	913	967
$\ \mathbf{u} - \mathbf{u}_h^{\text{wc}}\ _{0,\Omega}$	6.794e-05	6.157e-05	5.178e-05	2.878e-05
$ \mathbf{u} - \mathbf{u}_h^{\text{wc}} _{\text{E},\Omega_h}$	0.05295	0.04988	0.04601	0.03709
η_{primal}	0.04719	0.04281	0.03617	0.02184
η_{dual}	0.11972	0.10896	0.10248	0.10114
cells	512	512	512	512
dim M_h^{wc}	3 200	3 440	3 599	3 717
$\ \mathbf{u} - \mathbf{u}_h^{\text{wc}}\ _{0,\Omega}$	1.118e-05	8.298e-06	7.550e-06	7.422e-06
$ \mathbf{u} - \mathbf{u}_h^{\text{wc}} _{\text{E},\Omega_h}$	0.01571	0.01321	0.01267	0.01256
η_{primal}	0.01635	0.01156	0.01039	0.01015
η_{dual}	0.01131	0.00836	0.00813	0.00789

Table 5.2: Unit square example: Resulting error estimator values and errors for the p -adaptive strategy.

the cells with this strategy, we choose on each mesh level the corresponding graded mesh with $\gamma = \alpha^{\frac{3}{2}}$ to refine the singularity sufficiently and to increase the convergence rate.

The results for the p -adaptive strategy are visualized in Fig. 5.5, where the L_2 error and the energy error are plotted against the number of degrees of freedom for every discussed mesh refinement strategy for the $\mathbb{P}_3\mathbb{P}_1$ weakly conforming method and for the p -adaptive strategy. It becomes evident, that the highly resolved singularity leads to a higher efficiency for the adaptive method compared to the uniform weakly conforming method. The adaptive method needs only about 10% of the degrees of freedom to achieve the same level of accuracy with respect to the L_2 -error, compared to the uniform computation on the same graded mesh. The experimental orders of convergence for all mesh variants can be seen in Tab. 5.3. R_l with respect to the energy error is increasing with each improvement of the mesh: It starts low on the uniform mesh and increases for both graduation strategies, until it reaches its peak for the adaptive computations. The same holds true for R_l with respect to the L_2 error, which increases even further with each mesh improvement.

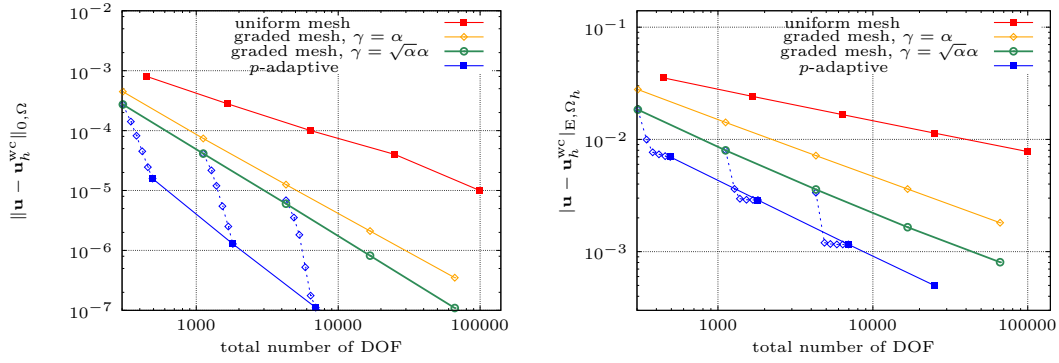


Figure 5.5: L-shaped domain example: p -adaptive realization of the example introduced in Sec. 4.2. Comparison of the error in the L_2 norm (left) and energy norm (right) for the $\mathbb{P}_3\mathbb{P}_1$ weakly conforming method with the p -adaptive variant of the weakly conforming method on quadrilateral meshes.

Uniform refinement				
$\dim M_{h,2}^{\text{wc}}$	448	1 664	6 400	25 088
$\ \mathbf{u} - \mathbf{u}_{h,2}^{\text{wc}}\ _{0,\Omega}$	0.00080	0.00028	0.00010	0.00004
R_l		2.83	2.80	2.75
$ \mathbf{u} - \mathbf{u}_{h,2}^{\text{wc}} _{E,\Omega_h}$	0.03527	0.02419	0.01659	0.01137
R_l		1.46	1.46	1.46
Graded ref., $\gamma = \alpha$				
$\dim M_{h,2}^{\text{wc}}$	304	1 120	4 288	16 768
$\ \mathbf{u} - \mathbf{u}_{h,2}^{\text{wc}}\ _{0,\Omega}$	0.00045	0.00007	0.00001	2.104e-06
R_l		6.05	5.89	5.95
$ \mathbf{u} - \mathbf{u}_{h,2}^{\text{wc}} _{E,\Omega_h}$	0.02784	0.01417	0.00717	0.00361
R_l		1.97	1.98	1.99
Graded ref., $\gamma = \alpha^{\frac{3}{2}}$				
$\dim M_{h,2}^{\text{wc}}$	304	1 120	4 288	16 768
$\ \mathbf{u} - \mathbf{u}_{h,2}^{\text{wc}}\ _{0,\Omega}$	0.00027	0.00004	6.021e-06	8.172e-07
R_l		6.62	6.85	7.37
$ \mathbf{u} - \mathbf{u}_{h,2}^{\text{wc}} _{E,\Omega_h}$	0.01841	0.00799	0.00358	0.00165
R_l		2.31	2.23	2.16
Adaptive refinement				
$\dim M_{h,2}^{\text{wc}}$	492	1 811	6 950	24 903
$\ \mathbf{u} - \mathbf{u}_h^{\text{wc}}\ _{0,\Omega}$	1.581e-05	1.284e-06	1.111e-07	1.822e-08
R_l		12.34	11.57	6.10
$ \mathbf{u} - \mathbf{u}_h^{\text{wc}} _{E,\Omega_h}$	0.00698	0.00288	0.00116	5.005e-04
R_l		2.42	2.48	2.32

Table 5.3: L-shaped domain example: Comparison of both error measures for all quadrilateral mesh variants, computed with the $\mathbb{P}_3\mathbb{P}_1$ variant of the weakly conforming method, including experimental orders of convergence.

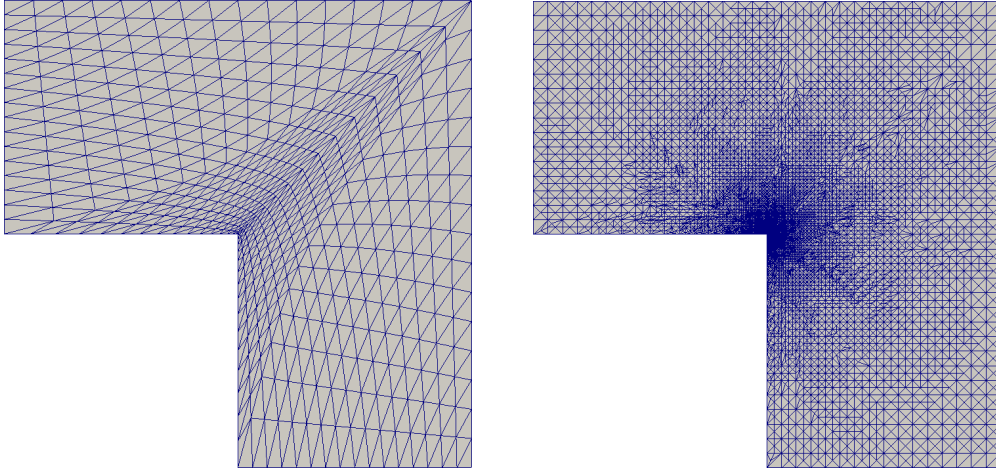


Figure 5.6: L-shaped domain example: Graded triangular mesh with $\gamma = \alpha^{\frac{3}{2}}$ (left), resulting mesh after several h -adaptive refinement steps with the weakly conforming method (right).

***hp*-adaptive strategy on a triangular mesh.**

Now the same example is computed on a triangular mesh, deploying an *hp-adaptive strategy*. Here we use triangular meshes, since the refinement of triangles can be easily performed without generating faces with hanging nodes, cf. Fig. 5.1. For a comparison of the results, we use computations on a uniformly refined triangular mesh, as well as two graded triangular meshes, with $\gamma = \alpha$ and $\gamma = \alpha^{\frac{3}{2}}$ respectively. The graded mesh with $\gamma = \alpha^{\frac{3}{2}}$ can be seen in Fig. 5.6, together with a h -refined mesh after several refinement steps, where we started with a uniformly refined initial mesh. It can be clearly seen, that the cells around the singularity are highly refined, which is to be expected.

The deployment of *hp*-adaptivity leads to a significant increase in efficiency compared to the uniform meshes and even the graded meshes, cf. Fig. 5.7, resulting in a much smaller required number of degrees of freedom to achieve a similar level of accuracy, with respect to the L_2 -error. We only need a fraction of degrees of freedom to achieve the same level of accuracy, compared to the pre-computed meshes. The R_l for all mesh variants can be seen in Tab. 5.4. As expected, the uniform refined yields again only a reduced rate of convergence, while the graduation increases it. The graduations with both values for γ yield comparable R_l , while the stronger graduation with $\gamma = \alpha^{\frac{3}{2}}$ has a smaller error constant. The R_l for the adaptive strategy are comparably high, in the last

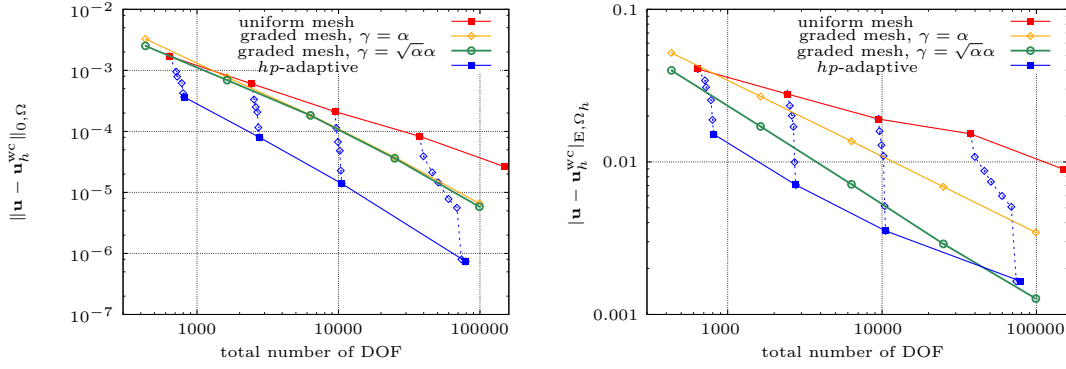


Figure 5.7: L-shaped domain example: Comparison of the error in the L_2 and energy norm for the $\mathbb{P}_3\mathbb{P}_1$ weakly conforming method with the hp -adaptive weakly conforming method on triangular meshes.

step the rate for the L_2 error has a significant jump, which is caused by the large increase of degrees of freedom between these two adaptive computations. The energy error however yields for this last level only a small convergence rate $R_l \approx 3^{-1}$, which explains, why with respect to the energy-error, our adaptive computations could not beat the last computed refinement step of the graded mesh with $\gamma = \alpha^{\frac{3}{2}}$. We are confident, that there are parameter sets, which perform better, but this illustrates the problem with parameters, which are in this case introduced by our adaptive algorithm. When every parameter has to be set by hand and adjusted for every computation, it can be time consuming and difficult to find optimal settings.

5.5 A corner singularity in 3D

In the next example we consider a 3D adaptive example, this time with a p -adaptive strategy. A junction of three bars is fixed at the end of one bar and traction forces are applied at the ends $\partial\Omega_B$ of the other two bars, cf. Fig. 5.8. The resulting three-legged domain consists of 7 cubical cells, each of which has the dimensions $1 \times 1 \times 1\text{mm}^3$. The traction forces which are applied on the two bars are $\mathbf{t}_{N,x_3} = (-0.05, -0.05, 0)\text{N}$ on the bar perpendicular to the x_3 axis and $\mathbf{t}_{N,x_1} = (0, -0.05, -0.05)\text{N}$ on the bar perpendicular to the x_1 axis.

Uniform refinement					
$\dim M_{h,2}^{\text{wc}}$	640	2 432	9 472	37 376	
$\ \mathbf{u} - \mathbf{u}_h^{\text{wc}}\ _{0,\Omega}$	0.00170	6.019e-04	2.112e-04	8.317e-05	
R_l	2.83		3.29	2.54	
$ \mathbf{u} - \mathbf{u}_h^{\text{wc}} _{E,\Omega_h}$	0.04063	0.02786	0.01910	0.01528	
R_l	1.46		1.46	1.25	
Graded refinement, $\gamma = \alpha$					
$\dim M_{h,2}^{\text{wc}}$	432	1 632	6 336	24 960	
$\ \mathbf{u} - \mathbf{u}_h^{\text{wc}}\ _{0,\Omega}$	0.00328	7.709e-04	1.868e-04	3.780e-05	
R_l	4.25		4.12	4.92	
$ \mathbf{u} - \mathbf{u}_h^{\text{wc}} _{E,\Omega_h}$	0.05186	0.02684	0.01365	0.00687	
R_l	1.94		1.96	1.99	
Graded refinement, $\gamma = \alpha^{\frac{3}{2}}$					
$\dim M_{h,2}^{\text{wc}}$	432	1632	6336	24960	
$\ \mathbf{u} - \mathbf{u}_h^{\text{wc}}\ _{0,\Omega}$	0.00252	6.916e-04	1.826e-04	3.615e-05	
R_l	3.65		3.78	5.08	
$ \mathbf{u} - \mathbf{u}_h^{\text{wc}} _{E,\Omega_h}$	0.03982	0.01708	0.00713	0.00290	
R_l	2.33		2.41	2.46	
Adaptive refinement					
$\dim M_{h,2}^{\text{wc}}$	810	2 764	10 538	79 284	
$\ \mathbf{u} - \mathbf{u}_h^{\text{wc}}\ _{0,\Omega}$	3.661e-04	7.980e-05	1.395e-05	7.375e-07	
R_l	4.58		5.70	18.90	
$ \mathbf{u} - \mathbf{u}_h^{\text{wc}} _{E,\Omega_h}$	0.01520	0.00706	0.00353	0.00165	
R_l	2.14		2.00	2.14	

Table 5.4: L-shaped domain example: Comparison of both error measures for all triangular mesh variants, computed with the $\mathbb{P}_3\mathbb{P}_1$ variant of the weakly conforming method, including experimental orders of convergence.

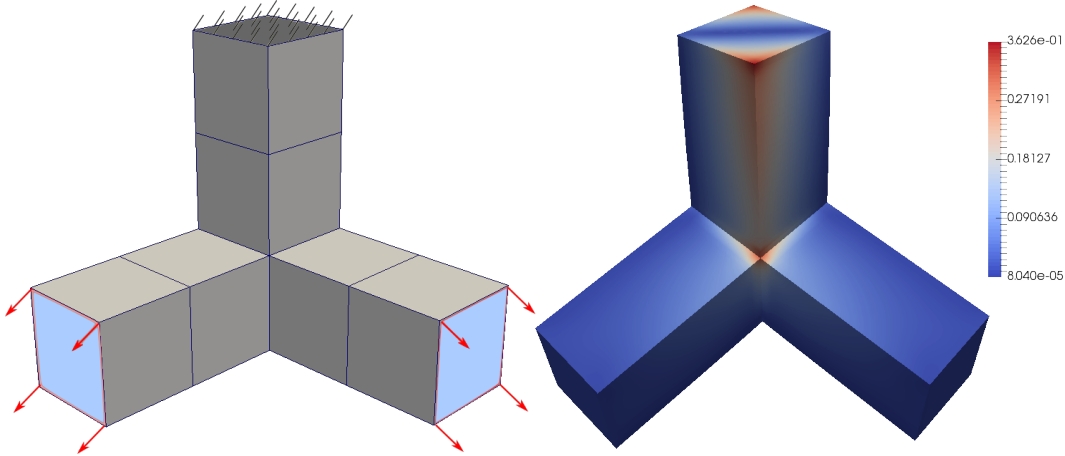


Figure 5.8: Junction of three bars example: Geometric configuration including boundary conditions and cell distribution (left) and stress distribution $|\boldsymbol{\sigma}(\mathbf{u})|$ illustrating strong corner and edge singularities (right).

We use a compressible linear elastic material with $E = 2.5$ MPa and $\nu = 0.25$.

In this configuration the three arising singularities result in a low regularity of the solution, which justifies the usage of adaptive strategies, since the extra effort for computing the same problem on different mesh iterations is recouped by the gain of efficiency.

For the p -adaptive algorithm, the starting mesh seen in Fig.5.8 is uniformly refined three times and each of the three refined meshes is used as a starting point for our adaptive algorithm, leaving us with adaptive computations on meshes with 56, 448 and 3584 cells. For each computation we set $\Theta = 0.05$ and compute four p -adaptive loops. The resulting displacements of these adaptive computations can be seen as data points in Fig. 5.9. Additionally we compute this example with two uniform conforming methods and two uniform variations of the weakly conforming methods and compare these results with our adaptive computations. By extrapolation we obtain the asymptotic value $\|\mathbf{u}\|_{0,\partial\Omega_B} \approx 0.11875$ which is used for the error measurement. The convergence for the displacement $\|\mathbf{u}_h\|_{0,\partial\Omega_B}$ is again reduced due to the singularities, with the optimal convergence rate of $\kappa = \frac{3}{2}$. All methods have an R_l around that value, for details see Tab. 5.5. The weakly conforming method of lowest order is slightly less efficient than the conforming method, while the higher order ansatz is superior to the quadratic conforming method. Since we observe

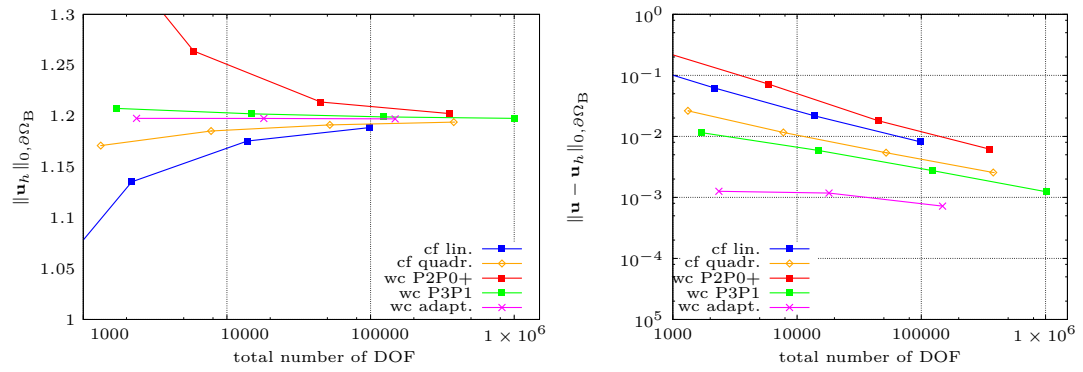


Figure 5.9: Junction of three bars example: Convergence of $\|\mathbf{u}\|_{0, \partial\Omega_B}$ and the error for conforming and weakly conforming $\mathbb{P}_3\mathbb{P}_1$ approximations compared with the results for the p -adaptive weakly conforming method.

multiple singularities of various magnitude in this example, the p -adaptive scheme yields a significant improvement, achieving the same accuracy as by uniform refinement with only a small fraction of global degrees of freedom. Even when we use the lowest starting mesh refinement with only 56 cells and 2349 degrees of freedom, we achieve the same level of accuracy as we do with the second most accurate method on 28672 cells, with 1011456 degrees of freedom.

$\dim V_{h,1}^{\text{cf}}$	405		2 175		13 851		97 971
$\ \mathbf{u}_h\ _{0,\partial\Omega_B}$	1.01027		1.12561		1.16580		1.17934
difference		0.11534		0.04019		0.01354	
R_l			2.87		2.97		
$\dim V_{h,2}^{\text{cf}}$	1 323		7 755		52 083		379 491
$\ \mathbf{u}_h\ _{0,\partial\Omega_B}$	1.16127		1.17590		1.18209		1.18494
difference		0.01463		0.00619		0.00285	
R_l			2.36		2.17		
$\dim M_{h,1}^{\text{wc}}$	796		5 872		44 992		352 000
$\ \mathbf{u}_h\ _{0,\partial\Omega_B}$	1.43761		1.25966		1.20557		1.19371
difference		0.17795		0.05409		0.01186	
R_l			3.29		4.56		
$\dim M_{h,2}^{\text{wc}}$	1 692		14 832		123 840		1 011 456
$\ \mathbf{u}_h\ _{0,\partial\Omega_B}$	1.19903		1.19339		1.19024		1.18874
difference		0.00564		0.00315		0.00150	
R_l			1.79		2.10		

Table 5.5: Junction of three bars example: Comparison of $\|\mathbf{u}_h\|_{0,\partial\Omega_B}$ for the different discretization schemes, including experimental orders of convergence.

Chapter 6

Non-linear materials

Content of this chapter In the previous chapters all examples are formulated for linear elastic materials. Since these materials only represent a small portion of materials that exist in reality, we need other, more sophisticated material models that broaden the spectrum. In this chapter we introduce strain elastic materials, damage and plasticity models and a contact problem, where two bodies of different material collide and exert pressure to one another.

Origin of this chapter For the hyperelastic theory we refer to [30]; for computational plasticity we follow [55] and the elasto-plastic damage model is taken from Spahn [56]. The application of the weakly conforming method to these models is part of the SPP project [15, 17]. Contact formulations and their applications are described in [60].

6.1 Hyperelasticity

Linear elastic materials are only a viable physical model for small deformations. To linearize the governing equations of elasticity we ignore strain terms of quadratic and higher orders, which is only a sensible choice if they vanish, due to the smallness of the strains itself. If we want to compute larger deformations, we need non-linear materials. For the discussion of hyperelastic materials, we first recall the following system, which we aim to solve, cf. eq. (2.1) and eq.

(2.2)

$$\begin{aligned}
-\operatorname{div} \mathbf{T} &= \mathbf{f} \text{ in } \Omega, \\
\mathbf{T} \mathbf{n} &= \mathbf{t}_N \text{ on } \partial\Omega_N, \\
\mathbf{u} &= \mathbf{u}_D \text{ on } \partial\Omega_D,
\end{aligned}$$

where \mathbf{T} is the first Piola-Kirchhoff stress tensor, \mathbf{t}_N is a given traction force acting on the Neumann boundary $\partial\Omega_N$ and \mathbf{u}_D is the given Dirichlet data. To solve this with the weakly conforming method, we use again the ansatz space V_h^{wc} , which we introduce in Chapter 3. Since we consider hyperelastic materials, the material has a so called strain energy functional

$$\mathcal{W}(\cdot) : \mathbb{M}_+^3 = \{\mathbf{F} \in \mathbb{R}^{3,3} : \det \mathbf{F} > 0\} \rightarrow \mathbb{R}.$$

We now aim to find the weakly conforming solution $\mathbf{u}_h^{\text{wc}} \in \mathbf{V}_h^{\text{WC}}$ minimizing this energy

$$\mathcal{E}(\mathbf{u}_h) := \sum_{K \in \mathcal{K}_h} \int_K \mathcal{W}(\mathbf{F}) \, d\mathbf{x} - \int_{\Omega} \mathbf{f} \cdot \mathbf{u}_h \, d\mathbf{x} - \int_{\partial\Omega_N} \mathbf{t}_N \cdot \mathbf{u}_h \, d\mathbf{a},$$

with $D_{\mathbf{F}}\mathcal{W}(\mathbf{F}) = \mathbf{T}$ and $\mathbf{F} = D\mathbf{u} + \mathbf{I}$. To solve this we need to iterate over three nested loops, one for the discretization of the time and two nested Newton methods, since we have to solve a non-linear system in each cell to assemble the local saddle point matrices and afterwards we have to solve a non-linear problem globally, cf. Algorithm 4.

Discretization of time

To discretize the time we introduce a series of time steps and gradually increase the forces \mathbf{t}_N and \mathbf{f} . Let $0 = t_0 < t_1 < \dots < t_{N_{\max}} = T$ be a time series with $\Delta t_n = t_n - t_{n-1}$ and let $\mathbf{t}_N(t) = t \cdot \mathbf{t}_N$ and $f(t) = t \cdot f$. As a solver, we use an implicit Euler method. In each time step n , we first compute for every cell K the right hand side ℓ_K^n and start subsequently our first Newton method. In the following the running indices are set to n for the time discretization, k for the outer Newton method and j for the inner Newton method.

Inner Newton method

Inside the inner Newton method we compute $\ell_K^n(\mathbf{u}_K^{n,k,j})$ by

$$\langle \ell_K^n(\mathbf{u}_K^{n,k,j}), \mathbf{v}_K \rangle = \langle \ell^n, \mathbf{v}_K \rangle - \left(\partial_{\mathbf{F}} \mathcal{W}(\mathbf{F}^{n,k,j}), D\mathbf{v}_K \right) \quad \text{for } \mathbf{v}_K \in V_K.$$

With this we compute

$$\begin{pmatrix} \Delta \mathbf{u}_K^{n,k,j} \\ \Delta \boldsymbol{\lambda}_K^{n,k,j} \end{pmatrix} = \begin{pmatrix} A_K^{n,k,j} & B_K \\ B_K^\top & 0 \end{pmatrix}^{-1} \begin{pmatrix} \ell_K^n(\mathbf{u}_K^{n,k,j}) \\ \hat{B}_K \hat{\mathbf{u}}_h^{n,k} \end{pmatrix},$$

with $A_K^{n,k,j} = \partial_{\mathbf{F}^2} \mathcal{W}(\mathbf{F}^{n,k,j})$. Note, that the local matrices B_K do not depend on time and need to be assembled only once. Next we set $\mathbf{u}_K^{n,k,j+1} = \mathbf{u}_K^{n,k,j} + \Delta \mathbf{u}_K^{n,k,j}$ and continue with the next iteration. Once the inner Newton method stops, which is when the residual $|\ell_K^n(\mathbf{u}_K^{n,k,j})|$ is small enough, we set $\ell_K^{n,k} = \ell_K^n(\mathbf{u}_K^{n,k,j})$, assemble the global system and proceed with the current step of the outer Newton method.

Outer Newton method

Once the inner loop has stopped, we assemble the global system

$$\begin{aligned} \hat{A}_h^{n,k} &= \sum_K \begin{pmatrix} 0 \\ \hat{B}'_K \end{pmatrix}^\top \begin{pmatrix} A_K^{n,k} & B'_K \\ B_K & 0 \end{pmatrix}^{-1} \begin{pmatrix} 0 \\ \hat{B}_K \end{pmatrix}, \\ \hat{\ell}_h^{n,k} &= \sum_K \begin{pmatrix} 0 \\ \hat{B}'_K \end{pmatrix}^\top \begin{pmatrix} A_K^{n,k} & B'_K \\ B_K & 0 \end{pmatrix}^{-1} \begin{pmatrix} \ell_K^{n,k} \\ 0 \end{pmatrix}. \end{aligned}$$

With these we compute the increment $\Delta \hat{\mathbf{u}}_h^{\text{wc},n,k}$ by solving the linearized system $\hat{A}_h^{n,k} \Delta \hat{\mathbf{u}}_h^{\text{wc},n,k} = \hat{\ell}_h^{n,k}$ and update $\hat{\mathbf{u}}_h^{\text{wc},n,k+1} = \hat{\mathbf{u}}_h^{\text{wc},n,k} + \Delta \hat{\mathbf{u}}_h^{\text{wc},n,k}$. The outer Newton method, with which we compute the solution to our global non-linear problem, stops when the residual $|\hat{\ell}_h^{n,k}|$ is small enough. At this point, the current time step is finished and we can proceed with the next one by setting $n = n + 1$, $t = t + \Delta t$. After the last time step we get the desired solution $\hat{\mathbf{u}}_h^{\text{wc}} = \hat{\mathbf{u}}_h^{\text{wc},n,k}$.

The non-linear algorithm requires a lot of assembly time, since we assemble different matrices in all steps of the nested methods, however, due to the high

speedup of the assembly time this can be solved by utilizing a high number of parallel processes, cf. Table 3.3.

Algorithm 4 Hyperelastic materials

```

1: Input:  $\text{eps}_d, \text{eps}_r, T, \mathcal{K}_h, \mathbf{t}_N, \mathbf{f}$ 
2:  $t = 0, n = 0, \hat{\mathbf{u}}_h^{\text{wc}} = \mathbf{0}$ 
3: for  $K \in \mathcal{K}_h$  do
4:   assemble  $B_K$ 
5: end for
6: while  $t < T$  do
7:   Compute  $\hat{\mathbf{u}}_h^{\text{wc},n,0}$  from  $\mathbf{u}_D$ 
8:   for  $K \in \mathcal{K}_h$  do
9:     Compute  $\ell_K^n$ 
10:  end for
11:   $k = 0$ 
12:  while  $d^n > \text{eps}_d$  do
13:    for  $K \in \mathcal{K}_h$  do
14:       $j = 0$ 
15:      compute  $\ell_K^n(\mathbf{u}_K^{n,k,j})$ 
16:      while  $|\ell_K^n(\mathbf{u}_K^{n,k,j})| > \text{eps}_r$  do
17:        assemble  $A_K^{n,k,j}$ 
18:        compute  $\begin{pmatrix} \Delta \mathbf{u}_K^{n,k,j} \\ \Delta \boldsymbol{\lambda}_K^{n,k,j} \end{pmatrix} = \begin{pmatrix} A_K^{n,k,j} & B_K \\ B_K^\top & 0 \end{pmatrix}^{-1} \begin{pmatrix} \ell_K^n(\mathbf{u}_K^{n,k,j}) \\ \hat{B}_K \hat{\mathbf{u}}_h^{n,k} \end{pmatrix}$ 
19:        update  $\mathbf{u}_K^{n,k,j+1} = \mathbf{u}_K^{n,k,j} + \Delta \mathbf{u}_K^{n,k,j}$  and compute  $\ell_K^n(\mathbf{u}_K^{n,k,j+1})$ 
20:         $j = j + 1$ 
21:      end while
22:    end for
23:    assemble  $\hat{A}_h^{n,k} = \sum_K \begin{pmatrix} 0 \\ \hat{B}_K' \end{pmatrix}^\top \begin{pmatrix} A_K^{n,k} & B_K' \\ B_K & 0 \end{pmatrix}^{-1} \begin{pmatrix} 0 \\ \hat{B}_K \end{pmatrix}$ ,
24:    assemble  $\hat{\ell}_h^{n,k} = \sum_K \begin{pmatrix} 0 \\ \hat{B}_K' \end{pmatrix}^\top \begin{pmatrix} A_K^{n,k} & B_K' \\ B_K & 0 \end{pmatrix}^{-1} \begin{pmatrix} \ell_K^n(\mathbf{u}_K^{n,k,j}) \\ 0 \end{pmatrix}$ .
25:    compute  $\Delta \hat{\mathbf{u}}_h^{\text{wc},n,k}$  with  $\hat{A}_h^{n,k} \Delta \hat{\mathbf{u}}_h^{\text{wc},n,k} = \hat{\ell}_h^{n,k}$ 
26:     $\hat{\mathbf{u}}_h^{\text{wc},n,k+1} = \hat{\mathbf{u}}_h^{\text{wc},n,k} + \Delta \hat{\mathbf{u}}_h^{\text{wc},n,k}$ 
27:     $d^n = |\hat{\ell}_h^{n,k}|$ 
28:     $k = k + 1$ 
29:  end while
30:   $t = t + \Delta t_n$ 
31:   $n = n + 1$ 
32: end while
33: Output:  $\hat{\mathbf{u}}_h^{\text{wc}}$ 

```

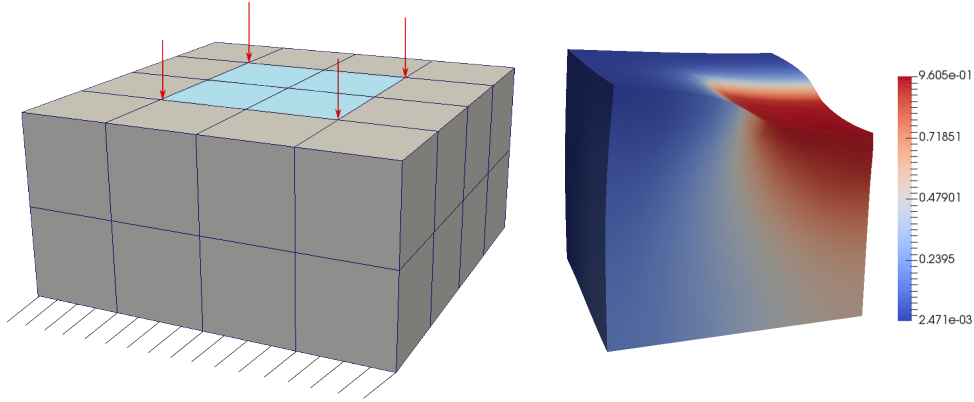


Figure 6.1: Compression block: Geometric configuration including boundary conditions and cell distribution (left) and stress distribution $|\boldsymbol{\sigma}(\mathbf{u})|$ on the actual computed quarter, depicting the large deformation of the block center (right).

Hyperelastic compression test

To test the behavior of the weakly conforming method for large strain deformations, we compute an example where we take a hexahedron with dimensions $100 \text{ mm} \times 100 \text{ mm} \times 50 \text{ mm}$, consisting of a hyperelastic material, cf. [53]. This hexahedron is fixed in vertical direction on the bottom side, but can slide in all horizontal directions. On a part of its topside a downward pressure of $2186,25 \text{ MPa}$ is applied, cf. Fig. 6.1. Since there is no real Dirichlet boundary, we cannot compute the whole block, since movement in horizontal directions would be unrestricted. For this reason, we compute only a quarter of the block, which additionally also decreases the problem size significantly. With the help of the symmetry boundaries in both horizontal directions, the problem is well-posed.

As a material we choose a Neo-Hooke material with $E = 2.5 \text{ MPa}$ and $\nu = 0.25$ and

$$\mathcal{W}(\mathbf{F}) = \frac{\mu}{2}(\mathbf{F} : \mathbf{F} - 3 - 2 \ln(J)) + \frac{\lambda}{4}(J^2 - 1 - 2 \ln(J)), \quad (6.1)$$

where $J = \det \mathbf{F}$.

To assess the quality of the computations, we measure the vertical displacement $u_3(\mathbf{A})$ of a control point $\mathbf{A} = (50, 50, 50)$. The results are displayed in

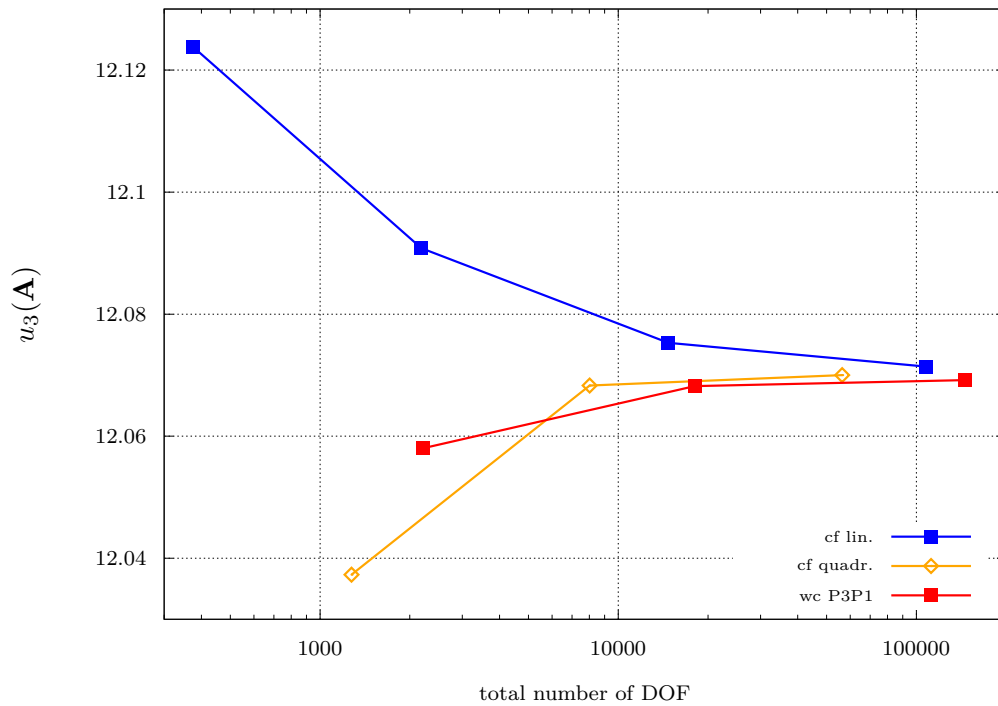


Figure 6.2: Compression test: Vertical displacement $u_3(\mathbf{A})$ at the control point $\mathbf{A} = (50, 50, 50)$ for two conforming methods and the $\mathbb{P}_3\mathbb{P}_1$ weakly conforming method.

Fig. 6.2. It can be seen, that the linear conforming method converges slower than the two higher order methods, which is to be expected, but there is no strong locking, so the linear method is not far less efficient. On the other hand, the quadratic conforming method and the $\mathbb{P}_3\mathbb{P}_1$ weakly conforming method are close together and are comparably efficient.

However, this test also shows, that there is still work to be done when it comes to the weakly conforming method with large strain deformations. While the established methods have little problems to converge for even further deformed configurations, the weakly conforming method could not compute beyond this deformation in the given setting since the Newton method did not converge for larger traction forces. One problem is, that the condition numbers of the local saddle point matrices increase when the deformation is increased. A scaling of the matrices B_K showed promising results, that this could decrease this effect, but this has to be further investigated.

6.2 Elasto-plastic damage model

We aim to find displacements $\mathbf{u}: [0, T] \times \Omega \rightarrow \mathbb{R}^3$ in the time interval $[0, T]$ of a material which is described by internal variables $\mathbf{z}: [0, T] \times \Omega \rightarrow \mathbb{R}^N$ and where the evolution is determined by the total energy and dissipation functionals

$$\begin{aligned}\mathcal{E}(t, \mathbf{u}, \mathbf{z}) &= \int_{\Omega} \mathcal{W}(\mathbf{x}, \boldsymbol{\varepsilon}(\mathbf{u}), \mathbf{z}) \, d\mathbf{x} - \langle \ell(t), \mathbf{u} \rangle, \\ \mathcal{R}(\dot{\mathbf{z}}) &= \int_{\Omega} R(\mathbf{x}, \dot{\mathbf{z}}) \, d\mathbf{x},\end{aligned}$$

where the load functional is given again by

$$\langle \ell(t), \delta \mathbf{u} \rangle = \int_{\Omega} \mathbf{f}(t) \cdot \delta \mathbf{u} \, d\mathbf{x} + \int_{\partial\Omega_N} \mathbf{t}_N(t) \cdot \delta \mathbf{u} \, d\mathbf{a}, \quad \delta \mathbf{u} \in V(0),$$

with body forces $\mathbf{f}: [0, T] \times \Omega \rightarrow \mathbb{R}^3$ and traction forces $\mathbf{t}_N: [0, T] \times \partial\Omega_N \rightarrow \mathbb{R}^3$.

We assume that the material is rate-independent, i.e. the inelastic deformation is independent from scaling in time. This is achieved if the dissipation function R is 1-homogeneous.

We only consider small strains with the ansatz space $V = H^1(\Omega, \mathbb{R}^{\dim})$ for the displacements, and the test space $V(\mathbf{0}) = \{\mathbf{v} \in V : \mathbf{v} = \mathbf{0} \text{ on } \partial\Omega_D\}$ including homogeneous boundary conditions on the Dirichlet boundary $\partial\Omega_D \subset \partial\Omega$. For the internal variables we use the space $Z = L_2(\Omega, \mathbb{R}^N)$. If the total energy functional $\mathcal{E}: [0, T] \times V \times Z \rightarrow \mathbb{R}$ is bounded and uniformly convex in $V(\mathbf{0}) \times Z$ for all $t \in [0, T]$, and if the dissipation functional $\mathcal{R}: Z \rightarrow \mathbb{R} \cup \{\infty\}$ is convex, proper and lower semi-continuous, an energetic solution

$$(\mathbf{u}, \mathbf{z}): [0, T] \longrightarrow V \times Z$$

exists which is characterized by

$$\textbf{Equilibrium} \quad 0 = \partial_{\mathbf{u}} \mathcal{E}(t, \mathbf{u}(t), \mathbf{z}(t)), \quad (6.2a)$$

$$\textbf{Flow rule} \quad 0 \in \partial_{\mathbf{z}} \mathcal{E}(t, \mathbf{u}(t), \mathbf{z}(t)) + \partial \mathcal{R}(\dot{\mathbf{z}}(t)), \quad (6.2b)$$

and boundary conditions for the displacement $\mathbf{u}(t) = \mathbf{u}_D(t)$ on the Dirichlet boundary $\partial\Omega_D$.

In this model, we consider plasticity and damage. Therefore the internal variables are chosen as $\mathbf{z} = (\boldsymbol{\varepsilon}_p, r, d)$, where $\boldsymbol{\varepsilon}_p$ is the plastic strain tensor, $r(t) = \int_0^t |\partial_t \boldsymbol{\varepsilon}_p| dt$ the equivalent plastic strain and $d \in [0, 1)$ the damage variable, which indicates the level of damage at each point.

We split the energy term $\mathcal{W}(\mathbf{x}, \boldsymbol{\varepsilon}(\mathbf{u}), \mathbf{z})$ in three additive parts, an elastic part \mathcal{W}_e , a plastic part \mathcal{W}_p and a damage part \mathcal{W}_d , i.e.

$$\mathcal{W}(\boldsymbol{\varepsilon}, \mathbf{z}) = (1 - d)\mathcal{W}_e(\boldsymbol{\varepsilon} - \boldsymbol{\varepsilon}_p) = (1 - d)\left(\mathcal{W}_e(\boldsymbol{\varepsilon}(\mathbf{u}) - \boldsymbol{\varepsilon}_p) + \mathcal{W}_p(r)\right) + \mathcal{W}_d(d),$$

with

$$\begin{aligned}\mathcal{W}_e(\boldsymbol{\varepsilon}_e) &= \frac{1}{2}\mathbb{C}[\boldsymbol{\varepsilon}_e] \cdot \boldsymbol{\varepsilon}_e, \\ \mathcal{W}_p(r) &= \int_0^r \phi_p(\rho) \, d\rho, \quad \phi_p(r) = \sqrt{2/3}H_0r + \sqrt{2/3}K_0, \\ \mathcal{W}_d(d) &= \int_0^d \phi_d^{-1}(s) \, ds, \quad \phi_d(Y) = 1 - \exp\left(-H(\sqrt{2Y} - Y_0)\right).\end{aligned}$$

This means, that we use isotropic hardening and have no kinematic term, which is a sensible choice, since in our examples the flow direction does not change.

The dissipation is chosen to embed the irreversibility of both damage and plastic flow, for this reason it is penalizing a negative derivate of $\boldsymbol{\varepsilon}_p$ and d ,

$$\mathcal{R}(\dot{d}, \dot{\boldsymbol{\varepsilon}}_p, \dot{r}) = \int_{\Omega} R(\dot{d}, \dot{\boldsymbol{\varepsilon}}_p, \dot{r}) \, d\mathbf{x}, \quad R(\dot{d}, \dot{\boldsymbol{\varepsilon}}_p, \dot{r}) = R_d(\dot{d}) + R_p(\dot{\boldsymbol{\varepsilon}}_p, \dot{r}) \quad (6.3)$$

$$R_p(\dot{\boldsymbol{\varepsilon}}_p, \dot{r}) = \begin{cases} 0 & \dot{r} \geq |\dot{\boldsymbol{\varepsilon}}_p|, \\ +\infty & \text{otherwise,} \end{cases} \quad (6.4)$$

$$R_d(\dot{d}) = \begin{cases} 0 & \dot{d} \geq 0, \\ +\infty & \text{otherwise.} \end{cases} \quad (6.5)$$

For solving this problem, we choose a similar approach, as we did with the hyperelastic materials. We use again a time discretization and two nested Newton methods in our method, cf. Algorithm 6.

Discretization in time

Since this is a non-static model, we define an evolution in time. It is approximated by a series of incremental problems. Let $0 = t_0 < t_1 < \dots < t_{N_{\max}} = T$ be a time series with $\Delta t_n = t_n - t_{n-1}$. The time dimension is solved using an implicit Euler method. Starting with $(\mathbf{u}^0, \mathbf{z}^0)$ we define for $n = 1, \dots, N_{\max}$ the following incremental problems depending on the given memory variable

\mathbf{z}^{n-1} , the load functional $\ell^n = \ell(t_n)$ and the Dirichlet data $\mathbf{u}_D^n = \mathbf{u}_D(t_n)$: find a minimizer $(\mathbf{u}^n, \mathbf{z}^n) \in V(\mathbf{u}_D^n) \times Z$ of the incremental functional

$$\mathcal{J}_n(\mathbf{u}^n, \mathbf{z}^n) = \mathcal{E}(t_n, \mathbf{u}^n, \mathbf{z}^n) + \mathcal{R}(\mathbf{z}^n - \mathbf{z}^{n-1}).$$

In our applications $\mathcal{J}_n(\cdot)$ is uniformly convex, so that a unique minimizer exists. It is determined by computing a critical point of $\mathcal{J}_n(\cdot)$ characterized by the nonlinear system

$$\text{Discrete equilibrium} \quad 0 = \partial_{\mathbf{u}} \mathcal{E}(t_n, \mathbf{u}^n, \mathbf{z}^n), \quad (6.6a)$$

$$\text{Discrete flow rule} \quad 0 \in \partial_{\mathbf{z}} \mathcal{E}(t_n, \mathbf{u}^n, \mathbf{z}^n) + \partial \mathcal{R}(\Delta \mathbf{z}^n). \quad (6.6b)$$

Since we only consider rate-independent materials, the flow rule satisfies $\Delta t_n \mathcal{R}((\Delta t_n)^{-1}(\mathbf{z}^n - \mathbf{z}^{n-1})) = \mathcal{R}(\mathbf{z}^n - \mathbf{z}^{n-1})$ and thus depends only on the increment $\Delta \mathbf{z}^n = \mathbf{z}^n - \mathbf{z}^{n-1}$.

In each time step n , we first compute for every cell K the right hand side ℓ_K^n . With this, we start our first Newton method. As in the previous section, in the following the running indices are set to n for the time discretization, k for the outer Newton method and j for the inner Newton method.

Equilibrium

The equilibrium (6.2a) is defined by the non-linear system

$$\int_{\Omega} \boldsymbol{\sigma} \cdot \boldsymbol{\varepsilon}(\delta \mathbf{u}) \, d\mathbf{x} = \langle \ell(t), \delta \mathbf{u} \rangle, \quad \delta \mathbf{u} \in V(0)$$

with

$$\boldsymbol{\sigma} = \partial_{\boldsymbol{\varepsilon}_e} \mathcal{W}(\boldsymbol{\varepsilon}(\mathbf{u}), \boldsymbol{\varepsilon}_p, r, d) = (1 - d) \partial_{\boldsymbol{\varepsilon}_e} \mathcal{W}_e(\boldsymbol{\varepsilon}(\mathbf{u}) - \boldsymbol{\varepsilon}_p) = (1 - d) \mathbb{C}[\boldsymbol{\varepsilon}(\mathbf{u}) - \boldsymbol{\varepsilon}_p].$$

Employing this equation to the discrete equilibrium (6.6a) leads to a non-linear problem in every time increment: For given \mathbf{u}^{n-1} at nodal points and $d_{n-1}, \boldsymbol{\varepsilon}_{p,n-1}, r_{n-1}(\boldsymbol{\varepsilon})$ at integration points find \mathbf{u}^n with $\mathbf{u}^n = \mathbf{u}_D$ on $\partial\Omega_D$ solving the nonlinear problem

$$\int_{\Omega} \boldsymbol{\sigma}_n(\boldsymbol{\varepsilon}(\mathbf{u}^n)) \cdot \boldsymbol{\varepsilon}(\delta \mathbf{u}) \, d\mathbf{x} = \int_{\Omega} \mathbf{f}^n \cdot \delta \mathbf{u} \, d\mathbf{x} + \int_{\partial\Omega_N} \mathbf{t}_N^n \cdot \delta \mathbf{u} \, d\mathbf{a},$$

for all test functions $\delta \mathbf{u} \in V_h^{\text{wc}}(\mathbf{0})$, with the incremental stress response

$$\boldsymbol{\sigma}_n = (1 - d^n) \mathbb{C}[\boldsymbol{\varepsilon}(\mathbf{u}^n) - \boldsymbol{\varepsilon}_p^n].$$

To find this solution \mathbf{u}^n , we employ two Newton methods in every time step.

Outer Newton method

For the outer Newton method, we want to assemble the global system

$$\begin{aligned}\hat{A}_h^{n,k} &= \sum_K \begin{pmatrix} 0 \\ \hat{B}'_K \end{pmatrix}^\top \begin{pmatrix} A_K^{n,k} & B'_K \\ B_K & 0 \end{pmatrix}^{-1} \begin{pmatrix} 0 \\ \hat{B}_K \end{pmatrix}, \\ \hat{\ell}_h^{n,k} &= \sum_K \begin{pmatrix} 0 \\ \hat{B}'_K \end{pmatrix}^\top \begin{pmatrix} A_K^{n,k} & B'_K \\ B_K & 0 \end{pmatrix}^{-1} \begin{pmatrix} \ell_K^{n,k} \\ 0 \end{pmatrix}.\end{aligned}\tag{6.7}$$

But since the local systems, which are needed to compute $A_K^{n,k}$ and $\ell_K^{n,k}$ are non-linear, we need to use a second, embedded Newton method.

Inner Newton method

Inside the inner Newton method we compute

$$\begin{pmatrix} \Delta \mathbf{u}_K^{n,k,j} \\ \Delta \boldsymbol{\lambda}_K^{n,k,j} \end{pmatrix} = \begin{pmatrix} A_K^{n,k,j} & B_K \\ B_K^\top & 0 \end{pmatrix}^{-1} \begin{pmatrix} \ell_K^n(\mathbf{u}_K^{n,k,j}, \mathbf{z}^n) \\ \hat{B}_K \hat{\mathbf{u}}_h^{n,k} \end{pmatrix},$$

with

$$\begin{aligned}\langle A_K^{n,k,j} \mathbf{v}_K, \mathbf{w}_K \rangle &= \left((1 - d^{n,k,j}) \boldsymbol{\sigma}_n(\boldsymbol{\varepsilon}(\mathbf{u}_K^{n,k,j})), \boldsymbol{\varepsilon}(\mathbf{v}_K) \right)_{0,K} \\ &\quad - \left(\mathbb{C}_n(\boldsymbol{\varepsilon}(\mathbf{u}_K)) [\delta \boldsymbol{\varepsilon}(\mathbf{v}_K)], \boldsymbol{\varepsilon}(\mathbf{w}_K) \right)_{0,K}, \\ \langle \ell_K^n(\mathbf{u}_K^{n,k,j}, \mathbf{z}^n), \mathbf{v}_K \rangle &= \langle \ell^n, \mathbf{v}_K \rangle - (\boldsymbol{\sigma}_n(\mathbf{u}_K^{n,k,j}, \mathbf{z}^n), \boldsymbol{\varepsilon}(\mathbf{v}_K))_{0,K},\end{aligned}$$

where the $\mathbb{C}_n(\boldsymbol{\varepsilon}) \in \partial \boldsymbol{\sigma}_n(\boldsymbol{\varepsilon})$ is the consistent tangent, which will be defined below. Note, that the local matrices B_K do not depend on the time and need to be assembled only once. Next we set $\mathbf{u}_K^{n,k,j+1} = \mathbf{u}_K^{n,k,j} + \Delta \mathbf{u}_K^{n,k,j}$ and continue with the next iteration.

Once the inner residual $|\ell_K^n(\mathbf{u}_K^{n,k,j}, \mathbf{z}^n)|$ is small enough the embedded Newton method stops, we set $\ell_K^{n,k} = \ell_K^n(\mathbf{u}_K^{n,k,j}, \mathbf{z}^n)$ and we can proceed with the current step of the outer Newton method. The global system (6.7) is now assembled and we can compute the increment $\Delta \hat{\mathbf{u}}_h^{\text{wc},n,k}$ by solving the linearized system $\hat{A}_h^{n,k} \Delta \hat{\mathbf{u}}_h^{\text{wc},n,k} = \hat{\ell}_h^{n,k}$ and update $\hat{\mathbf{u}}_h^{\text{wc},n,k+1} = \hat{\mathbf{u}}_h^{\text{wc},n,k} + \Delta \hat{\mathbf{u}}_h^{\text{wc},n,k}$. The outer Newton method stops, when the residual $|\hat{\ell}_h^{n,k}|$ is small enough. At this point, the current time step is finished and we can proceed with the next one, by setting $n = n + 1$, $t = t + \Delta t$ and updating the memory variables.

Computation of the memory variables

Up to now we showed, how the memory variables influence the computation of the equilibrium. Now it must be clarified, how they are evolving. This is determined by the flow rule (6.2b). First we define the elasto-plastic energy $Y = \mathcal{W}_e(\boldsymbol{\varepsilon}(\mathbf{u}) - \boldsymbol{\varepsilon}_p) + \mathcal{W}_p(\boldsymbol{\varepsilon}_p, r)$, and the conjugated variables $\mathbf{y} = (\boldsymbol{\alpha}, \zeta, \xi) = -\partial_{\mathbf{z}}\mathcal{W}(\boldsymbol{\varepsilon}, \mathbf{z})$ with

$$\begin{aligned}\boldsymbol{\alpha} &= -\partial_{\boldsymbol{\varepsilon}_p}\mathcal{W}(\boldsymbol{\varepsilon}, \boldsymbol{\varepsilon}_p, r, d) = \partial_{\boldsymbol{\varepsilon}_p}(1-d)\mathcal{W}_e(\boldsymbol{\varepsilon}(\mathbf{u}) - \boldsymbol{\varepsilon}_p) = (1-d)(\operatorname{dev} \boldsymbol{\sigma}), \\ \zeta &= -\partial_r\mathcal{W}(\boldsymbol{\varepsilon}, \boldsymbol{\varepsilon}_p, r, d) = -\partial_r(1-d)\mathcal{W}_p(r) = -(1-d)\phi_p(r) \\ \xi &= -\partial_d\mathcal{W}(\boldsymbol{\varepsilon}, \boldsymbol{\varepsilon}_p, r, d) = \mathcal{W}_e(\boldsymbol{\varepsilon}(\mathbf{u}) - \boldsymbol{\varepsilon}_p) + \mathcal{W}_p(\boldsymbol{\varepsilon}_p, r) - \partial_d\mathcal{W}_d(d) = Y - \phi_d^{-1}(d).\end{aligned}$$

Then, we obtain

$$(\boldsymbol{\alpha}, \zeta) \in \partial R_p(\dot{\boldsymbol{\varepsilon}}_p, \dot{r}) \iff (\dot{\boldsymbol{\varepsilon}}_p, \dot{r}) \in \partial R_p^*(\boldsymbol{\alpha}, \zeta) \quad \text{and} \quad \xi \in \partial R_d(\dot{d}).$$

Introducing consistency parameters λ_p and λ_d this is equivalent to the normality rule, which states that the plastic strain increment vector is orthogonal to the yield surface,

$$\dot{\boldsymbol{\varepsilon}}_p = \lambda_p \frac{\boldsymbol{\alpha}}{|\boldsymbol{\alpha}|}, \quad \dot{r} = \lambda_p \quad \text{and} \quad \dot{d} = \lambda_d,$$

and the complementarity conditions

$$\lambda_p \geq 0, \quad |\boldsymbol{\alpha}| + \zeta \leq 0, \quad \lambda_p(|\boldsymbol{\alpha}| + \zeta) = 0 \quad \text{and} \quad \lambda_d \geq 0, \quad \xi \leq 0, \quad \lambda_d \dot{d} = 0.$$

This motivates the time-discretized formulation, where we introduce the analogue discretized variables: The discrete flow rule (6.6b) is evaluated from the discrete elasto-plastic energy $Y^n = \mathcal{W}_e(\boldsymbol{\varepsilon}(\mathbf{u}^n) - \boldsymbol{\varepsilon}_p^n) + \mathcal{W}_p(\boldsymbol{\varepsilon}_p^n, r^n)$ and the discrete conjugated variables

$$\begin{aligned}\boldsymbol{\alpha}^n &= (1-d^n)(\operatorname{dev} \boldsymbol{\sigma}^n), \\ \zeta^n &= -(1-d^n)\phi_p(r^n) \\ \xi^n &= Y^n - \phi_d^{-1}(d^n).\end{aligned}$$

Then, we obtain

$$(\Delta \boldsymbol{\varepsilon}_p^n, \Delta r^n) \in \partial R_p^*(\boldsymbol{\alpha}^n, \zeta^n) \quad \text{and} \quad \xi^n \in \partial R_d(\Delta d^n).$$

And together with the incremental consistency parameters λ_p^n and λ_d^n this is now equivalent to the discrete normality rule

$$\Delta \boldsymbol{\varepsilon}_p^n = \lambda_p^n \frac{\boldsymbol{\alpha}^n}{|\boldsymbol{\alpha}^n|}, \quad \Delta r^n = \lambda_p^n \quad \text{and} \quad \Delta d^n = \lambda_d^n,$$

and the complementarity conditions

$$\begin{aligned} \lambda_p^n &\geq 0, \quad |\boldsymbol{\alpha}^n| + \zeta^n \leq 0, \quad \lambda_p^n (|\boldsymbol{\alpha}^n| + \zeta^n) = 0 \\ \text{and} \quad \lambda_d^n &\geq 0, \quad \zeta^n \leq 0, \quad \lambda_d^n \Delta d^n = 0. \end{aligned}$$

Inserting the evaluation of the conjugated variables, we obtain

$$\begin{aligned} \lambda_p^n &\geq 0, \quad \left| (1 - d^n) (\text{dev } \boldsymbol{\sigma}^n) \right| - (1 - d^n) \phi_p(r^n) \leq 0, \\ \lambda_p^n &\left(\left| (1 - d^n) (\text{dev } \boldsymbol{\sigma}^n) \right| + \zeta^n \right) = 0 \end{aligned}$$

and

$$\lambda_d^n \geq 0, \quad Y^n - \phi_d^{-1}(d^n) \leq 0, \quad \lambda_d^n \Delta d^n = 0$$

and thus $\phi_d(Y^n) \leq d^n$. The complementarity condition for the damage variable is equivalent to

$$d^n = d^{n-1} + \max \left\{ 0, \phi_d(Y^n) - d^{n-1} \right\},$$

and starting with $d^0 = 0$ yields $d^n \in [0, 1)$. This finally yields for the plastic update independent of the damage process

$$\lambda_p^n \geq 0, \quad |\text{dev } \boldsymbol{\sigma}^n| - \phi_p(r^n) \leq 0, \quad \lambda_p^n (|\text{dev } \boldsymbol{\sigma}^n| + \zeta^n) = 0$$

and

$$\Delta \boldsymbol{\varepsilon}_p^n = \lambda_p \frac{\boldsymbol{\alpha}^n}{|\boldsymbol{\alpha}^n|} = \lambda_p \frac{\boldsymbol{\alpha}_{\text{tr}}^n}{|\boldsymbol{\alpha}_{\text{tr}}^n|},$$

with the relative trial stress $\boldsymbol{\alpha}_{\text{tr}}^n = \mathbb{C}[\boldsymbol{\varepsilon}(\mathbf{u}^n)] - 2\mu \boldsymbol{\varepsilon}_p^{n-1} = \boldsymbol{\alpha}^n - 2\mu + \Delta \boldsymbol{\varepsilon}_p^{n-1}$. Note that λ_p^n can be computed directly with the chosen hardening rules. Finally, the consistent tangent $\mathbb{C}_n(\boldsymbol{\varepsilon}) \in \partial \boldsymbol{\sigma}_n(\boldsymbol{\varepsilon})$ is given by

$$\begin{aligned} \mathbb{C}_n(\boldsymbol{\varepsilon})[\delta \boldsymbol{\varepsilon}] &= (1 - d_n(\boldsymbol{\varepsilon})) \mathbb{C}_n^{\text{plastic}}(\boldsymbol{\varepsilon})[\delta \boldsymbol{\varepsilon}] \\ &\quad - \text{sgn} \left(\max \left\{ 0, \phi_p(Y_n(\boldsymbol{\varepsilon})) - d^{n-1} \right\} \right) \left(\mathbb{C}[\boldsymbol{\varepsilon} - \boldsymbol{\varepsilon}_{p,n}(\boldsymbol{\varepsilon})] \cdot \delta \boldsymbol{\varepsilon} \right) \mathbb{C}[\boldsymbol{\varepsilon}] \end{aligned}$$

with

$$\begin{aligned} \mathbb{C}_n^{\text{plastic}}(\boldsymbol{\varepsilon})[\delta\boldsymbol{\varepsilon}] &= \mathbb{C}[\delta\boldsymbol{\varepsilon}] - \frac{4\mu^2\Delta r}{|\boldsymbol{\alpha}_n^{\text{tr}}(\boldsymbol{\varepsilon})|} \text{dev}(\delta\boldsymbol{\varepsilon}) \\ &+ \left(\frac{4\mu^2\Delta r}{|\boldsymbol{\alpha}_n^{\text{tr}}(\boldsymbol{\varepsilon})|} - \frac{4\mu^2}{2\mu + \phi'_d(r_n(\boldsymbol{\varepsilon}))} \right) \frac{\boldsymbol{\alpha}_n^{\text{tr}}(\boldsymbol{\varepsilon}) \cdot \delta\boldsymbol{\varepsilon}}{|\boldsymbol{\alpha}_n^{\text{tr}}(\boldsymbol{\varepsilon})|} \frac{\boldsymbol{\alpha}_n^{\text{tr}}(\boldsymbol{\varepsilon})}{|\boldsymbol{\alpha}_n^{\text{tr}}(\boldsymbol{\varepsilon})|}. \end{aligned}$$

After each iteration of the outer Newton method we update the memory variables

$$\begin{aligned} d^n(\boldsymbol{\varepsilon}) &= d^{n-1} + \Delta d^n, \\ \boldsymbol{\varepsilon}_p^n(\boldsymbol{\varepsilon}) &= \boldsymbol{\varepsilon}_p^{n-1} + \Delta\boldsymbol{\varepsilon}_p^n, \\ r^n(\boldsymbol{\varepsilon}) &= r^{n-1} + \lambda_p^n, \end{aligned}$$

and proceed with the next time step.

Algorithm 5 Update of the memory variables

- 1: **Input:** $d^n, \boldsymbol{\varepsilon}_p^n, r^n, \hat{\mathbf{u}}_h^{\text{wc},n,k}$
 - 2: compute λ_p^n
 - 3: $\Delta\boldsymbol{\varepsilon}_p^n = \lambda_p^n \frac{\boldsymbol{\alpha}_n^{\text{tr}}}{|\boldsymbol{\alpha}_n^{\text{tr}}|}$
 - 4: $\Delta r = \lambda_p^n$
 - 5: $Y^n = \mathcal{W}_e(\boldsymbol{\varepsilon}(\mathbf{u}^n) - \boldsymbol{\varepsilon}_p^n) + \mathcal{W}_p(\boldsymbol{\varepsilon}_p^n, r^n)$
 - 6: $\boldsymbol{\alpha}_n^{\text{tr}} = \mathbb{C}[\boldsymbol{\varepsilon}(\mathbf{u}^n)] - 2\mu\boldsymbol{\varepsilon}_p^n$
 - 7: $\Delta d^n = \max\{0, \phi_d(Y^n) - d^n\}$
 - 8: **Output:** $\Delta d^n, \Delta\boldsymbol{\varepsilon}_p^n, \Delta r^n$
-

Algorithm 6 Elasto-plastic damage model

1: **Input:** $\text{eps}_d, \text{eps}_r, T, \mathcal{K}_h, \mathbf{t}_N, \mathbf{f}, K_0, H_0, Y_0, H$
 2: $t = 0, n = 0, \hat{\mathbf{u}}_h^{\text{wc},0} = 0$
 3: **for** $K \in \mathcal{K}_h$ **do**
 4: assemble B_K
 5: **end for**
 6: **while** $t < T$ **do**
 7: $\hat{\mathbf{u}}_h^{\text{wc},n,0} = \hat{\mathbf{u}}_h^{\text{wc},n-1,0}$
 8: Compute $\hat{\mathbf{u}}_h^{\text{wc},n,0}$ from \mathbf{u}_D
 9: **for** $K \in \mathcal{K}_h$ **do**
 10: Compute ℓ_K^n
 11: **end for**
 12: $k = 0$
 13: **while** $\mathcal{D}^n > \text{eps}_d$ **do**
 14: **for** $K \in \mathcal{K}_h$ **do**
 15: $j = 0$ and compute $\ell_K^n(\mathbf{u}_K^{n,k,j}, \mathbf{z}^n)$
 16: **while** $|\ell_K^n(\mathbf{u}_K^{n,k,j}, \mathbf{z}^n)| > \text{eps}_r$ **do**
 17: assemble $A_K^{n,k,j}$
 18: compute $\Delta d_K^{n,k,j}, \Delta r_K^{n,k,j}, \Delta \boldsymbol{\varepsilon}_K^{n,k,j}$
 19: compute $\begin{pmatrix} \Delta \mathbf{u}_K^{n,k,j} \\ \Delta \boldsymbol{\lambda}_K^{n,k,j} \end{pmatrix} = \begin{pmatrix} A_K^{n,k,j} & B_K \\ B_K^\top & 0 \end{pmatrix}^{-1} \begin{pmatrix} \ell_K^n(\mathbf{u}_K^{n,k,j}, \mathbf{z}^n) \\ \hat{B}_K \hat{\mathbf{u}}_h^{n,k} \end{pmatrix}$
 20: update $\mathbf{u}_K^{n,k,j+1} = \mathbf{u}_K^{n,k,j} + \Delta \mathbf{u}_K^{n,k,j}$ and compute $\ell_K^n(\mathbf{u}_K^{n,k,j+1}, \mathbf{z}^n)$
 21: $j = j + 1$
 22: **end while**
 23: **end for**
 24: assemble $\hat{A}_h^{n,k,j} = \sum_K \begin{pmatrix} 0 \\ \hat{B}'_K \end{pmatrix}^\top \begin{pmatrix} A_K^{n,k} & B'_K \\ B_K & 0 \end{pmatrix}^{-1} \begin{pmatrix} 0 \\ \hat{B}_K \end{pmatrix}$,
 25: assemble $\hat{\ell}_h^{n,k} = \sum_K \begin{pmatrix} 0 \\ \hat{B}'_K \end{pmatrix}^\top \begin{pmatrix} A_K^{n,k} & B'_K \\ B_K & 0 \end{pmatrix}^{-1} \begin{pmatrix} \ell_K^n(\mathbf{u}_K^{n,k,j}, \mathbf{z}^n) \\ 0 \end{pmatrix}$.
 26: compute $\Delta \hat{\mathbf{u}}_h^{\text{wc},n,k}$ with $\hat{A}_h^{n,k} \Delta \hat{\mathbf{u}}_h^{\text{wc},n,k} = \hat{\ell}_h^{n,k}$
 27: $\hat{\mathbf{u}}_h^{\text{wc},n,k+1} = \hat{\mathbf{u}}_h^{\text{wc},n,k} + \Delta \hat{\mathbf{u}}_h^{\text{wc},n,k}$
 28: $\mathcal{D}^n = |\hat{\ell}_h^{n,k}|$
 29: $k = k + 1$
 30: **end while**
 31: Compute $\Delta d^{n,k,j}, \Delta \boldsymbol{\varepsilon}_p^{n,k,j}, \Delta r^{n,k,j}$, see Algorithm 5
 32: $d^{n+1} = d^n + \Delta d^{n,k,j}, \boldsymbol{\varepsilon}_p^{n+1} = \boldsymbol{\varepsilon}_p^n + \Delta \boldsymbol{\varepsilon}_p^{n,k,j}, r^{n+1} = r^n + \Delta r^{n,k,j}$
 33: $t = t + \Delta t_n$
 34: $n = n + 1$
 35: **end while**
 36: **Output:** $\hat{\mathbf{u}}_h^{\text{wc},n}, r^n, \boldsymbol{\varepsilon}_p^n, d^n$

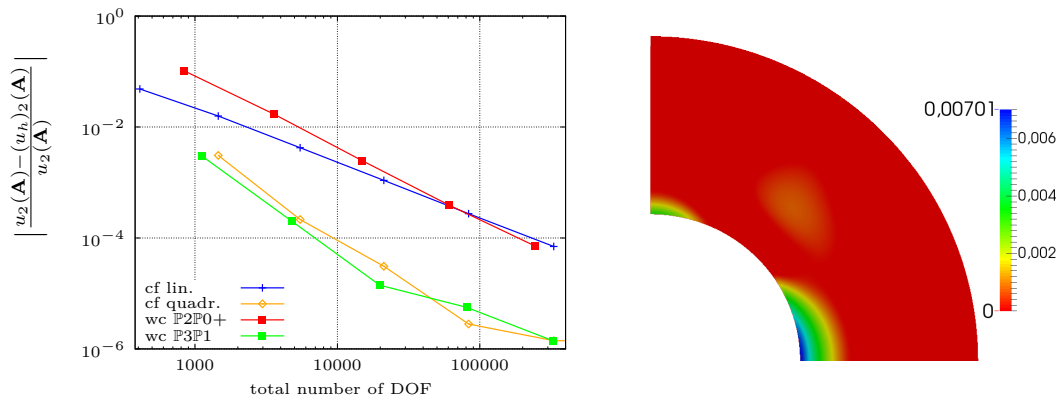


Figure 6.3: Plastic ring example: Vertical displacement of the point control point $\mathbf{A} = (0, 1.1)$ (left) and plastic flow of the homogeneous steel ring (right).

Plastic annulus under symmetric pressure

In this example we consider plasticity without damage. We compute it on the same ring domain as the bi-material example computed in Section 4.5. However this time we do not use a bi-material, but rather compute a homogeneous material, with the Lamé constants being $E = 200$ GPa and $\nu = 0.285$, which emulates a steel-like material. We use the initial yield stress $K_0 = 800$ MPa and the hardening modulus $H_0 = 0.3$. To avoid damage we set $Y_0 = \infty$. In this computation we use an implicit Euler-scheme for time-discretization.

The distribution of the plastic strain is shown in Fig. 6.3 (right). The relative displacement on the top of the ring, i.e. $u_2(\mathbf{A})$ with $\mathbf{A} = (0, 1.1)$ mm is shown in Fig. 6.3 (left). It can be seen, that the weakly conforming method and the conforming methods are comparable for this example. The lowest order weakly conforming method converges comparably to the linear conforming method, and the same relationship holds true for the $\mathbb{P}_3\mathbb{P}_1$ weakly conforming method and the quadratic conforming method.

This comparability of conforming and weakly conforming methods resembles the results of the smooth elastic example discussed in Section 4.1. This is again a somewhat smooth example with only a small peak of $|\boldsymbol{\sigma}(\boldsymbol{\varepsilon})|$ and no considerable singularity. In such a setting, where a basic method already yields sufficiently accurate results, no sophisticated method is needed. But we use these examples as a proof of concept, in this case of the plastic model, which we described

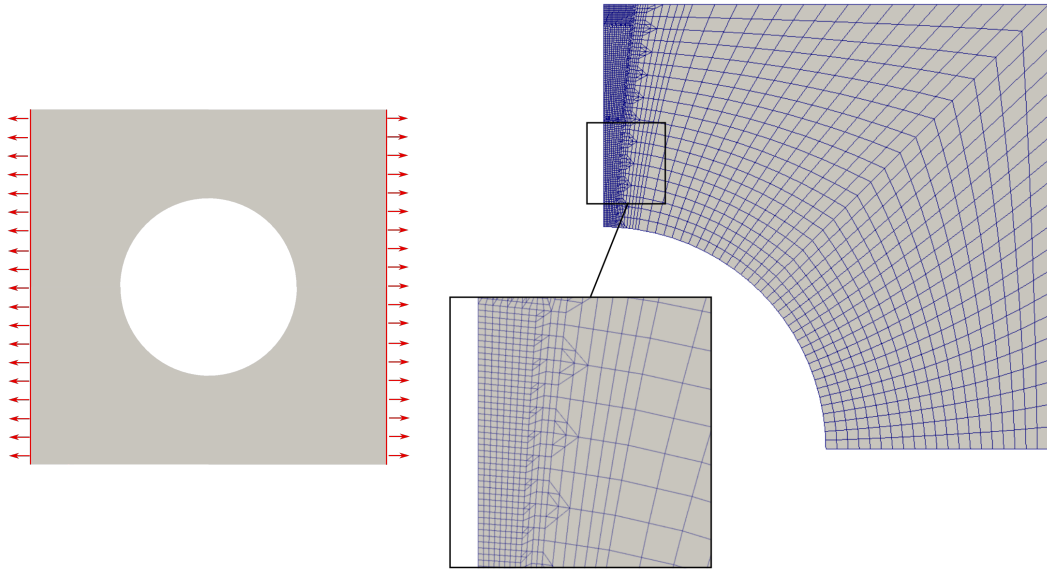


Figure 6.4: Square specimen example: Geometric configuration including boundary conditions (left), cell distribution of the computed part (right).

in this section. In the next example, the difficulty will be raised, leading to a whole different outcome.

Square specimen with circular hole

The following configuration is taken from [25] and computed with slightly altered boundary conditions. We compute a square specimen with the size $200 \times 200 \text{ mm}^2$ which has a circular hole with a diameter of 100 mm in the middle. Since the domain is symmetric, we compute only one quarter, cf. Fig. 6.4. For this reason, there is no need for an explicit Dirichlet boundary, instead we use symmetry boundary conditions with $u_1(\mathbf{x}) = 0$ for all \mathbf{x} with $x_1 = 0$ and $u_2(\mathbf{x}) = 0$ for all \mathbf{x} with $x_2 = 0$.

On the outer left boundary of the computed domain, the used mesh consists of small rectangles and on the rest of the domain it consists of larger rectangles. This a-priori mesh refinement ensures a better quality of the arising solution, because we expect that on this edge most of the plastic flow will occur. To avoid hanging nodes, a transition area between the two sides consists of rectangles and triangles.

This time the full model is used, plastic flow and damage. For this we set

cells	2788	11152	44608	178432
dim $V_{h,1}^{\text{cf}}$	2 151	8 196	31 977	126 303
$\ r\ _{0,\Omega}$	0.014021324	0.014544392	0.014695427	0.014735505
$\Delta\ r\ _{0,\Omega}$		5.23e-04	1.51e-04	4.00e-05
$\ d\ _{0,\Omega}$	0.016486170	0.015051032	0.014316882	0.0141116765
$\Delta\ d\ _{0,\Omega}$		1.44e-03	7.34e-04	2.05e-04
dim $V_{h,2}^{\text{cf}}$	6390	24 753	97 407	386 427
$\ r\ _{0,\Omega}$	0.014733576	0.014748607	0.01475053	0.014751109
$\Delta\ r\ _{0,\Omega}$		1.50e-05	1.92e-06	5.77e-07
$\ d\ _{0,\Omega}$	0.01402295	0.01403578	0.014035061	0.014034576
$\Delta\ d\ _{0,\Omega}$		1.28e-05	7.21e-07	4.84e-07
dim $M_{h,1}^{\text{wc}}$	3 980	16 039	64 394	258 052
$\ r\ _{0,\Omega}$	0.0147355127	0.014749554	0.01475090	0.014751146
$\Delta\ r\ _{0,\Omega}$		1.40e-05	1.35e-06	2.44e-07
$\ d\ _{0,\Omega}$	0.014024602	0.014034277	0.01403374	0.014034913
$\Delta\ d\ _{0,\Omega}$		9.68e-06	5.29e-07	1.16e-6
dim $M_{h,2}^{\text{wc}}$	5 260	21 292	85 672	343 696
$\ r\ _{0,\Omega}$	0.014751982	0.014750049	0.014750838	0.014751213
$\Delta\ r\ _{0,\Omega}$		1.93e-06	7.88e-07	3.75e-07
$\ d\ _{0,\Omega}$	0.014048736	0.014035174	0.014035070	0.014034631
$\Delta\ d\ _{0,\Omega}$		1.356e-05	1.05e-07	4.39e-07

Table 6.1: Square specimen example: Convergence study of the L_2 norm of the equivalent plastic strain and the L_2 norm of the damage variable d for two conforming methods and two weakly conforming configurations.

$E = 18000$ MPa, $\nu = 0.2$, $K_0 = 10$ MPa, $H_0 = 0.1$, $H = 0.1$ and $Y_0 = 0.1$. The specimen is pulled on both sides with a traction force of $\mathbf{t}_N = 12 \text{ N} \cdot \mathbf{n}$.

In Fig. 6.5 the results of our computation can be seen in the form of the distribution of the equivalent plastic strain r and of the damage variable d . It is clearly visible, that a spike in $|\boldsymbol{\sigma}(\boldsymbol{\varepsilon})|$ is emerging in Ω , right above the top side of the circular hole, which is subsequently causing a spike in r and d .

We computed this example with two conforming schemes and two configurations of our weakly conforming method. In Fig. 6.6 the numerical behavior of all schemes is depicted. As a reference measurement for the computed plastic flow we show the convergence of $\|r\|_{0,\Omega}$ and for the measurement of damage we compare $\|d\|_{0,\Omega}$. On low levels it can be seen, that both weakly conforming versions, as well as the quadratic conforming method are already significantly closer to the estimated values $r_{\text{ex}} \approx 0.014751964$ and $d_{\text{ex}} \approx 0.0140347$ as the linear conforming method, which shows signs of locking and only converges towards a suitable approximation on higher refinement levels. In the bottom

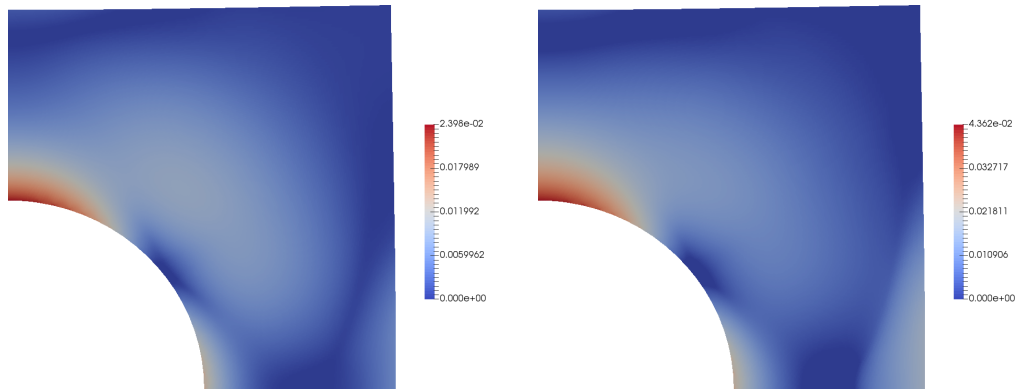


Figure 6.5: Square specimen example: Resulting distribution of the equivalent plastic strain ε_p (left) and of the damage variable d (right).

row we can see, that the estimated error $\|r - r_{\text{ex}}\|_{0,\Omega_h}$ converges monotone for all methods and all levels, with the exception of the lowest level of the $\mathbb{P}_3\mathbb{P}_1$ weakly conforming method, which shows a pre-asymptotic jump on the first refinement level. With respect to the estimated damage error $\|d - d_{\text{ex}}\|_{0,\Omega_h}$ both conforming method converge monotone, whereas the weakly conforming method, though convergent, has minor jumps between refinement level 2 and 3, which is probably caused by the influence of rounding errors and stopping criteria, since the overall error is already very small.

In Tab. 6.1 the inter-level jumps are given to further investigate the behavior of the various methods. It can be seen, that the methods converge more reliably, the farther away they are from the estimated values. This is expected, since the influence of small errors is of little influence, when the approximation error itself is large.

6.3 Contact Problems

Contact problems describe, in which way bodies interact when they collide or are pressed against each other. Possible sources to study this subject are [41, 60, 45]. For this work we compute a contact problem formulation with small deformation, where we compute only the impact on one body and assume that the other body is not impacted at all, which means that it consists of a far more rigid material than the contact body.

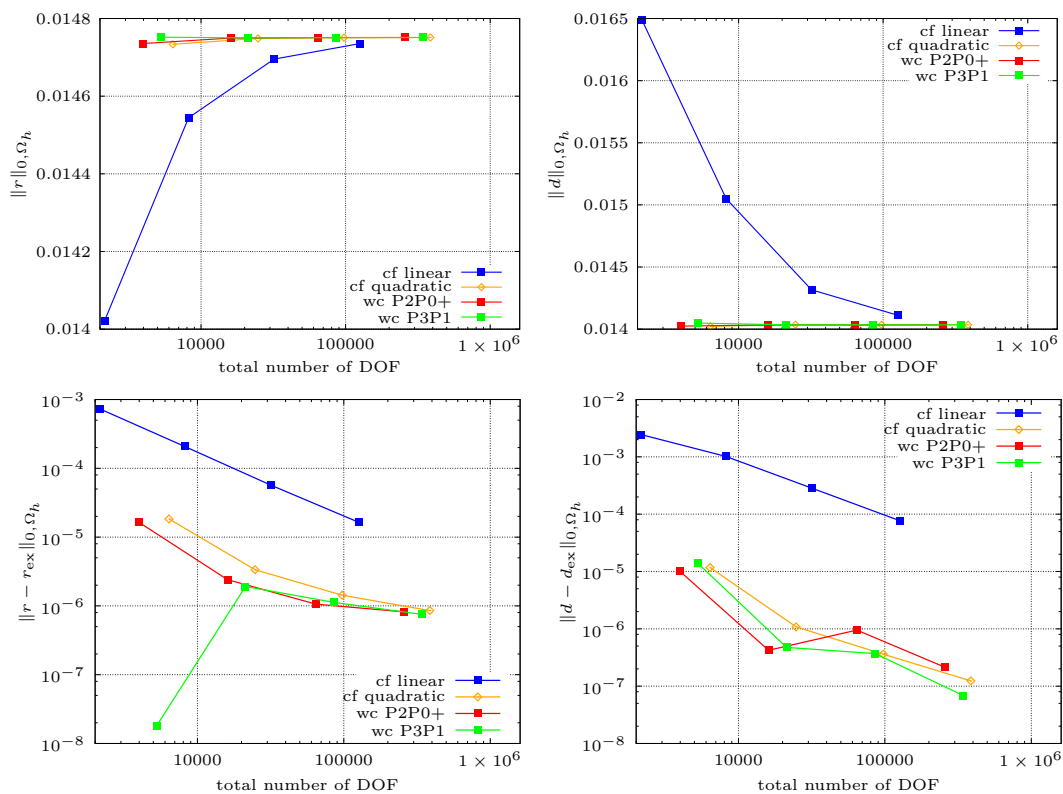


Figure 6.6: Square specimen example: A comparison of conforming methods with the weakly conforming methods. Top row: The L₂ norm of the equivalent plastic strain (left) and the L₂ norm of the damage variable d (right) are depicted. Bottom row: For both measures the errors are estimated, based on extrapolated values r_{ex} and d_{ex} .

In the examples before, we defined $\partial\Omega$ to consist of two parts, i.e. Dirichlet and Neumann boundary. For the contact formulation we introduce a third kind of boundary, the contact boundary $\partial\Omega_C$, as the surface of the domain, where contact could be possible. As a consequence, $\partial\Omega = \partial\Omega_D \cup \partial\Omega_N \cup \partial\Omega_C$. With this we now want to solve the system of equations

$$\operatorname{div} \boldsymbol{\sigma} = 0, \quad \text{in } \Omega, \quad (6.8)$$

$$\boldsymbol{\sigma} \mathbf{n} = 0, \quad \text{on } \partial\Omega_N, \quad (6.9)$$

$$\mathbf{u} = 0, \quad \text{on } \partial\Omega_D, \quad (6.10)$$

i.e. equations (2.4) of linear elasticity with $\mathbf{f} = \mathbf{t}_N = \mathbf{u}_D = \mathbf{0}$. Additionally we need to fulfill the complementary contact conditions

$$\mathbf{u} \cdot \mathbf{n} \leq g, \quad (\boldsymbol{\sigma}(\mathbf{u})\mathbf{n})\mathbf{n} \leq 0, \quad (\mathbf{u} \cdot \mathbf{n} - g)((\boldsymbol{\sigma}(\mathbf{u})\mathbf{n}) \cdot \mathbf{n}) = 0, \quad \text{on } \partial\Omega_C,$$

where $g : \partial\Omega_C \rightarrow \mathbb{R}$ is the distance functions, which measures the minimal distance between a point $\mathbf{x} \in \Omega$ and the rigid body.

In Algorithm 7 we describe how we embed the contact conditions in the weakly conforming framework. For this we use an active set strategy, where we start with an empty set $\mathcal{A} = \emptyset$ and add faces to this set, which are active in the sense that $\mathbf{u} \cdot \mathbf{n} > g$, i.e. the bodies are in contact on this face. For this we use a generalized Newton method, where we start each Newton-step by first computing on each cell $K \in \mathcal{K}$

$$\begin{pmatrix} \mathbf{u}_K \\ \boldsymbol{\mu}_K \end{pmatrix} = \begin{pmatrix} A_K & B'_K \\ B_K & 0 \end{pmatrix}^{-1} \begin{pmatrix} \ell_K \\ \hat{B}_K \hat{\mathbf{u}}_h \end{pmatrix}.$$

After this we check for each cell whether the contact conditions are fulfilled. If on a face $\mathbf{u} \cdot \mathbf{n} > g$, this cell is added to \mathcal{A} and we reassemble for the corresponding cell K B_K and the right hand side, to incorporate the contact condition, cf. Algorithm 8. After this, we assemble the global system

$$\begin{aligned} \hat{A}_h^k &= \sum_K \begin{pmatrix} 0 \\ \hat{B}'_K \end{pmatrix}^\top \begin{pmatrix} A_K^k & B'_K \\ B_K & 0 \end{pmatrix}^{-1} \begin{pmatrix} 0 \\ \hat{B}_K \end{pmatrix}, \\ \hat{\ell}_h^k &= \sum_K \begin{pmatrix} 0 \\ \hat{B}'_K \end{pmatrix}^\top \begin{pmatrix} A_K^k & B'_K \\ B_K & 0 \end{pmatrix}^{-1} \begin{pmatrix} \ell_K^k \\ 0 \end{pmatrix}, \end{aligned}$$

and compute $\Delta \hat{\mathbf{u}}_h^{\text{wc},k}$ with $\hat{A}_h^k \Delta \hat{\mathbf{u}}_h^{\text{wc},k} = \hat{\ell}_h^k$. With this we update $\hat{\mathbf{u}}_h^{\text{wc},k+1} = \hat{\mathbf{u}}_h^{\text{wc},k} + \Delta \hat{\mathbf{u}}_h^{\text{wc},k}$ and check, whether the residual $d = |\hat{A}_h^k \hat{\mathbf{u}}_h^{\text{wc},k+1} - \hat{\ell}_h^k|$ is small enough to stop the Newton method, otherwise we start the next iteration.

Algorithm 7 Solution of the contact problem

```

1: Input:  $\text{eps}_d$ 
2:  $k = 0$ 
3: while  $d > \text{eps}_d$  do
4:    $\mathcal{A} = \emptyset$ 
5:   for  $K \in \mathcal{K}_h$  do
6:      $g_K = 0$ 
7:      $n_{\text{test},K}$  = number of test functions in cell  $K$ 
8:     assemble  $A_K, B_K$  as for linear elasticity, see Algorithm 1
9:     compute  $\mathbf{u}_K$  with  $\begin{pmatrix} \mathbf{u}_K \\ \boldsymbol{\mu}_K \end{pmatrix} = \begin{pmatrix} A_K & B'_K \\ B_K & 0 \end{pmatrix}^{-1} \begin{pmatrix} \ell_K \\ \hat{B}_K \hat{\mathbf{u}}_h \end{pmatrix}$ 
10:     $n_{\text{faces}}$  = number of faces of cell  $K$ 
11:    for ( $f = 0$ ;  $f < n_{\text{faces}}$ ;  $f++$ ) do
12:      if  $F_f \subset \partial\Omega_C$  then
13:         $n_{\text{Lagr},f}$  = number of Lagrange parameter on face  $F_f$ 
14:        for ( $j = 0$ ;  $j < n_{\text{Lagr},f}$ ;  $j++$ ) do
15:           $g_K = g_K + \int_{F_f} (\mathbf{u}_K \mathbf{n} - g) \boldsymbol{\mu}_{F_j} da$ 
16:        end for
17:      end if
18:    end for
19:    if  $g_K > 0$  then
20:       $\mathcal{A} = \mathcal{A} \cup (\partial\Omega_C \cap \mathcal{F}_K)$ 
21:       $\mathbf{v}_{K,C} = \hat{B}_K \hat{\mathbf{u}}_h$ 
22:      update  $B_K, \mathbf{v}_{K,C}$ , see Algorithm 8
23:      compute  $\mathbf{u}_K$  with  $\begin{pmatrix} \mathbf{u}_K \\ \boldsymbol{\mu}_K \end{pmatrix} = \begin{pmatrix} A_K & B'_K \\ B_K & 0 \end{pmatrix}^{-1} \begin{pmatrix} \ell_K \\ \mathbf{v}_{K,C} \end{pmatrix}$ 
24:    end if
25:  end for
26:  assemble  $\hat{A}_h^k = \sum_K \begin{pmatrix} 0 \\ \hat{B}'_K \end{pmatrix}^\top \begin{pmatrix} A_K^k & B'_K \\ B_K & 0 \end{pmatrix}^{-1} \begin{pmatrix} 0 \\ \hat{B}_K \end{pmatrix}$ 
27:  assemble  $\hat{\ell}_h^k = \sum_K \begin{pmatrix} 0 \\ \hat{B}'_K \end{pmatrix}^\top \begin{pmatrix} A_K^k & B'_K \\ B_K & 0 \end{pmatrix}^{-1} \begin{pmatrix} \ell_K^k \\ 0 \end{pmatrix}$ 
28:  compute  $\Delta \hat{\mathbf{u}}_h^{\text{wc},k}$  with  $\hat{A}_h^k \Delta \hat{\mathbf{u}}_h^{\text{wc},k} = \hat{\ell}_h^k$ 
29:   $\hat{\mathbf{u}}_h^{\text{wc},k+1} = \hat{\mathbf{u}}_h^{\text{wc},k} + \Delta \hat{\mathbf{u}}_h^{\text{wc},k}$ 
30:   $d = |\hat{A}_h^k \hat{\mathbf{u}}_h^{\text{wc},k+1} - \hat{\ell}_h^k|$ 
31:   $k = k + 1$ 
32: end while
33: Output:  $\mathbf{u}_h^{\hat{\text{wc}}}, \mathcal{A}$ 

```

Algorithm 8 Update local matrices on contact boundaries

```

1: Input:  $\mathbf{v}_{K,C}$ ,  $B_K$ ,  $n_{\text{test},K}$ 
2:  $n_j = 0$ 
3: for ( $f = 0$ ;  $f < n_{\text{faces}}$ ;  $f++$ ) do
4:   if  $f$  on  $\partial\Omega_C$  then
5:     for ( $j = 0$ ;  $j < n_{\text{Lagr},f}$ ;  $j++$ ) do
6:       for ( $i = 0$ ;  $i < n_{\text{test},K}$ ;  $i++$ ) do
7:          $(B_K)_{in_j} = \int_{F_f} \mathbf{v}_i \boldsymbol{\mu}_{F,j} \, \text{d}\mathbf{a}$ 
8:       end for
9:        $(v_{K,C})_j = \int_{F_f} g \cdot \boldsymbol{\mu}_{F,j}$ 
10:       $n_j = n_j + 1$ 
11:    end for
12:  else
13:     $n_j = n_j + n_{\text{Lagr},f}$ 
14:  end if
15: end for
16: Output:  $\mathbf{v}_{K,C}$ ,  $B_K$ 

```

Parabolic shaped contact problem

The following example was formulated as a benchmark problem for our priority program by A. Popp, A. Seitz, W.A. Wall, C. Wieners, B.I. Wohlmuth and L. Wunderlich. Here, a parabolic shaped object is shifted downwards. This presses it against another object, which is fixed with Dirichlet boundary conditions along its bottom side, cf. Fig. 6.7. The bottom body is a unit square, which is transformed on its top side by the cosine curve

$$d(\xi) = 0.1(\cos(2\pi\xi) - 1),$$

with $\xi \in [0, 1]$. Since the top body is too rigid to be affected by any deformations, it is sufficient to define only its bottom side, which is described by the function

$$p(\xi) = 0.4\pi(\xi - \alpha - 0.5)^2 + \beta,$$

again with $\xi \in [0, 1]$. The parameter α describes a vertical shift of the upper body away from the center of the bottom body and is set to $\alpha = 0.005$ in this example. β describes how far the top body is pushed down and is set to

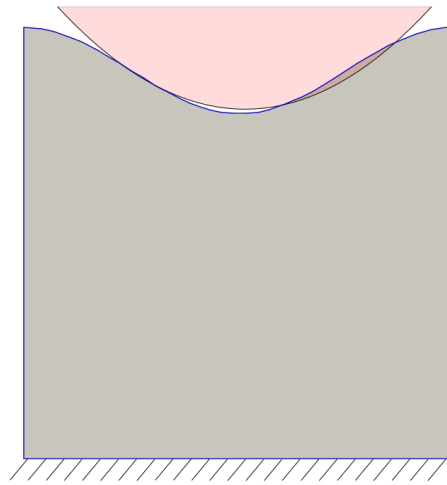


Figure 6.7: Contact benchmark: Domains of the two bodies which are in contact. The rigid body (red) overlaps contacts the lower body on both sides, since the bodies are put off center with $\alpha = 0.005$, the contact on the right is much more pronounced.

$\beta = 0.8135$, which ensures, that the bodies are in contact at two distinct areas, cf. Fig. 6.7.

In Fig.6.8 the resulting deformation and stress distribution $|\boldsymbol{\sigma}(\mathbf{u})|$ can be seen. In terms of deformation, it can be seen that almost all deformation happens on the right side and in terms of stress distribution it can be seen that, as expected, on the right side larger stress values are emerging. Both is due to the fact, that the bodies are slightly off-center to one another. In Tab. 6.2 the results of a computation with two variants of the weakly conforming method for various measurements can be seen. The contact boundary length is slightly decreasing with increasing refinement, which can be explained by the better resolution of the contact boundary on higher mesh levels. Not all cells with contact faces, which are active on a coarse level, have only child cells which have active faces as well. Both methods produce comparable results, which can be explained by the fact, that faces can only be active as whole or not at all. This causes a huge dependency of the quality of the solution on the resolution of the contact boundary. In non-contact examples we always created meshes,

dim $V_{h,2}^{\text{cf}}$	33 024	131 584	525 312	2 099 200
contact length	0.18395	0.18386	0.17932	0.17244
difference		-9.088e-5	-0.00454	-0.00688
$\ \mathbf{n} \cdot \boldsymbol{\sigma}(\mathbf{u})\mathbf{n}\ _{0,\Gamma_C}$	0.01127	0.01123	0.01123	0.01119
difference		-4.335e-5	3.419e-6	-4.523e-5
max. traction	0.03795	0.03766	0.03728	0.03716
difference		-2.918e-4	-3.831e-4	-1.139e-4
pos. max. traction	0.73413	0.74206	0.73822	0.74020
difference		0.00794	-0.00384	0.00198
dim $V_{h,3}^{\text{cf}}$	49 408	197 120	787 456	3 147 776
contact length	0.18395	0.18386	0.17932	0.17244
difference		-9.088e-5	-0.00454	-0.00688
$\ \mathbf{n} \cdot \boldsymbol{\sigma}(\mathbf{u})\mathbf{n}\ _{0,\Gamma_C}$	0.01172	0.01135	0.01127	0.01119
difference		0.00037	0.00008	0.00008
max. traction	0.03681	0.03671	0.03671	0.03683
difference		0.00010	1.71e-06	0.00012
pos. max. traction	0.74472	0.74068	0.74213	0.74020
difference		0.00404	0.00145	0.00193

Table 6.2: Contact benchmark: Reference values on 4 mesh levels with an estimation of the accuracy by the difference between two mesh levels. Here we use the $\mathbb{P}_3\mathbb{P}_1$ and the $\mathbb{P}_4\mathbb{P}_2$ weakly conforming method.

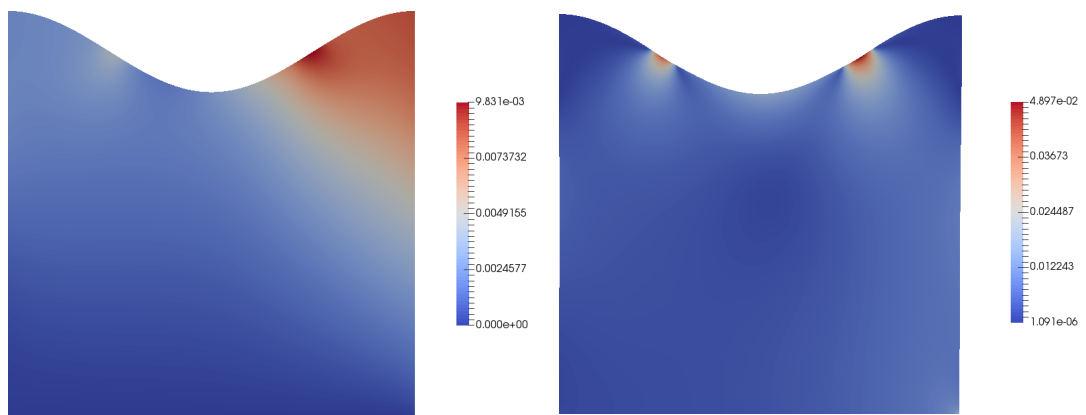


Figure 6.8: Contact benchmark: Displacement (left), and stress distribution $|\boldsymbol{\sigma}(\mathbf{u})|$ (right).

which refined the boundary conditions exactly, but this is not possible in this case, since there is no analytical solution to this problem and we don't know where the active parts of the contact boundary begin and where they end. We could solely give an estimate by analytically computing the intersections of the functions $d(\xi)$ and $p(x)$, but with increasing deformation these intersections move.

Overall this example works as a proof of concept, that the weakly conforming method can compute contact problems with an active set strategy.

Chapter 7

Conclusion

The goal of this work was to introduce and analyze the weakly conforming method for applications to solid mechanics. We formulated several requirements that define the capability of a numerical discretization scheme with respect to an application in the field of solid mechanics. These requirements were to produce a reliable solution in an efficient manner and the possibility to apply the scheme to a broad spectrum of existing material models. In this conclusion we want to discuss the fulfillment of these requirements.

Reliability of solutions

This point is especially important, since in general one does not want to compute a configuration of a mechanical part several times with different methods, but rather only once and still be certain, that the solution represents an accurate description of reality, within the limits of the chosen model. Over the course of this work we present numerous computed examples and in each of them, the weakly conforming method converges towards the same reference values as the benchmark methods do, no matter which reference value we choose. This leads us to conclude, that this method is reliable, in the sense that we can reproduce the solutions which established methods, like conforming finite elements methods and the discontinuous Galerkin method, produce for various examples.

Spectrum of possible models

Since there are a lot of different material models, which all aim to describe a certain physical material behavior as accurate as possible, a discretization scheme which can only reliably model a small number of these models seems futile. In this work we looked at small strain elasticity, with the complications of singularities (Section 4.2), locking (Section 4.3), geometrical anisotropy (Section 4.4), material jumps (Section 4.5) and incompressibility (Section 4.6). Furthermore we looked at non-linear materials, for example large deformations with a hyperelastic material (Section 6.1), plasticity and damage formulations (Section 6.2) and contact problems (Section 6.3). The weakly conforming method performs well for all linear examples, making it a suitable competitor in this field. Especially the fact that it is locking free and robust with respect to incompressibility are noteworthy properties. However, the non-linear material models leave us with mixed results, where we have no problem modeling contact problems, plasticity and damage, but the hyperelastic material has shown signs, that here still some more work is needed. With the weakly conforming method we could not compute *very* large deformations, since we always reached a point of divergence of the global solution.

Efficiency of the method

The established discontinuous Galerkin method lacks the ability to reduce the global amounts of freedom via static condensation, which the conforming methods can achieve, for example through the use of serendipity elements. On the other hand, conforming methods, though cheap, perform only well in certain situations, but when used for the solution of problems containing anisotropy, incompressibility, severe singularities or various other challenging phenomena, they may produce results which converge in a slow manner, if at all. Locking is a prominent problem of low order conforming methods. The weakly conforming methods combines some aspects of conforming and discontinuous Galerkin methods, as it has only a small global footprint and a sparse global system matrix, but performs well in most examples which we studied, even in numerically complicated situations. Additionally, it is not necessary to balance penalty parameters, which can be costly and can cause a

loss of efficiency.

However, there is a price to pay for the small global system, and this is an increased assembly time, since in every cell a few small matrices have to be assembled and a small linear system has to be solved. But this disadvantage can be tackled quite easy, since this additional assembly time can be parallelized with a near perfect speed-up, because all local systems requires only information from the cell they are based on and no communication is needed in this stage. Therefore, this is overcome easily, since today the number of possible parallel processes is large and growing fast, where every chip and every graphic chip, even for small home computers has multiple cores and possibly even multiple threads per core.

Lastly, the possibility for the application of various adaptive strategies was shown in Chapter 5, which is an important feature with respect to efficiency. This is especially important if large mechanical parts or whole buildings are simulated, since this usually means that there is a huge span of different stress values in different areas and a huge portion of the error comes often from small areas, where therefore the computational effort should be concentrated.

Outlook

The weakly conforming method was implemented for various scenarios and managed to solve a broad spectrum of problems. But for future works, there is still a few things left to do. As it became evident in Chapter 6, it is still unclear, whether larger deformations are possible, this has to be further investigated. Additionally, the transition to other fields, where finite element methods are deployed could be of interest and should be implemented and analyzed. Lastly, the adaptive algorithm could be improved, if a concept of handling hanging nodes would be developed, this would allow for a more loose marking and refinement of cells and provide more flexibility for large computations.

Bibliography

- [1] ABBAS, M. ; ERN, A. ; PIGNET, N.: Hybrid High-Order methods for finite deformations of hyperelastic materials. In: *Computational Mechanics* 62 (2018), Nr. 4, S. 909–928
- [2] ABBAS, M. ; ERN, A. ; PIGNET, N.: A Hybrid High-Order method for finite elastoplastic deformations within a logarithmic strain framework. In: *Numerical Methods in Engineering* 120 (2019), Nr. 3, S. 303–327
- [3] ABBAS, M. ; ERN, A. ; PIGNET, N.: A Hybrid High-Order method for incremental associative plasticity with small deformations. In: *Computer Methods in Applied Mechanics and Engineering* 346 (2019), S. 891–912
- [4] AINSWORTH, Mark: Robust a posteriori error estimation for nonconforming finite element approximation. In: *SIAM Journal on Numerical Analysis* 42 (2005), Nr. 6, S. 2320–2341
- [5] AINSWORTH, Mark ; ODEN, J T.: A posteriori error estimation in finite element analysis. In: *Computer methods in applied mechanics and engineering* 142 (1997), Nr. 1-2, S. 1–88
- [6] APEL, Thomas ; NICAISE, Serge: The finite element method with anisotropic mesh grading for elliptic problems in domains with corners and edges. In: *Mathematical Methods in the Applied Sciences* 21 (1998), Nr. 6, S. 519–549
- [7] APEL, Thomas ; SÄNDIG, Anna-Margarete ; WHITEMAN, John R.: Graded Mesh Refinement and Error Estimates for Finite Element Solutions of Elliptic Boundary Value Problems in Non-smooth Domains. In: *Mathematical Methods in the Applied Sciences* 19 (1996), S. 63–85

- [8] ARNOLD, Douglas N. ; BREZZI, Franco ; COCKBURN, Bernardo ; MARINI, L D.: Unified analysis of discontinuous Galerkin methods for elliptic problems. In: *SIAM J. Numer. Anal.* 39 (2002), Nr. 5, S. 1749–1779
- [9] BABUŠKA, Ivo ; SURI, Manil: On locking and robustness in the finite element method. In: *SIAM Journal on Numerical Analysis* 29 (1992), Nr. 5, S. 1261–1293
- [10] BABUŠKA, L ; SURI, Manil: The optimal convergence rate of the p-version of the finite element method. In: *SIAM Journal on Numerical Analysis* 24 (1987), Nr. 4, S. 750–776
- [11] BARRIOS, Tomás P ; GATICA, Gabriel N. ; GONZÁLEZ, María ; HEUER, Norbert: A residual based a posteriori error estimator for an augmented mixed finite element method in linear elasticity. In: *ESAIM: Mathematical Modelling and Numerical Analysis* 40 (2006), Nr. 5, S. 843–869
- [12] BARTELS, Sören: *Numerical approximation of partial differential equations*. Bd. 64. Springer, 2016
- [13] BAUMANN, Carlos E. ; ODEN, J T.: A discontinuous hp finite element method for convection-diffusion problems. In: *Computer Methods in Applied Mechanics and Engineering* 175 (1999), Nr. 3-4, S. 311–341
- [14] BAUMGARTEN, Niklas ; WIENERS, Christian: The parallel finite element system M++ with integrated multilevel preconditioning and multilevel Monte Carlo methods. In: *Computers & Mathematics with Applications* (2020)
- [15] BAYAT, Hamid ; KRÄMER, Julian ; WUNDERLICH, Linus ; REESE, Stefanie ; WOHLMUTH, Barbara ; WIENERS, Christian: Hybrid discretization in solid mechanics for non-linear and non-smooth problems (to appear).
- [16] BAYAT, Hamid R.: *Failure modeling of interfaces and sheet metals*. Aachen, Rheinisch-Westfälische Technische Hochschule Aachen, Dissertation, 2020. <http://dx.doi.org/10.18154/RWTH-2020-04847>. – DOI 10.18154/RWTH-2020-04847

- [17] BAYAT, Hamid R. ; KRÄMER, Julian ; WUNDERLICH, Linus ; WULFINGHOFF, Stephan ; REESE, Stefanie ; WOHLMUTH, Barbara ; WIENERS, Christian: Numerical evaluation of discontinuous and nonconforming finite element methods in nonlinear solid mechanics. In: *Computational Mechanics* 62 (2018), Nr. 6, S. 1413–1427. <http://dx.doi.org/10.1007/s00466-018-1571-z>. – DOI 10.1007/s00466-018-1571-z. – ISSN 1432-0924
- [18] BAYAT, Hamid R. ; WULFINGHOFF, Stephan ; KASTIAN, Steffen ; REESE, Stefanie: On the use of reduced integration in combination with discontinuous Galerkin discretization: application to volumetric and shear locking problems. In: *Advanced Modeling and Simulation in Engineering Sciences* 5 (2018), Nr. 1, S. 1–16
- [19] BECKER, Roland ; HANSBO, Peter ; LARSON, Mats G.: Energy norm a posteriori error estimation for discontinuous Galerkin methods. In: *Computer Methods in Applied Mechanics and Engineering* 192 (2003), Nr. 5, S. 723–733
- [20] BENZI, Michele ; GOLUB, Gene H. ; LIESEN, Jörg: Numerical solution of saddle point problems. In: *Acta numerica* 14 (2005), S. 1
- [21] BRAESS, Dietrich: *Finite elements: Theory, fast solvers, and applications in solid mechanics*. Cambridge University Press, 2007
- [22] BRAESS, Dietrich: An a posteriori error estimate and a comparison theorem for the nonconforming P1 element. In: *Calcolo* 46 (2009), Nr. 2, S. 149–155
- [23] BRENNER, Susanne C.: Korn’s inequalities for piecewise H1 vector fields. In: *Mathematics of Computation* (2004), S. 1067–1087
- [24] BRENNER, Susanne C. ; SCOTT, L. R.: *The Mathematical Theory of Finite Element Methods*. New York: Springer, 2008
- [25] BREPOLS, Tim: *Theory and numerics of gradient-extended damage coupled with plasticity*. Aachen, Rheinisch-Westfälische Technische Hochschule Aachen, Dissertation, 2018

- [26] BRIDGEMAN, L. J. ; WIHLER, T.P.: Stability and a posteriori error analysis of discontinuous Galerkin methods for linearized elasticity. In: *Computer Methods in Applied Mechanics and Engineering* 200 (2011), Nr. 13, S. 1543–1557
- [27] CARSTENSEN, C ; EIGEL, M ; GEDICKE, J: Computational competition of symmetric mixed FEM in linear elasticity. In: *Computer methods in applied mechanics and engineering* 200 (2011), Nr. 41-44, S. 2903–2915
- [28] CARSTENSEN, Carsten: A unifying theory of a posteriori finite element error control. In: *Numerische Mathematik* 100 (2005), Nr. 4, S. 617–637
- [29] CHOULY, F. ; ERN, A. ; PIGNET, N.: A Hybrid High-Order discretization combined with Nitsche’s method for contact and Tresca friction in small strain elasticity, 2019
- [30] CIARLET, Philippe G.: *Mathematical Elasticity: Volume I: three-dimensional elasticity*. North-Holland, 1988
- [31] CIARLET JR, Patrick ; DUNKL, Charles F. ; SAUTER, Stefan A.: A family of Crouzeix–Raviart finite elements in 3D. In: *Analysis and Applications* 16 (2018), Nr. 05, S. 649–691
- [32] COCKBURN, Bernardo ; KANSCHAT, Guido ; SCHÖTZAU, Dominik ; SCHWAB, Christoph: Local discontinuous Galerkin methods for the Stokes system. In: *SIAM Journal on Numerical Analysis* 40 (2002), Nr. 1, S. 319–343
- [33] COCKBURN, Bernardo ; KARNIADAKIS, George E. ; SHU, Chi-Wang: *Discontinuous Galerkin methods: theory, computation and applications*. Bd. 11. Springer Science & Business Media, 2012
- [34] DI PIETRO, Daniele A. ; NICAISE, Serge: A locking-free discontinuous Galerkin method for linear elasticity in locally nearly incompressible heterogeneous media. In: *Appl. Numer. Math.* 63 (2013), S. 105–116. – ISSN 0168–9274
- [35] DI PIETRO, Daniele A. ; ERN, Alexandre: *Mathematical Aspects of Discontinuous Galerkin Methods*. Springer, 2012

- [36] DÖRFLER, Willy: A convergent adaptive algorithm for Poisson's equation. In: *SIAM J. Numer. Anal.* 33 (1996), Nr. 3, S. 1106–1124. – ISSN 0036–1429
- [37] DÖRFLER, Willy ; NOCHETTO, Ricardo H.: Small data oscillation implies the saturation assumption. In: *Numerische Mathematik* 91 (2002), Nr. 1, S. 1–12
- [38] HANNUKAINEN, Antti ; STENBERG, Rolf ; VOHRALÍK, Martin: A unified framework for a posteriori error estimation for the Stokes problem. In: *Numerische Mathematik* 122 (2012), Nr. 4, S. 725–769
- [39] HANSBO, Peter ; LARSON, Mats G.: Discontinuous Galerkin methods for incompressible and nearly incompressible elasticity by Nitsche's method. In: *Computer methods in applied mechanics and engineering* 191 (2002), Nr. 17, S. 1895–1908
- [40] HORGER, Thomas ; REALI, Alessandro ; WOHLMUTH, Barbara ; WUNDERLICH, Linus: A hybrid isogeometric approach on multi-patches with applications to Kirchhoff plates and eigenvalue problems. In: *Computer Methods in Applied Mechanics and Engineering* 348 (2019), S. 396–408
- [41] JOHNSON, Kenneth L. ; JOHNSON, Kenneth L.: *Contact mechanics*. Cambridge university press, 1987
- [42] KNOBLOCH, P. ; TOBISKA, L.: On Korn's first inequality for quadrilateral nonconforming finite elements of first order approximation properties. In: *Int. J. Numer. Anal. Model.* 2 (2005), Nr. 4, S. 439–458
- [43] KRÄMER, Julian ; WIENERS, Christian ; WOHLMUTH, Barbara ; WUNDERLICH, Linus: A hybrid weakly nonconforming discretization for linear elasticity. In: *PAMM* 16 (2016), Nr. 1, S. 849–850
- [44] KRÄMER, Julian ; WIENERS, Christian ; WOHLMUTH, Barbara ; WUNDERLICH, Linus: A priori and a posteriori analysis for a hybrid discretization for linear elasticity / Institute for Applied and Numerical Mathematics, KIT. Version: 2020. <http://www.math.kit.edu/user/~wieners/KraemerWienersWohlmuthWunderlich2020.pdf>. 2020. – Forschungsbericht

- [45] LAURSEN, Tod A.: *Computational contact and impact mechanics: fundamentals of modeling interfacial phenomena in nonlinear finite element analysis*. Springer Science & Business Media, 2013
- [46] LIU, R. ; WHEELER, M.F. ; DAWSON, C.N.: A three-dimensional nodal-based implementation of a family of discontinuous Galerkin methods for elasticity problems. In: *Computers & Structures* 87 (2009), Nr. 3-4, S. 141 – 150
- [47] LONSING, Marco ; VERFÜRTH, Rüdiger: A posteriori error estimators for mixed finite element methods in linear elasticity. In: *Numerische Mathematik* 97 (2004), Nr. 4, S. 757–778
- [48] MARSDEN, Jerrold E. ; HUGHES, Thomas J.: *Mathematical foundations of elasticity*. Courier Corporation, 1994
- [49] MAURER, Daniel ; WIENERS, Christian: A parallel block LU decomposition method for distributed finite element matrices. In: *Parallel Computing* 37 (2011), Nr. 12, S. 742–758
- [50] PIGNET, Nicolas: *Hybrid High-Order methods for nonlinear solid mechanics*, Diss., 2019
- [51] RAMM, Ekkehard ; RANK, E ; RANNACHER, R ; SCHWEIZERHOF, K ; STEIN, E ; WENDLAND, W ; WITTUM, G ; WRIGGERS, Peter ; WUNDERLICH, Walter: *Error-controlled adaptive finite elements in solid mechanics*. John Wiley & Sons, 2003
- [52] REDDY, Junuthula N.: An introduction to the finite element method. In: *New York* 27 (1993)
- [53] REESE, Stefanie ; KÜSSNER, Martin ; REDDY, Batmanathan D.: A new stabilization technique for finite elements in non-linear elasticity. In: *International Journal for Numerical Methods in Engineering* 44 (1999), Nr. 11, S. 1617–1652
- [54] ROSENBERG, Ivo G. ; STENGER, Frank: A lower bound on the angles of triangles constructed by bisecting the longest side. In: *Mathematics of Computation* 29 (1975), Nr. 130, S. 390–395

- [55] SIMO, Juan C. ; HUGHES, Thomas J.: *Computational inelasticity*. Bd. 7. Springer Science & Business Media, 2006
- [56] SPAHN, Johannes: An efficient multiscale method for modeling progressive damage in composite materials. (2015)
- [57] ULRICH, Kai: *Comparison of conforming and non-conforming discretizations for Laplace's equation*, Bachelor thesis
- [58] WIENERS, Christian: A geometric data structure for parallel finite elements and the application to multigrid methods with block smoothing. In: *Computing and Visualization in Science* 13 (2010), Nr. 4, S. 161–175
- [59] WOHLMUTH, Barbara I.: A mortar finite element method using dual spaces for the Lagrange multiplier. In: *SIAM Journal on Numerical Analysis* 38 (2000), Nr. 3, S. 989–1012
- [60] WRIGGERS, Peter ; ZAVARISE, Giorgio: Computational contact mechanics. In: *Encyclopedia of computational mechanics* (2004)
- [61] WUNDERLICH, Linus M.: *Hybrid Finite Element Methods for Non-linear and Non-smooth Problems in Solid Mechanics*, Technische Universität München, Diss., 2017